

**DEVELOPMENT AND CHARACTERIZATION OF SPARK PLASMA SINTERED
BISMUTH FERRITE (BiFeO₃) MULTIFERROIC CERAMICS**

by

Md. Shofiqul Islam

MASTER OF SCIENCE IN MATERIALS AND METALLURGICAL ENGINEERING

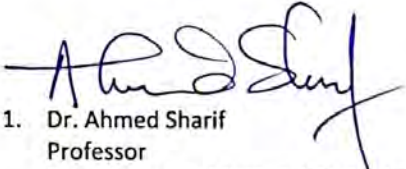


Department of Materials and Metallurgical Engineering
BANGLADESH UNIVERSITY OF ENGINEERING AND TECHNOLOGY

July 2019

The thesis titled "DEVELOPMENT AND CHARACTERIZATION OF SPARK PLASMA SINTERED BISMUTH FERRITE (BiFeO₃) MULTIFERROIC CERAMICS" submitted by Student- Md. Shofiqul Islam, Roll No.: 0416112017 Session: April 2016, has been accepted as satisfactory in partial fulfillment of the requirement for the degree of Master of Science in Materials and Metallurgical Engineering on July 3, 2019.

BOARD OF EXAMINERS


1. Dr. Ahmed Sharif
Professor
Department of MME, BUET, Dhaka
(Supervisor)


Chairman


2. Dr. Fahmida Gulshan
Head
Department of MME, BUET, Dhaka


Member
(Ex- officio)

M. HASAN
3. Dr. Mahbub Hasan
Professor
Department of MME, BUET, Dhaka

Member


4. Dr. Muktadir Billah
Assistant Professor
Department of MME, BUET, Dhaka

Member


5. Professor Dr. Md. Mohar Ali
Adjunct Professor
Department of Mechanical and Chemical
Engg. (MCE), Islamic University of
Technology (IUT), Board Bazar, Gazipur

Member
(External)

Declaration

I, Md. Shofiqul Islam, hereby declare that this thesis is entirely my own work and any part of it has not been submitted to anywhere else for the award of any degree. All quotations, figures and results from other sources are duly acknowledged and referenced.

শফিকুল ইসলাম

Md. Shofiqul Islam

Student no - 0416112017
DMME, BUET

Dedication

To the great man who is the pioneer of the link program between Department of Materials & Metallurgical engineering, BUET and Department of physics, UL

Dr. Tofail Syed

Table of Contents

Declaration.....	iii
Dedication.....	iv
Table of Contents.....	v
List of Figures:.....	x
List of Tables.....	xiii
Abbreviations.....	xiv
Nomenclature.....	xv
Acknowledgements.....	xvi
Abstract.....	xviii
Chapter 1: Introduction.....	1
1.1. Multiferroics and bismuth ferrite.....	1
1.2. Spark Plasma Sintering of BFO.....	3
1.3. Aim of the Thesis.....	3
1.4. Research Questions:.....	4
1.5. Research Hypothesis.....	5
1.6. Methodological Approach.....	5
1.7. Why BFO and Why SPS rather than Conventional Sintering.....	6
1.8. Scope of Thesis.....	8
Chapter 2: Literature Review.....	9
2.1. Primary ferroics.....	9
2.1.1. Ferroelectric Materials.....	12
2.1.2. Ferro-, Antiferro-, and Ferri-magnetic Materials.....	15
2.1.3. Ferroelastic Materials.....	16
2.2. Order parameter couplings.....	17
2.3. Multiferroics.....	18
2.3.1. Classification of Multiferroics.....	19
2.3.1.1. Type-I multiferroics.....	20
i. Ferroelectricity due to lone pairs.....	20

II.	Ferroelectricity due to charge ordering.....	21
III.	Multiferroic perovskites.....	21
IV.	“Geometric” ferroelectricity.....	22
2.3.1.2.	Type-II multiferroics: Magnetic multiferroics.....	23
a)	Spiral magnets.....	23
b)	Collinear magnets.....	23
2.3.2.	Why is it difficult to find materials that are both ferroelectric and magnetic?	24
2.3.2.1.	Requirements for magnetoelectric multiferroicity.....	24
i.	Symmetry.....	25
ii.	Electrical Properties.....	25
iii.	Chemistry.....	25
2.3.2.2.	Conclusion.....	27
2.4.	BiFeO ₃ multiferroics.....	28
2.4.1.	History of BiFeO ₃	28
2.4.2.	Science of BiFeO ₃	29
2.4.2.1.	Structure of BiFeO ₃	29
2.4.2.2.	Phase diagram of BiFeO ₃	30
2.4.3.	Electrical properties of BiFeO ₃	32
2.4.3.1.	Piezoelectric Properties of BiFeO ₃	33
•	Piezoelectric Materials.....	34
2.4.3.2.	Pyroelectric Properties of BiFeO ₃	34
2.4.3.3.	Dielectric constant of BiFeO ₃	35
2.4.4.	Magnetic properties of BiFeO ₃	36
2.4.5.	Optical Properties of BFO.....	37
2.4.5.1.	Linear optical properties.....	37
2.4.5.2.	Non-linear optical properties.....	38
2.4.5.3.	Infrared properties.....	38
2.4.6.	Applications of BiFeO ₃	41
2.4.6.1.	Ferroelectric and Piezoelectric Devices.....	41
2.4.6.2.	Spintronics.....	42
Chapter 3:	Experimental and Process Descriptions.....	45

3.1.	Introduction.....	45
3.2.	Processing of bismuth ferrite-based ceramics.....	45
3.2.1.	Ball Milling.....	46
3.2.2.	Drying.....	47
3.2.3.	Sintering.....	48
3.2.3.1.	Mechanism of sintering.....	49
3.2.3.2.	Sintering of Bismuth Ferrite.....	49
a.	Spark plasma sintering.....	49
b.	Process of the SPS Machine.....	51
c.	SPS parameter effects.....	52
d.	Thermal distribution during the SPS process.....	52
3.3.	Raw materials.....	53
3.4.	Sample Preparation.....	53
3.4.1.	Weight Measurement.....	54
3.4.2.	Milling.....	54
3.4.3.	Extraction and Drying.....	55
3.4.4.	Sieve Analysis.....	55
3.4.5.	Calcination.....	56
3.4.6.	Sintering of Bismuth Ferrite Ceramics.....	57
3.4.7.	Polishing.....	59
3.5.	Poling of Ceramics.....	60
3.5.1.	Poling Apparatus.....	60
3.5.2.	Poling procedure.....	62
3.6.	Characterization Methods.....	63
3.6.1.	Phase Study.....	63
3.6.1.1.	X- Ray Diffraction.....	63
1)	Phase identification.....	64
2)	Purity of Phase.....	65
3)	Crystallinity.....	65
4)	Texture.....	65
5)	Determination of Lattice Parameter.....	66

3.6.1.2. EDS.....	67
3.6.2. Microstructure Study	68
3.6.2.1. Optical Microscopy	68
• Thermal etching	69
3.6.2.2. Scanning Electron Microscopy.....	70
3.6.3. FTIR.....	70
3.6.4. Ferroelectric Property measurements	72
3.6.4.1. Piezoelectric measurements	72
• Piezoelectric Effect.....	73
3.6.4.2. Loop Test	74
3.6.5. Magnetic property measurement	74
3.6.6. Raman Spectroscopy.....	75
Chapter 4: Results and Discussions	77
4.1. Density Measurements	77
4.1.1. Effect of Sintering Parameters on Density.....	77
4.2. Microstructure Analysis	78
4.2.1. OM Micrograph Analysis.....	78
4.2.2. SEM Analysis	79
4.3. EDS Analysis.....	81
4.4. XRD Analysis	82
4.4.1. Origin of 2nd phases	85
4.5. Magnetic Property Measurement.....	87
4.6. Optical Properties Measurements	91
4.6.1. FT-IR Analysis	91
4.6.2. Raman Analysis	95
4.7. Electrical Properties Measurements	97
4.7.1. Piezoelectric Measurements	97
4.7.2. Ferro-electric Loop Test	101
Chapter 5: Conclusions and Future Work.....	105
5.1. Summary of the key Findings.....	105
5.2. Answers to the Research Questions	107

5.3. Testing of the Research Hypotheses.....	108
5.4. Future Work	109
References	110

List of Figures:

Figure 1-1: Schematic view of the $R3c$ structure built up from two cubic perovskite BiFeO_3 unit cells. The cations are displaced along the $[111]$ direction relative to the anions, and the oxygen octahedra rotate with alternating sense around the $[111]$ axis. In the ideal cubic perovskite structure, the oxygen ions would occupy the face-centered sites. 2

Figure 1-2: Flow chart outlining the methodological approach during this research project. 5

Figure 2-1: Hysteresis loops of (a) ferroelectric, (b) ferromagnetic and (c) ferroelastic materials. 11

Figure 2-2: Schematic representation of ferroelectric and ferromagnetic characteristics. Ferroelectrics and Ferromagnetics permit the orientations of electrical polarization and magnetization to be reversed by applying an electric field and magnetic field, respectively. 11

Figure 2-3: Characteristics of ferroic materials a) Ordering of physical properties, b) Hysteretic behavior and c) Existence of ferroic properties below a threshold temperature. 12

Figure 2-4: a) Perovskite crystal structure, showing a dipole moment generated by a displaced B-site atom; b) An example of Perovskite crystal structure (BaTiO_3). 14

Figure 2-5: Elementary cell of PbTiO_3 in the 'up' and 'down' spontaneous polarization states. 14

Figure 2-6: Common examples of magnetic dipole ordering. 15

Figure 2-7: Experimentally observed microstructures of lead phosphate. The two fully 'switched' crystals (a) and (c) display striped twin patterns whereas the crystal in the intermediate state (b) shows superposition of various twin orientations. 17

Figure 2-8: Ferroic orders and possible couplings between them. 18

Figure 2-9: Multiferroics materials are those that present more than one ferroic order. Multiferroics combining ferroelectric (left-orange) and ferromagnetic (right- blue) properties are very appealing materials because the possible presence of magnetoelectric coupling (magnetic control of polarization or electric control of magnetization, bottomgreen) can give rise to new technological functionalities. 19

Figure 2-10: Different microscopic mechanisms found in type-I multiferroics. 22

Figure 2-11: Schematic illustration of a structural transition process (a) ideal cubic structure $Pm\bar{3}m$ without tilting ($a0a0a0$); (b) $R\bar{3}c$ structure tilted along three axes with the same angle ($a-a-a$); (c) Displacement of Bi ion towards $[111]$ direction based on $R\bar{3}c$ 30

Figure 2-12: Phase Diagram of Fe_2O_3 and Bi_2O_3 31

Figure 2-13: Schematic of crystal structure of BFO and ferroelectric polarization (arrow) along $[111]$ direction. 32

Figure 2-14: a) Piezoelectric d_{33} constant, b) electromechanical coupling coefficients k_p , k_t , and c) elastic compliance S_{11E} of 760°C -sintered BiFeO_3 as a function of poling field. 33

Figure 2-15: Piezoelectricity—An intermingling of electric and elastic phenomena. 34

Figure 2-16: (Colour on-line) Schematic of tetragonal-like BiFeO_3 (BFO) with G-type antiferromagnetic ordering. 36

Figure 2-17: Schematics of the 64 nm antiferromagnetic circular cycloid. The canted antiferromagnetic spins (blue and green arrows) give rise to a net magnetic moment (purple arrows) that is specially averaged out to zero due to the cycloidal rotation. The spins are contained within the plane defined by the polarization vector 37

Figure 2-18: Color online Temperature dependence of the IR reflectivity spectra of BiFeO₃ ceramics. They note that the reflectivity value above 200 cm⁻¹ may be slightly reduced due to a small porosity of the ceramics and subsequent diffuse scattering of the IR beam. This can apparently enhance the phonon damping in the fit of our spectra, but the phonon frequencies are not substantially influenced. 39

Figure 2-19: (Color online) Schematic structural and magnetic phase diagram of Bi_{0.85}Nd_{0.15}FeO₃ (plotted according to data in Ref. 172). Ferroelectric R3c phase has Z=2, paraelectric Pbnm phase Z=4, and antiferroelectric Pbam phase Z=8. Electron diffraction revealed even Z=16 and Pbnm structure in AFE phase. Neél temperature of G-type antiferromagnetic phase increases with Nd concentration (dashed line). 40

Figure 2-20: (Color online) Temperature dependence of transverse phonon frequencies obtained from the fits of THz and IR spectra. Appearance of several new phonons due to lowering of crystal symmetry below 600 K is seen. 41

Figure 2-21: MERAM based on exchange-bias coupling between a multiferroic that is ferroelectric and antiferromagnetic (FE-AFM, green layer), and a thin ferromagnetic electrode (blue). A tunneling barrier layer between the two top ferromagnetic layers provides the two resistive states. Interestingly, BiFeO₃ could act not only as the magnetoelectric active layer, but also as the tunneling barrier. 44

Figure 3-1: Schematic representation of ball milling. 46

Figure 3-2: Schematic of a spark plasma sintering machine. 50

Figure 3-3: Milling pot with zirconia balls and ball mill setup. 54

Figure 3-4: Fume hood and Hot plate used for Drying and powders after drying. 55

Figure 3-5: Laboratory Test sieve with different mesh size. 56

Figure 3-6: Furnace used for calcination and powders after calcination. 57

Figure 3-7: Schematic of SPS Machine and Powder sample within graphite die at 750°C during spark plasma sintering. 58

Figure 3-8: Graph showing the effect of voltage and current on the temperature of the sample during spark plasma sintering. 58

Figure 3-9: Polishing Machine(PM-01023). 59

Figure 3-10: Operational set up during polarization of ceramics. 61

Figure 3-11: Image of the inside of the modified desiccator box containing the polarizing unit and a hot plate. 61

Figure 3-12: Polarizing unit used this research work. 62

Figure 3-13: Typical features of an XRD Machine. 64

Figure 3-14: Schematic showing principle of Optical Microscope. 69

Figure 3-15: Field Emission Scanning Electron (FESEM). 70

Figure 3-16: FTIR Analyzer. 71

Figure 3-17: Piezo Meter and one of readings of the prepared BFO sample SPS sintered at 825 °C.	72
Figure 3-18: Piezoelectric effect explained with a simple molecular model: (a) An unperturbed molecule with no piezoelectric polarization (though prior electric polarization may exist); (b) The molecule subjected to an external force (F_k), resulting in to polarization (P_k) as indicated; (c) The polarizing effect on the surface when piezoelectric material is subjected to an external force. .	73
Figure 3-19: Vibrating Sample Magnetometer (VSM).	74
Figure 3-20: Schematic diagram showing the working principle of Raman spectroscopy.....	75
Figure 4-1: Prepared BFO pellets SPS sintered at 625, 700, 750, 800, 825°C respectively.....	77
Figure 4-2: Microstructure of BFO-800 sample-a) Before etching, b) After etching	78
Figure 4-3: SEM micrographs of the pellets sintered by SPS and thermal etched for a) BFO-625, b) BFO-700, c) BFO-750, d) BFO-800, e) BFO-825. The magnification for all the images is 10,000.	80
Figure 4-4: EDS mapping of SPS prepared BFO sample showing O, Fe and Bi elements where a) BFO-625, b) BFO-700, c) BFO-750, d) BFO-800, e) BFO-625.	82
Figure 4-5: XRD patterns of BFO samples (BFO-calcined powder, BFO-625, BFO-700, BFO-750, BFO-800 and BFO-825).	83
Figure 4-6: XRD Patterns of BFO-750 sample showing respective peaks with a tiny amount of 2ndary phase.....	84
Figure 4-7: Compositional phase diagram of the Bi_2O_3 - Fe_2O_3 system proposed by Palai	85
Figure 4-8: Magnetization vs Applied Magnetic Field for SPS Sintered BFO-625.....	87
Figure 4-9: Magnetization vs Applied Magnetic Field for SPS Sintered BFO-700.....	88
Figure 4-10: Magnetization vs Applied Magnetic Field for SPS Sintered BFO-750.....	88
Figure 4-11: Magnetization vs Applied Magnetic Field for SPS Sintered BFO-800.....	89
Figure 4-12: Magnetization vs Applied Magnetic Field for SPS Sintered BFO-825.....	89
Figure 4-13: Magnetization vs Applied Magnetic Field for BFO-625, BFO-700, BFO-750, BFO-800, BFO-825.....	90
Figure 4-14: Fourier transform infrared (FT-IR) spectrum of Bismuth Ferrite a) BFO-Calcined powder, b) BFO-625, c) BFO-700, d) BFO-750, e) BFO-800, f) BFO-825.	92
Figure 4-15: Combined Fourier transform infrared (FT-IR) spectrum of Bismuth Ferrite (BFO-Calcined powder, BFO-625, BFO-700, BFO-750, BFO-800, BFO-825).	93
Figure 4-16: Raman Spectra of BFO-Calcined powder and SPS sintered samples (BFO-625, BFO-700, BFO-750).	95
Figure 4-17: Room Temperature Raman Spectra of BFO-750. Multi-peaks fitting shows Raman modes at different Raman shift.	96
Figure 4-18: P-E curve for BFO-625 and BFO-700 at voltage 5 kV and 10 kV.	102
Figure 4-19: P-E curve for BFO-750 at voltage 5 kV and 10 kV.	103
Figure 4-20: P-E curve for BFO-800 and BFO-825 at voltage 5 kV and 10 kV.	104

List of Tables

Table 3-1: Information of raw materials	53
Table 3-2: The space groups associated with the rhombohedral lattice are	67
Table 4-1: Density and %Theoretical Density of BFO-625, BFO-700, BFO-750, BFO-800 and BFO-825 samples.	77
Table 4-2: Comparative study on Grain Size of SPS prepared BFO sample	79
Table 4-3: Structure Parameter of the refined BFO samples.....	84
Table 4-4: M-H curve parameters.....	90
Table 4-5: Piezoelectric d_{33} constant (pC/N) of BFO-750 sintered sample	97
Table 4-6: Piezoelectric d_{33} constant (pC/N) of BFO-800(B)	98
Table 4-7: Piezoelectric d_{33} constant (pC/N) of BFO-800(A)	99
Table 4-8: Piezoelectric d_{33} constant (pC/N) of BFO-800(A) sample after poling.	100
Table 4-9: Piezoelectric d_{33} constant (pC/N) of BFO-825.....	100

Abbreviations

BFO	Bismuth Ferric Oxide (Bismuth ferrite or BiFeO ₃)
SPS	Spark Plasma Sintering
ME	Magnetoelectronic
FESEM	Field Emission Scanning Electron Microscopy
BNFO	Neodymium Bismuth Ferric Oxide
LBFTO	La and Ti co-doped BiFeO ₃
BLF	La doped BiFeO ₃
SHG	Second Harmonic Generation
NLO	Non-linear Optical
PZT	Lead Zirconate Titanate
MPB	Morphotropic Phase Boundary
BLFZ	La and Zr co-doped BiFeO ₃
BFO-Calcined Powder	BiFeO ₃ calcined powder calcined at 800°C
BFO-625	BiFeO ₃ pellet spark plasma sintered at 625°C
BFO-700	BiFeO ₃ pellet spark plasma sintered at 700°C
BFO-750	BiFeO ₃ pellet spark plasma sintered at 750°C
BFO-800	BiFeO ₃ pellet spark plasma sintered at 800°C
BFO-825	BiFeO ₃ pellet spark plasma sintered at 825°C
MERAM	Magnetoelectric Random Access Memory
IPA	Isopropyl Alcohol
VSM	Vibrating Sample Magnetometer

Nomenclature

T_N	Neel Temperature
T_C	Ferroelectric Curie Temperature
M	Magnetization
H	Magnetic Field
gm	Gram
mm	Millimeter
pC/N	Pico Coulomb per Newton
$^{\circ}\text{C}$	Degrees Celsius

Acknowledgements

At first, I would like to pay my gratitude to Almighty Allah for His upmost favor and enormous blessings to help me to complete my research in due time and without any difficulties.

I express my sincere gratitude to my supervisor, Prof. Dr. Ahmed Sharif for providing me with this research topic in the first place. Without his regular mentoring, direction and inspiration this research work would have been impossible. I thank him from the deepest of my heart for his sincere cooperation, precious advice and consistent encouragement & motivation. Had he not been there, the research could not have been completed. I would like to thank him for encouraging my research and for allowing me to grow as a research scientist.

I pay my utmost gratitude to Dr. Tofail Syed, Associate Professor, Department of Physics, University of Limerick for his constant and priceless help with all the technical, theoretical and experimental aspects of this research project. He was the first guidance I would seek whenever any problem had arisen, and in each occasion, he would prove to be wonderfully helpful.

I would like to thank Prof. Dr. Fahmida Gulshan for her continuous all kinds of guidance, support and help to excel in my research, and for allowing me to be the part of this link program. Her advice on both research as well as on my career have been invaluable.

I profoundly thank Dr. Christophe Silien, Associate Professor, Department of Physics, University of Limerick, for giving me permission to use various facilities available and for the support and advice he continues to give me, without which the research work would have become unduly exaggerated.

I would like to show my thankfulness to Aladin Mani, Senior Research Fellow, MOSAIC Group, University of Limerick, for his meticulous direction in every stage of my work.

I am also highly grateful to Dr. Ehtsham UL Haq, Postdoctoral Researcher, MOSAIC Group, University of Limerick for his kind co-operation and continuous support, guidance & encouragement to complete my research work.

I am equally grateful to Dr. Rabah Mouras, Senior Research Fellow, MOSAIC Group, University of Limerick, for his supervision and suggestions which has given me new insights. Without his co-operation with experimental aspects (especially FTIR & Raman), this project would have remained wholly incomplete.

I convey my regards to Garry Warren, Research Assistant, MOSAIC Group, University of Limerick for helping me with the experimental aspects of the project like spark plasma sintering operation, furnace operating and so on.

I would like to present my special thanks to Sarah Markham, PhD student, Department of Physics, University of Limerick for her benevolent assistance for any kind support at the Bernal Institute. If I didn't get any supports from her, it wouldn't be possible to stir my research work.

I would also like to Grace Brennan, PhD student, Department of Physics, University of Limerick for her instant support that help to continue my research without any interruption.

I would like to show my gratitude to all the faculty and staff members and lab technicians of MOSAIC Group, Department of Physics, University of Limerick whose services turned my research a success for their technical support throughout the endeavor, and to the staffs and members of DMME, BUET for providing me assistance whenever it was required.

I would especially like to thank Dr. Md. Abdul Matin, Head, Department of Glass and Ceramic Engineering (GCE) and Mehedi Hasan Rizvi, Assistant Professor, Department of Glass and Ceramic Engineering (GCE) as well as Mr. Arman Hussain, Assistant Professor, Department of Glass and Ceramic Engineering (GCE) for their restless co-operation and supportive ideas that help me do my research even at hardship.

Last but not the least, I would also like to pay my utmost gratitude to Md. Rafiqul Islam, Lecturer, MME for his relentless support and motivation throughout this research project.

My Parents, and family members, without whom I was nothing, they motivated me all times and extended their support morally and emotionally. I also thank my friends for supporting me for everything, and especially I can't thank them enough for encouraging me throughout this whole experience.

Abstract

BiFeO₃ (BFO) Ferrite ceramics were synthesized by an improved solid-state technique in conjunction with high-energy ball milling. Calcination was carried out at 800°C for 2 hours at a heating rate 5 °C/min and cooling rate was same as heating rate. High density BiFeO₃ ceramics were further sintered using by Spark Plasma Sintering (SPS) at different temperatures. Comparatively minimal amount of secondary phases was achieved than conventional sintering because of the higher heating rate with less holding time. They were contrived by different characterization techniques such as X-Ray Diffraction (XRD), Energy Dispersive X-Ray Spectroscopy (EDS), Optical Microscopy (OM), Scanning Electron Microscopy (SEM), Ferromagnetic, Ferroelectric and Piezoelectric Measurements, Raman Spectroscopy, Fourier-Transform Infrared Spectroscopy (FTIR) as well as shaped up Linear Optical Properties. The sintering conditions were optimized in order to attain high density, minimal amount of secondary phases and improved magnetic, piezoelectric and optical properties. The optimal structure and properties were achieved after Spark Plasma Sintering at 750°C for 5 minutes, under uniaxial pressure of 50 MPa. It was found that with decreasing grain size there occurs an enhancement in magnetization. This enriched magnetization is attributed to the improved grain boundaries. BFO-750 showed copious % transmittance about 27 with a long-range wavenumber. Piezoelectric measurements using a quasi-static method based on the Berlincourt method confirmed that conspicuous d_{33} coefficient measured maximum 7.2 ± 0.5 pC/N¹ without poling. Ferroelectric hysteresis loop measurement revealed that the samples have good ferroelectricity except BFO-800 and BFO-825 samples. Raman spectroscopy confirmed that there were maximum 13 modes formed in BFO-750. SPS + high density ball milling was supposed to be responsible for the outstanding obtained properties.

Keywords: Multiferroic, Perovskite, SPS, BFO, Piezoelectric, Optical properties.

Chapter 1: Introduction

A short brief discussion on bismuth ferrite as multiferroic, spark plasma sinter of bismuth ferrite, thesis aim, hypothesis and so on will be emphasized in this chapter. This chapter will be started with describing the outline of the thesis. The main concepts along with the aims, objectives, the research questions as well as importance of the thesis will be narrated. An account of the research hypothesis will be also given in this chapter with a breakdown of the methodological approach used in the investigation.

1.1. Multiferroics and bismuth ferrite

Multiferroics are multifunctional materials that exhibit more than one ferroic order in the same phase. In recent years, multiferroics have been drawing the attention of researchers due to their unique behaviour of coupling between two or more properties of ferroelectricity, ferromagnetism and ferroelasticity and also because of their potential technological applications in devices in spintronics, information storage, sensing and actuation [1-3]. However, ferroelectricity and ferromagnetism tend to be mutually exclusive and attaining both orders in a single compound is a rare phenomenon because the requirement of transition metal ions with partially filled d electrons for magnetism is not compatible with the requirement of empty d orbitals for ferroelectricity [4, 5]. Consequently, although there are many magnetic and ferroelectric materials, there are relatively few multiferroic materials. BiFeO₃ (BFO) is perhaps the only material that is both magnetic and a strong ferroelectric at room temperature. As a result, it has had an impact on the field of multiferroics that is comparable to that of yttrium barium copper oxide (YBCO) on superconductors, with hundreds of publications devoted to it in the past few years.

Bismuth ferrite is one of the most promising multiferroics and at room temperature, bulk BiFeO₃ presents a rhomboedrally distorted perovskite structure belonging to the space group R3c. The primitive unit cell contains two formula units (10 atoms) as shown in figure 1-1. Compared to other multiferroics, BFO exhibits a higher ferroelectric Curie temperature ($T_C \sim 830^\circ\text{C}$) and a high G-type antiferromagnetic ordering ($T_N \sim 370^\circ\text{C}$) temperature [6-7]. The Fe magnetic moments are coupled ferromagnetically within the pseudocubic (111) planes and antiferromagnetically between the near planes; this is called the G-type antiferromagnetic order. If the magnetic moments are oriented perpendicular to the [111] direction, the symmetry also permits a canting of the antiferromagnetic sublattices resulting in a macroscopic magnetization called weak magnetism. The R3c symmetry permits the development of a spontaneous polarization along

[111], and Bi, Fe, and O are displaced relative to one another along this 3-fold axis. The largest relative displacements are those of Bi relative to O, consistent with a stereochemically active Bi lone pair. The polar displacements (relative to cubic perovskite) are noticeably extreme when compared with those in non-lone-pair-active perovskite ferroelectrics such as BaTiO₃ or KNbO₃ but are consistent with those observed in other Bi-based perovskites.

Thus, BFO is one of the most popular objects in modern material science and an excellent candidate for use in ferroelectric non-volatile memories and high-performance electronics.

But unfortunately, BFO has some inherent problems. In BFO, magnetic ordering is of antiferromagnetic type, having a spatially modulated spin structure with an incommensurate long-wavelength period of 62 nm which cancels the macroscopic magnetization and also inhibits the observation of the linear magnetoelectric effect [8–11]. In addition, the bulk BFO is characterized by serious current leakage problems due to the existence of a large number of charge centres caused by oxygen ion vacancies and Bi₂O₃ evaporation during sintering process which makes it difficult to achieve high resistivity.

These problems limit the use of BFO for fabrication of multifunctional devices. The mechanism inducing resistivity in BFO films can be attributed to the variable oxidation states of Fe ions (Fe³⁺ to Fe²⁺), which requires oxygen vacancies (V_O²⁺) for charge compensation and produces electron hopping in films. Another mechanism is due to high volatility of atom Bi which generates V_{Bi}³⁻ vacancies in lattice accompanied by the emergence of the second-phase (such as Bi₂Fe₄O₉ and Bi₂₅FeO₄₀ or Bi₂₅FeO₃₉). The V_O²⁺ and V_{Bi}³⁻ vacancies are highly mobile and inclined to reduce resistivity on the application of electric field.

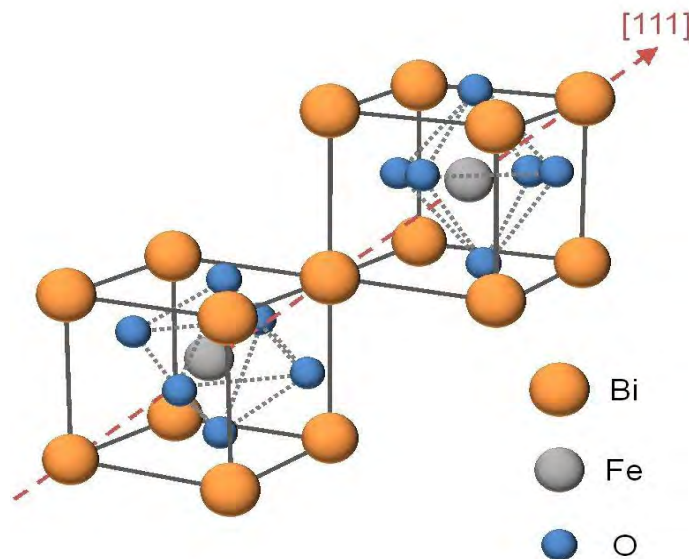


Figure 1-1: Schematic view of the R3c structure built up from two cubic perovskite BiFeO₃ unit cells. The cations are displaced along the [111] direction relative to the anions, and the oxygen octahedra rotate with alternating sense around the [111] axis. In the ideal cubic perovskite structure, the oxygen ions would occupy the face-centered sites. Adapted from [10]

Therefore, of late, there has been considerable interest in the design of magnetoelectric materials and finding ways to improve the magnetic and ferroelectric properties of BFO.

1.2. Spark Plasma Sintering of BFO

Although various syntheses methods have been used to prepare BiFeO₃ powders, starting from solid state reaction to wet chemical methods (sol-gel, co-precipitation, hydrothermal, microwave-hydrothermal, sonochemical and auto-combustion methods) [30], formation of the secondary phases cannot be avoided in any of those methods, while their amount can be significantly lowered by careful optimization of the processing conditions. Several research teams have reported successful preparation of phase pure bismuth ferrite powders, using methods such as molten alkali metal salts [31] and mechanochemical synthesis [8–10]. Another important problem in fabrication of BFO ceramics is difficult densification of the powders during sintering. According to literature data, it is extremely difficult to reach densities exceeding 90 %TD (theoretical density) [29]. Some alternative sintering techniques, such as rapid liquid phase sintering [30–35] or microwave sintering of BFO [36], have been applied to improve both purity and density of the final product.

Among different sintering methods, spark plasma sintering (SPS) has been recognized as a potentially efficient method of preparation of high density and single phase BFO ceramics with improved dielectric, ferroelectric and magnetic properties [37]. For example, SPS of powders, previously treated in a high-energy ball mill, resulted in high-density BFO samples (density up to 97 %TD) [38,39]. Although several studies reported on SPS of BFO ceramics, the full potential of employing this sintering method in processing a fully dense, phase pure BiFeO₃ ceramics is not still sufficiently explored. For example, very limited data on magnetic properties of BFO ceramics, processed by SPS, were presented in some of those studies, indicating enhanced magnetization [40] of the SPS samples in comparison with the samples processed using more conventional sintering methods.

1.3. Aim of the Thesis

The aims of this thesis will be engrossed in the synthesis and sintering of bismuth ferrite. This involves following proven synthesis technique and adapting it, so to be compatible with the laboratory equipment available during this project. Throughout the synthesis process a detailed analysis will be carried out as to determine the optimum parameters required to effectively and efficiently produce bismuth ferrite powder. Following the synthesis, the bismuth ferrite powder will then be sintered into a highly dense and homogenous ceramic. The sintering of the ceramic

will be carried out in a novel sintering technique named spark plasma sintering. Sintering parameters will be varied throughout this process and characterization will be carried out at each step. The focus of this sintering will be on producing a bismuth ferrite which is homogenous in composition with optimal physical, chemical and electrical properties. The electrical and crystallographic properties of the ceramic will be investigated by measuring its piezoelectric response following high voltage electrical polarization. Each aim will be done to the highest scientific standards and a detail review of each step will be documented throughout the following report.

The objectives of this research work are:

- a) Synthesis of bismuth ferrite;
- b) Spark plasma sintering and characterization of bismuth ferrite;
- c) Find out the optimum SPS sintering condition with varying sintering temperature;
- d) Find out magnetic properties, electrical properties, optical properties and optical response of bismuth ferrite.

The main target of this thesis will be to determine the optimum sintering condition of pure BFO samples as well as to focus on some linear optical properties. Moreover, ferroelectric and ferromagnetic properties as well as piezoelectric property of SPS sintered BFO will be emphasized on the present work.

As the preparation of the compacts is simple, the biggest challenge is to achieve very fine grain structure with minimum porosity. On this occasion the toughest task is to find the optimum sintering temperature which will bring the desired microstructure. Control of the geometry of samples is another challenge to take over.

One important thing here is the use of powder which has a size in nanometer range. Such powders possess very high surface energy and consequentially, are more reactive than coarser powders. Hence the sintering temperature needs to be modified accordingly.

1.4. Research Questions:

Bismuth ferrite (BiFeO_3) has generated increasing interest from the community of science and technology as it possesses spontaneous magnetic and polar orders well above room temperature. BFO has potential applications in functional materials and fundamental physics, such as high dense non-volatile memory devices, spintronics, telecommunication and sensors. There will be scrutinized to the optical and structural properties of bismuth ferrite to further understand its function within infrared filter and also to develop its potential for future applications.

The following questions will be investigated on this work:

- 1) How do spark plasma sintering parameters effect the properties of the bismuth ferrite ceramic?
- 2) What are the optical properties of bismuth ferrite ceramic? Should bismuth ferrite exhibit infrared response?
- 3) Should bismuth ferrite exhibit piezoelectric effect?
- 4) Should bismuth ferrite demonstrate ferro magneticity, ferroelectricity and pyroelectricity?

1.5. Research Hypothesis

These research questions were investigated on the basis of the following research hypotheses:

Hypothesis 1: Structural changes should have impact on infrared response, piezoelectric and magnetic response.

Hypothesis 2: Sintering temperature is directly related to the % transmittance with a range of wavenumber.

1.6. Methodological Approach

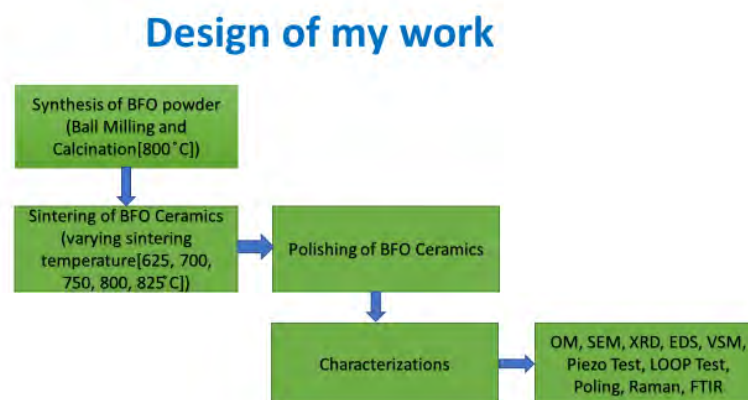


Figure 1-2: Flow chart outlining the methodological approach during this research project.

Now outline the experimental procedures used during this research project will be drawn below in a flow chat which gives an outline of each step taken.

There will be outlined the process descriptions and experimental details used during the synthesis and characterization of bismuth ferrite ceramics on the chapter three. A detailed account of all the synthesis and characterization techniques used will be given.

1.7. Why BFO and Why SPS rather than Conventional Sintering

In this competitive world people finds motivation or gets information from other works with healthy competitive way. In this present works it will be highlighted why BiFeO₃ has been chosen as multiferroic materials and SPS has been preferred rather than conventional sintering with respect some praiseworthy previous works

The current interest in bismuth ferrite was stimulated primarily by a 2003 paper from Ramesh's group [12] which showed that it had unexpectedly large remnant polarization, P_r , 15 times larger than previously seen in bulk, together with very large ferromagnetism of ca. 1.0 Bohr magneton (μ_B) per unit cell. Single crystals grown more recently in France in 2006–7 have confirmed the large value of the polarization first observed in the films, showing also that it is intrinsic; [13-17] In 2005 Xiaoding et al. [18] investigated the transport properties of aliovalent-ion-doped BiFeO₃ thin films in order to identify the cause of high leakage currents. Doping of 2 at. % Ti⁴⁺ ions increased the dc resistivity by more than three orders of magnitude. In 2006 Wang et.al. [19] reported the effect of Ba doping on magnetic, ferroelectric, and magnetoelectric properties on BiFeO₃ at room temperature Ba doped BiFeO₃ compounds were prepared by a solid-state reaction that was ensured an increase of the dielectric constant with the increase of the applied magnetic field.

In 2007 Yuan-Hua et al. [20] studied the enhancement of ferromagnetic properties in BiFeO₃ polycrystalline ceramic by La doping with the structure transformation and magnetic properties of Bi_{1-x}La_xFeO₃ (x=0.0–0.15) ceramics prepared by a conventional solid-state reaction processing.

In 2010 Cui et al. [21] reported the dielectric, magnetic, and magneto-electric properties of La and Ti codoped BiFeO₃ (LBFTO). Co-doping changes the structure of BiFeO₃ from rhombohedral to tetragonal and the ferromagnetic properties and electric polarization of LBFTO are remarkably improved. In 2010, Changyong et al. [22] reported the magnetic properties of La and (La, Zr) doped BiFeO₃ ceramics Bi_{0.9}La_{0.1}FeO₃ (BLF) and Bi_{0.9}La_{0.1}Fe_{0.98}Zr_{0.02}O₃ (BLFZ) ceramics were synthesized by conventional soli-state reaction method with average grain size of BLFZ (~700 μm) was greatly reduced in comparison with BLF (~6 μm).

In 2012 Reetu et al. [23] reported the structural transformation and improved dielectric and magnetic properties in $\text{Bi}_{0.8}\text{La}_{0.2}\text{Fe}_{1-x}\text{Ti}_x\text{O}_3$ ($x = 0.0, 0.05, 0.10, 0.15$) Powder x-ray diffraction investigations performed at room temperature show that the crystal structure was rhombohedral for $x = 0.0, 0.05$; tetragonal for $x = 0.15$; and a phase boundary occurred at $x = 0.1$. In 2013, Anup et al. [24] reported the role of co-doping (20% La in Bi-site and 10% Mn in Fe-site) on multiferroic properties in insulating BiFeO_3 ceramic. The X-ray diffraction (XRD) with Rietveld refinement shows that the structure of $\text{Bi}_{0.8}\text{La}_{0.2}\text{FeO}_3$ is orthorhombic (Pnma) when substitution of 10% Mn- ions in Fe-site, no structural change occurs which has been supported by micro-Raman study.

In 2013 Jin et al. [25] reported the effect of Mn doping on crystal structure, electric, magnetic and optical properties of BiFeO_3 thin films prepared via the sol-gel process on indium tin oxide/glass substrates X-ray diffraction analysis indicated that Mn-doped BiFeO_3 thin films presented single tetragonal structure with P4mm symmetry. From the work of previous researchers, it is evident that A-site and B-site co-doping is a good way to improve the multiferroic properties of BFO, both in films and ceramics [26–28].

According to the previous findings it is crystal clear that BFO has a higher Curie temperature, antiferromagnetic Neel temperature and polarization than other multiferroic materials.

In 2013 Song et al. [37] reported the 750°C-SPS prepared BFO ceramic samples possessed a single perovskite structure and they were compared with the conventionally synthesized ones. Previous studies from Prejon et al. [38] they have shown here that high-quality, phase-pure BiFeO_3 ceramics, whose electrical properties are comparable with those of a good-quality BiFeO_3 single crystal but with even lower conductivity, can be prepared by direct mechanochemical synthesis from pristine iron and bismuth oxides.

Recent studies in 2015 from Prejon et al. [39] mentioned grain sizes of the BFO pellets obtained by SPS are in the range from 50-100 nm, which demonstrates that it is possible to obtain nanostructured ceramics of La-substituted BiFeO_3 using mechanosynthesis followed by SPS at low temperature (625–650 °C). In 2012 Wang et al. [40] it was found that with decreasing grain size there occurs an enhancement in magnetization and a simultaneous suppression in current leakage which ascribed to fewer conduction paths provided by the compacted grain structure. In 2013 Dai et al. [153] reported the dielectric permittivity and loss of SPS samples(BFO) were measured as functions of sintering temperature, frequency, and annealing conditions. In 2016 Brankovic et al. [185] reported the optimal structure and properties were achieved after spark plasma sintering at 630°C for 20 min, under uniaxial pressure of 90 MPa. In 2016 Wang et al. [194] revealed the 4hr oxygen-annealed BFO sample contained a single rhombohedral perovskite phase while the samples annealed in the other conditions contained small quantities of impurity phases besides the rhombohedral perovskite phase.

The above findings ensured that minimal amount of secondary phases would be obtained because of the higher heating rate with less holding time compared to conventional sintering technique.

1.8. Scope of Thesis

This thesis is broken up into five distinctive chapters, which include; Chapter 1- Introduction, Chapter 2- Literature Review, Chapter 3- Experimental and Process Details, Chapter 4- Results and Discussion, and Chapter 5- Conclusions and Future Work.

Chapter 1 will be started with describing the outline of the thesis. The main concepts along with the aims, objectives, the research questions as well as importance of the thesis will be narrated. This chapter will be started with describing the outline of the thesis. The main concepts along with the aims, objectives, the research questions as well as importance of the thesis will be narrated. An account of the research hypothesis will be also given in this chapter with a breakdown of the methodological approach used in the investigation.

Chapter 2, here an elaborated literature review will be deployed. A collection of all literature relevant to this investigation will be compiled into a concise and informative section. This chapter will be represented as detail views on primary ferroic; multiferroics and its classification; multiferroic bismuth ferrite; history, science, structure, properties and applications of bismuth ferrite.

Chapter 3 will be outlined the process descriptions and experimental details used during the synthesis and characterization of bismuth ferrite ceramics. A detailed account of all the synthesis and characterization techniques used will be given.

In Chapter 4, an elaborate results and discussion will be outlined with details explanation for each finding as well as the relevant experimental results and thoroughly explain the relevance of each result.

In **Chapter 5** a conclusion will be drawn from the experimental results which are novel to this field of study. Some recommendations will be also enlisted on some future work proposals section.

Chapter 2: Literature Review

In chapter 2 an elaborated literature review will be deployed. A collection of all literature relevant to this investigation will be compiled into a concise and informative section. This chapter will be represented as detail views on primary ferroic; multiferroics and its classification; multiferroic bismuth ferrite; history, science, structure, properties and applications of bismuth ferrite.

2.1. Primary ferroics

A primary ferroic material exhibits a spontaneous magnetization, a spontaneous polarization or a spontaneous strain. And these spontaneous orders can be reoriented by an external magnetic field, electric field, or mechanical stress below a characteristic temperature (Curie temperature).

There are four primary ferroic order parameters. They are described below.

- ❖ **Ferroelectricity:** It is the property due to which materials show spontaneous, stable polarization that can be switched hysteretically by an applied electric field; antiferroelectric materials have ordered dipole moments which cancel each other completely within each crystallographic unit cell resulting net polarization zero [41].
E.g. BaTiO_3 .
- ❖ **Ferromagnetism:** It is the property due to which materials exhibit spontaneous, stable magnetization that can be switched hysteretically by an applied magnetic field; antiferromagnetic materials possess ordered magnetic moments which nullify each other completely within each magnetic unit cell resulting net magnetization zero [41].
E.g. Fe_3O_4 .
- ❖ **Ferroelasticity:** Materials display a spontaneous, stable deformation which if we apply a stress can be switched hysteretically [41]. E.g. $\text{Au}_x\text{Cu}_{1-x}\text{Zn}$.
- ❖ **Ferrotoroidicity:** Materials possess a stable and spontaneous order parameter that is taken to be the curl of a magnetization or polarization. By analogy with the above examples, it is anticipated that this order parameter may be switchable. Ferrotoroidic materials have evaded unambiguous observation.

Ferro- is a prefix which means iron in Latin, it is primitively used to describe materials exhibiting strong magnetic properties as iron does. Apart from iron, other elements like cobalt, nickel and rare earth elements also exhibit magnetic behavior called ferromagnetism, which enables materials made from the above-mentioned elements to form permanent magnets. Ferromagnetic materials were reported to have a long-range ordering phenomenon at the atomic level. Many small domains can be found in a magnetic material with plenty of unpaired electrons inside. Microscopically, those unpaired electrons are not randomly alligned, they interact with others to make the alignment in the same direction within the same domain. However, these domains are randomly aligned so that on the whole, they cancel out to make zero magnetism. When an external magnetic field is applied, those domains with the magnetic field grow at the expense of their neighbouring domains, causing materials to be magnetized. This phenomenon is characterized by a hysteresis loop of magnetization M as a function of external magnetic field H , as illustrated in figure 2-1 (b). It is obvious that the magnetization is saturated at high magnetic field and a remnant magnetization can still exist in the absence of the field. In addition, the direction of magnetization could be reversed provided that the external magnetic field is switched oppositely with quite strong field intensity.

However, the ferromagnetic material can lose its ferromagnetic properties under thermal agitation, the temperature that characterizes this phenomenon is known as the “Curie temperature (T_c)”, above which spontaneous ferromagnetism becomes paramagnetism which owns a small, positive susceptibility to magnetic fields and can’t keep this magnetic property after removal of the external field. When such a material is cooled down and crosses the Curie temperature, it undergoes a phase transition from a non-ferroic to ferroic state. These transitions are generally accompanied with a lowering of the crystal symmetry. For example, bulk $BaTiO_3$ an archetypal ferroelectric presents a transition from a cubic paraelectric structure to a tetragonal ferroelectric structure around 120°C .

Ferroelectricity and ferroelasticity are analogous to ferromagnetism. Polarization and strain are induced by externally applied electric field and mechanical stress respectively. They both show hysteresis loops with spontaneous electric polarization and strain, as depicted in figure 2-1 (a) and (c). Figure 2-2 shows how ferroelectrics and ferromagnetics permit the orientations of electrical polarization and magnetization to be reversed by applying an electric field and magnetic field, respectively.

Actually, the discovery of ferroelectricity can date back to the early 20th century when ferromagnetism had already been discovered. Since the appearance of hysteresis loops from ferroelectricity and ferromagnetism look quite similar, the prefix ferro- was continuously carried forward to describe ferroelectricity, though many ferroelectric materials have nothing to do with iron either.

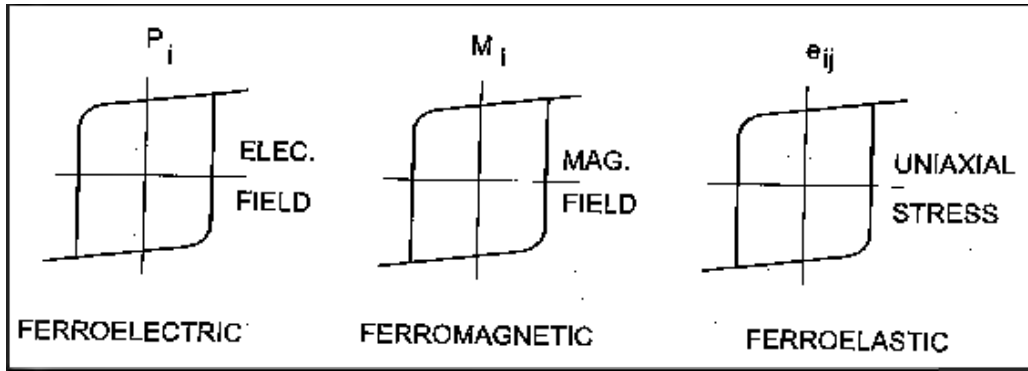


Figure 2-1: Hysteresis loops of (a) ferroelectric, (b) ferromagnetic and (c) ferroelastic materials. Adapted from [9]

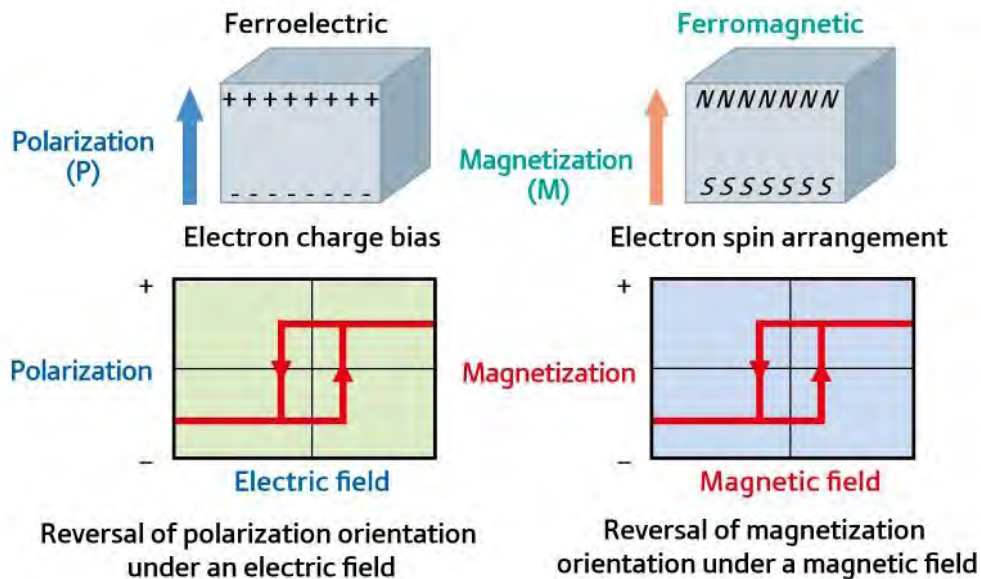


Figure 2-2: Schematic representation of ferroelectric and ferromagnetic characteristics. Ferroelectrics and Ferromagnetics permit the orientations of electrical polarization and magnetization to be reversed by applying an electric field and magnetic field, respectively. Adapted from [41]

The strong interaction between electrical and magnetic dipoles results in small regions within the material in which the ferroic property is uniform, with the dipoles arranged parallel to each other. Such regions are known as domains and are separated by domain walls, whereby the dipoles undergo a coherent rotation from the direction in one domain to that in the adjacent domain. Due to the random orientation of the magnetic and electrical dipoles of different domains in the absence of an external stimulus, the total net polarization and magnetization is zero for ferroic materials. Ferroic properties depend on external conditions such as: magnetic

field, electric field, pressure and temperature. The existence of domain structures is also responsible for the hysteretic response of the ferroic properties of the material when an external stress is applied. As a result, ferroic materials have the unique ability to store and release energy in the form of magnetic and electrical energy, an attribute which made them very attractive to different technologies. Based on the above information, characteristics of ferroic materials are presented schematically in figure 2-3 (a-c). In the following discussion, concepts of the ferroelectrics and ferro (ferri) magnetic materials will be discussed in detail.

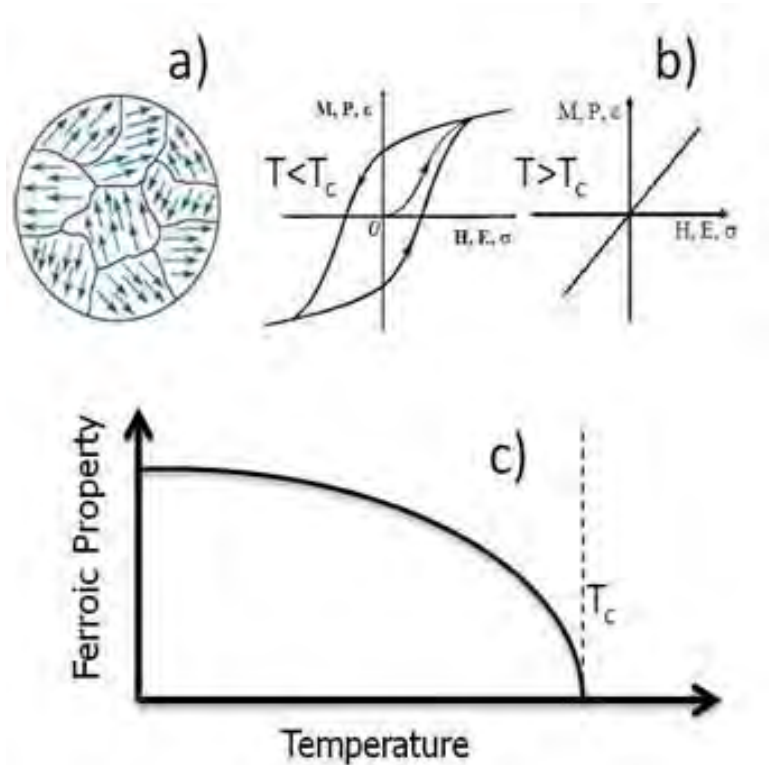


Figure 2-3: Characteristics of ferroic materials a) Ordering of physical properties, b) Hysteretic behavior and c) Existence of ferroic properties below a threshold temperature. Adapted from [42]

2.1.1. Ferroelectric Materials

Ferroelectricity (FE) was first discovered in Rochelle salt in 1921. At that time, it was called Seignette-electricity, honoring its discoverer. For the past few decades, ferroelectric materials have received a great amount of interests because of their various uses in many applications such as nonvolatile ferroelectric random access memories (NVFRAM), dynamic random access memories, sensors and microactuators [42].

A crystal is said to be ferroelectric when it possesses at least two equilibrium orientations of the spontaneous polarization vector in the absence of an external electric field, and the spontaneous polarization can be switched between those orientations by an electric field. The polar character of the orientation states should represent an absolutely stable configuration in a null field [43].

Among the thirty-two crystal classes, eleven of them are characterized by the existence of a center of symmetry. The remaining twenty-one crystal classes do not have a center of symmetry. Thus, it is possible for the 21 groups to (i) have one or more polar axes, and (ii) possess odd-rank tensor properties. The only exception is the group 432, which lacks a center of symmetry, but has other symmetry operations that destroy polarity. *All non-centrosymmetric point groups exhibit piezoelectric effect that is defined by a change in electric polarity under applied stress, and vice versa.* Out of the twenty piezoelectric classes, ten possess a unique polar axis, the spontaneous polarization of which depends on temperature. This is called the pyroelectric effect. Ferroelectric crystals belong to the pyroelectric family, which in addition has a spontaneous polarization can be reversed by external electric field, i.e. more than one equivalent direction for Ps [44].

Among all ferroelectric materials, the most extensively studied and widely used are the perovskite. A perfect perovskite structure has a general formula of ABO_3 , where A represents a divalent or trivalent cation, and B is typically a tetravalent or trivalent cation. The origin of ferroelectricity in this family of materials can be explained using the well-known example of barium titanate ($BaTiO_3$). As shown in figure 2-4 b), the Ba^{2+} cations are located at the corners of the unit cell. A dipole moment occurs due to relative displacements of the Ti^{4+} and O^{2-} ions from their symmetrical positions.

A (proper) ferroelectric possesses a spontaneous polarization of the electric dipole which can be switched by the application of an electric field. This polarization is due to a lack of inversion symmetry within the crystal structure. For example, consider the most extensively studied and widely used classic perovskite of the form ABO_3 , in which a central positive B-ion (a transition metal element) is surrounded by an octahedron of negatively charged oxygen ions (figure 2-4 a)). A shift in the position of the B-site ion would break the inversion symmetry and cause the induction of a dipole moment, giving rise to ferroelectric order. Such shifts can occur during structural phase transitions, in which the system moves from a high to low symmetry state (e.g. cubic to tetragonal). One of the best known examples of a proper ferroelectric is $BaTiO_3$. As shown in figure 2-4 b), the Ba^{2+} cations are located at the corners of the unit cell. A dipole moment occurs due to relative displacements of the Ti^{4+} and O^{2-} ions from their symmetrical positions.

In the majority of ferroelectric perovskites, the B-site atom has an empty d electron shell, which allows covalent bonding with the full p orbitals of the oxygen atoms. Ferroelectricity can also

occur due to the existence of lone pairs of electrons on the outer shell of the A-site atom, which are highly susceptible to polarization. This is the cause of ferroelectricity in BiFeO_3 .

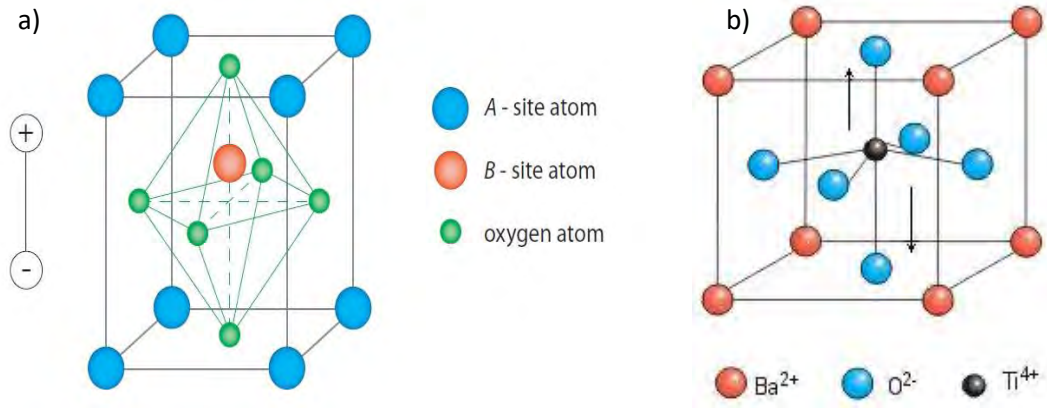


Figure 2-4: a) Perovskite crystal structure, showing a dipole moment generated by a displaced B-site atom; b) An example of Perovskite crystal structure (BaTiO_3). Adapted from [41]

In an improper ferroelectric, the spontaneous polarisation is not due to a polar displacement of the ions, but occurs as a result of some other effect within the material. In a geometric ferroelectric, the dipole moment occurs due to non-polar lattice distortions, due to e.g. electrostatic forces rather than changes in chemical bonding. An example of this is in YMnO_3 , where a ferroelectric state is due to a buckling of the rigid MnO_5 bipyramids. In charge ordered ferroelectrics, the spontaneous polarisation is dependent on electron correlations in the material. Such charge ordered ferroelectricity is observed in LuFe_2O_4 . Improper ferroelectricity can also occur due to magnetic order.

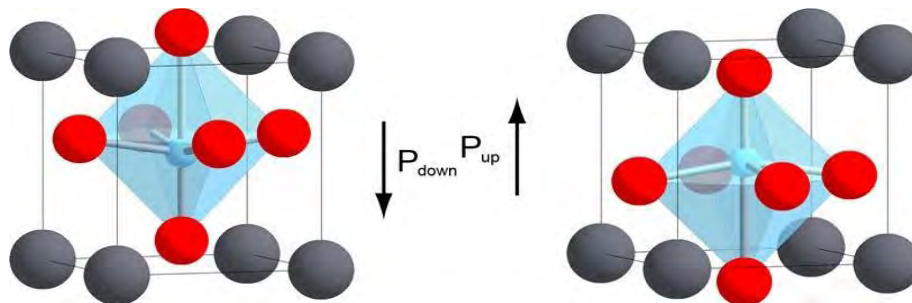


Figure 2-5: Elementary cell of PbTiO_3 in the 'up' and 'down' spontaneous polarization states. Adapted from [44]

2.1.2. Ferro-, Antiferro-, and Ferri-magnetic Materials

The phenomenon of magnetism has been known to mankind for many thousands of years. Lodestone (Fe_3O_4) was the first permanent magnetic material to be identified and studied. The magnetic moment of an atom/ion has three principal sources: (1) the spin of electrons; (2) electron orbital angular momentum about the nucleus; and (3) a change in the orbital moment induced by an applied magnetic field. The first two effects give paramagnetic contributions to the magnetization, and the third gives a diamagnetic contribution [45].

In a crystal, the overall magnetic property depends on two factors: (i) the magnetic response associated with each atom/ion, and (ii) the interactions between these magnetic moments. In the case that there are no unpaired electrons around each atom/ion, there will be no net magnetic moments associated with them (bearing in mind that both orbital moments and electron spins cancel to zero in a fully filled orbital), diamagnetic behavior will be shown by the material. When there are unpaired electrons, every atom/ion has a net magnetic moment. Depending on the interactions between the magnetic dipoles, the material may show (i) paramagnetism (PM); (ii) ferromagnetism (FM); (iii) antiferromagnetism (AFM) and (iv) ferrimagnetism (FIM). In a paramagnetic material, alignment of adjacent moments is not observed due to thermal fluctuation. Ferromagnetism consists of parallel aligned adjacent moments. Antiferromagnetic order consists of antiparallel aligned equal moments. And, ferrimagnetic order consists of antiparallel unequal moments, resulting in a non-zero net magnetization.

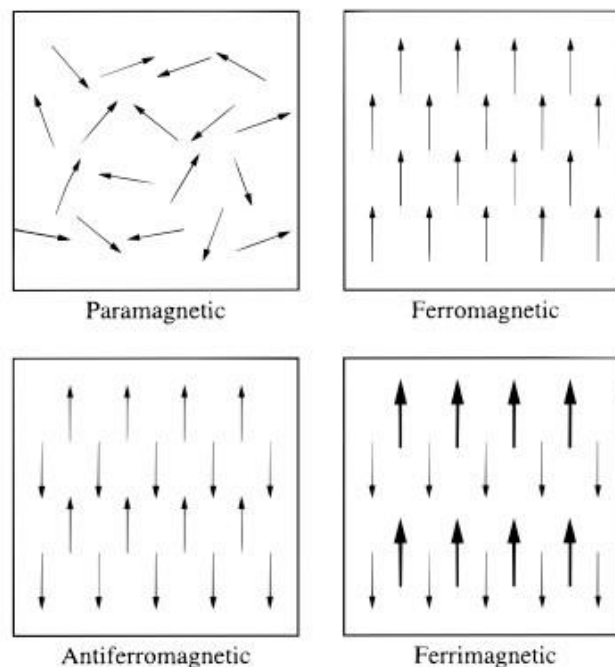


Figure 2-6: Common examples of magnetic dipole ordering, from [9].

Ferromagnetism is a very strong magnetic response compared with paramagnetic and diamagnetic behaviors. It is characterized by a transition temperature (Neel temperature, T_N). Above this temperature, the material is paramagnetic. Below this temperature, it is ferromagnetic. The magnetic susceptibility, $\chi = M/H$, which defines the degree of magnetization of a material in response to a magnetic field, is a good indication of their magnetic properties. If χ is positive the material is paramagnetic, and the magnetic field is strengthened by the presence of the material. If χ is negative then the material is diamagnetic and the magnetic field is weakened in the presence of the material. The magnetic susceptibility of a ferromagnetic substance is not linear.

2.1.3. Ferroelastic Materials

Ferroelastic materials develop a spontaneous strain below a phase transition temperature. From the symmetry point of view, the material undergoes a structural phase transition from a high symmetry phase to a low symmetry phase, which is characterized by a 'broken symmetry' of the high symmetry phase [46].

The phase transition mechanism results in a spontaneous strain. The spontaneous strain can be quite large. For example, the spontaneous strain of a typical ferroelastic material is >2%. The correlated changes in the enthalpy of the crystal related to this formation of spontaneous strain often reach some 6 KJ/mole, an energy which would reactive equivalent changes in thermochemical phase diagrams of some hundreds of degrees in temperature. In order to release the energy created by the phase transition, a twin domain structure is often created within a ferroelastic crystal, where the dominant twin planes are oriented approximately perpendicular to each other.

A wall between two adjacent domains can be envisaged as an internal surface of the crystal. The orientation of an individual twin wall is then determined by the condition that the crystal in the low-symmetry phase tends to maintain the total symmetry of the high-symmetry phase as an average. The domains are related equivalent to each other via the symmetry element lost at the phase transition that give rise to the long-range ordered state. It is commonly accepted that stress induced domain wall motion in ferroelastic materials yield hysteretic macroscopic behavior. Mueller et al. [47] showed that nonlinear effects in ferroelastic crystals are related to the properties of ferroelastic domain walls pinned on defects, which became de-pined above a critical stress level. Additionally, Jian and Wayman [48] observed domain wall motion in single crystal and polycrystalline LaNbO_4 ferroelastics under stress, and argued that the nonlinear elastic behavior is a direct result of domain wall motion, rather than the intrinsic properties of the crystal. In addition, Newnham [49] concluded that stress-induced movement of domain

walls is the principle source of hysteresis in ferroelastics. A complete analysis of twin structure and domain wall can be seen in reference [47]. Figure 2-7 illustrates the stress-induced twin movement of a ferroelasteic $\text{Pb}_3(\text{Pb}_4)_2$ crystal [47].

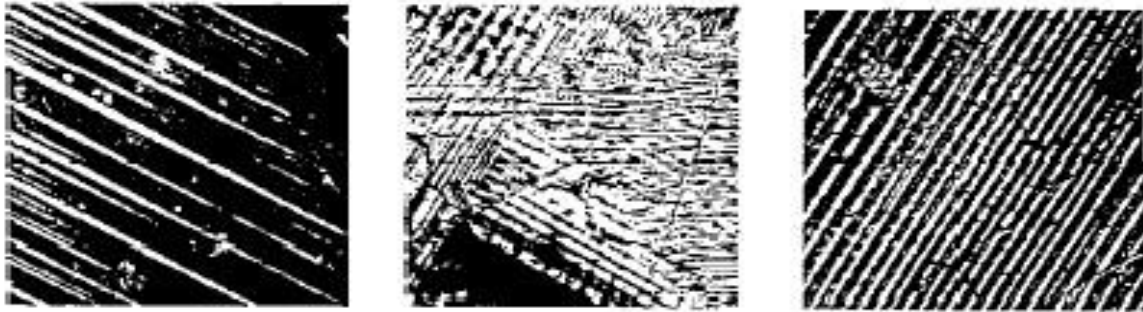


Figure 2-7: Experimentally observed microstructures of lead phosphate. The two fully ‘switched’ crystals (a) and (c) display striped twin patterns whereas the crystal in the intermediate state (b) shows superposition of various twin orientations. Adapted from [47]

2.2. Order parameter couplings

There are four order parameters. The order parameter couplings are given below:

- **Piezoelectricity:** describes a change in strain as a linear function of applied electric field, or a change in polarization as a linear function of applied stress.
- **Piezomagnetism:** describes a change in strain as a linear function of applied magnetic field, or a change in magnetization as a linear function of applied stress.
- **Magnetolectricity:** describes the influence of a magnetic (electric) field on the polarization (magnetization) of a material.
- **Electrostriction:** describes a change in strain as a quadratic function of applied electric field.

The effects of cross-coupling between ferroic orders is, represented in figure 2-8 Changes in strain as a function of an electric or magnetic field are shown by the black arrows, and the magnetoelectric coupling between the ferroelectric and ferromagnetic orders is shown by the green arrows.

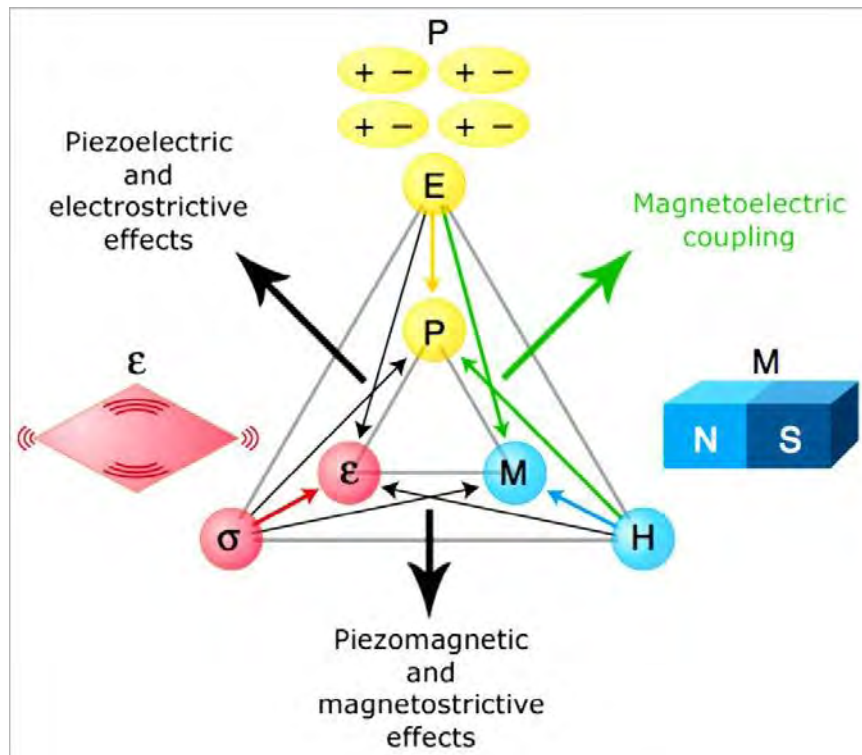


Figure 2-8: Ferroic orders and possible couplings between them. Adapted from [54]

2.3. Multiferroics

Multiferroic materials are single-component materials or composites exhibiting two or more ferroic properties such as ferromagnetism, ferroelectricity, or ferroelasticity, as shown in figure 2-9. In a broader definition, it also covers materials with ferro- and antiferro- orders. There are significant scientific and technological interests in these materials due to their unusual responses, including very large magneto-electric susceptibility, giant magnetostriction, and energy coupling coefficients [50, 51]. In addition, the ability to couple between the spontaneous order parameters offers extra degrees of freedom in the design of conventional devices. Examples of single component multiferroics are BiFeO_3 (a ferromagnetic/ferroelectric perovskite), and Fe-Ga (a ferromagnetic/ferroelastic alloy).

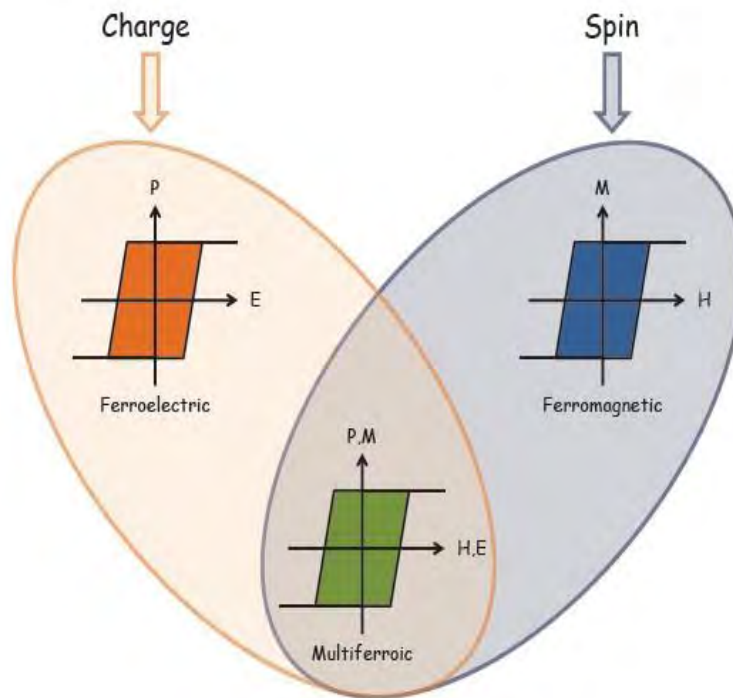


Figure 2-9: Multiferroics materials are those that present more than one ferroic order. Multiferroics combining ferroelectric (left- orange) and ferromagnetic (right- blue) properties are very appealing materials because the possible presence of magnetoelectric coupling (magnetic control of polarization or electric control of magnetization, bottomgreen) can give rise to new technological functionalities. Adapted from [4]

The ability to combine magnetic and ferroelectric properties within one material and the potential functionality that can be achieved has resulted in much of the early work on multiferroics being concentrated within magnetic ferroelectrics [52]. Combining these two properties has, however, proven to be difficult. Normally, these two order parameters are mutually exclusive; yet a number of materials have simultaneously presented magnetic and ferroelectric properties. Coupling of the parameters within the multiferroic system tends to be weak. The microscopic mechanisms of magnetism and ferroelectricity are very different from each other therefore do not strongly interfere [4].

2.3.1. Classification of Multiferroics

The microscopic origin of magnetism is basically the same in all magnets: it is the presence of localized electrons, mostly in the partially filled d or f shells of transition-metal or rare-earth ions, which have a corresponding localized spin, or magnetic moment. Exchange interactions between the localized moments lead to magnetic order. The situation with ferroelectrics is quite

different. There are several different microscopic sources of ferroelectricity, and accordingly one can have different types of multiferroics.

Broadly, multiferroics can be classified as single-phase or composite multiferroics. Generally speaking, there are two groups of multiferroics. Single-phase multiferroics are those materials that show both ferroelectric and ferromagnetic order [53-58]. Thus, multiferroicity is intrinsic of the material. The scarcity of single phase multiferroic materials makes composite materials an interesting alternative. In opposition to single-phase multiferroics, multiferroic order is not intrinsic but results from the combination of two materials that are ferroelectric and ferromagnetic, separately. Therefore, the availability of ferromagnetic and ferroelectric materials at room temperature makes easy to obtain multiferroic composite materials at room temperature.

Single-phase multiferroics can be further classified into two groups. The first group, called type-I multiferroics, contains those materials in which ferroelectricity and magnetism have different sources and appear largely independently of one another, though there is some coupling between them. In these materials, ferroelectricity typically appears at higher temperatures than magnetism, and the spontaneous polarization P is often rather large (of order 10^{-100} $\mu\text{C}/\text{cm}^2$).

Examples are BiFeO_3 ($T_{\text{FE}} \sim 1100\text{K}$, $T_{\text{N}} = 643 \text{ K}$, $P \sim 90\mu\text{C}/\text{cm}^2$) and YMnO_3 ($T_{\text{FE}} \sim 914\text{K}$, $T_{\text{N}} = 76 \text{ K}$, $P \sim 6\mu\text{C}/\text{cm}^2$). The second group, which we can call type-II multiferroics, is the relatively recently discovered materials [59, 60], in which magnetism causes ferroelectricity, implying a strong coupling between the two. However, the polarization in these materials is usually much smaller ($10^{-2}\mu\text{C}/\text{cm}^2$). Many groups are also investigating composite multiferroics that consist of known magnets and ferroelectrics in the form of multilayers and self-organized nanostructures [53].

2.3.1.1. Type-I multiferroics

Type-I multiferroics are “older” and more numerous. These are often good ferroelectrics, and the critical temperatures of the magnetic and ferroelectric transitions can be well above room temperature. Unfortunately, the coupling between magnetism and ferroelectricity in these materials is usually rather weak. The materials challenge for this group of multiferroics is to keep all their positive features, but enhance this coupling., The opposite problem exists for type-II multiferroics will be seen later. One can single out several different subclasses of type-I multiferroics, depending on the mechanism of ferroelectricity in them. Four of the major subclasses will be focused but there are certainly others.

I. Ferroelectricity due to lone pairs

In BiFeO_3 , and probably in BiMnO_3 and PbVO_3 , Bi^{3+} and Pb^{2+} play the major role in the origin of ferroelectricity. In these ions, there are two outer 6s electrons that do not participate in chemical

bonds. They are called lone pairs, or sometimes dangling bonds. They have a high polarizability—the condition required for ferroelectricity in the classical description. These electrons generate an electric dipole, which is the origin of ferroelectric order. Other cations (i.e. Fe^{3+} , Mn^{3+} , Ni^{2+}) are responsible for magnetic properties. More microscopically one can explain the origin of ferroelectricity in these compounds by ordering of these lone pairs (with certain admixture of p orbitals) in one direction (figure 2-10). Apparently this is what happens in many Bi- and Pb-containing ferroelectrics and multiferroics such as BiFeO_3 , but it also helps to improve the ferroelectric properties of $\text{Pb}[\text{Zr}_x\text{Ti}_{(1-x)}]\text{O}_3$.

II. Ferroelectricity due to charge ordering

One more mechanism that can lead to ferroelectricity and to type-I multiferroicity can be charge ordering, often observed in transition metal compounds, especially those formally containing transition metal ions with different valence. If, after charge ordering, both sites and bonds turn out to be inequivalent, this can lead to ferroelectricity [figure 2-10]. A corresponding mechanism can work in systems like $\text{Pr}_{1/2}\text{Ca}_{1/2}\text{MnO}_3$ or in nickelates RNiO_3 with charge ordering. But more often we meet the situation in which there exist ions with different charge (often because they are different elements), but on top of that there occurs dimerization.

TbMn_2O_5 belongs to this class, as does the newly discovered multiferroic $\text{Ca}_3\text{CoMnO}_6$. Another similar possibility is when the bonds are inequivalent because of the structure of the material, the site-centered charge order appearing on top of that. This is the case in an organic ferroelectric $(\text{TMTTF})_2\text{X}$, and also in the multiferroic LuFe_2O_4 .

III. Multiferroic perovskites

Probably the best-known ferroelectrics are the perovskites like BaTiO_3 or $\text{Pb}(\text{ZrTi})\text{O}_3$ (PZT). There are many magnetic materials among perovskites [61], and also many ferroelectrics [62]. But comparing these extensive compilations, each containing more than 100 pages of tables, demonstrates that there seems to be mutual exclusion of magnetism and ferroelectricity in perovskites: there is practically no overlap of these tables. Why? Whereas for magnetism one needs partially filled d shells of a transition metal, practically all ferroelectric perovskites contain transition metal ions with an empty d shell, such as Ti^{4+} , Ta^{5+} , W^{6+} . Ferroelectricity in these systems is caused by the off-center shifts of the transition metal ion, which forms strong covalent bonds with one (or three) oxygens, using their empty d states. And somehow, the presence of real d electrons in d^n configurations of magnetic transition metals suppresses this process, preventing ferroelectricity in magnetic Perovskites. This so called " d^0 vs. d^n problem" was one of the first to be studied theoretically at the beginning of the recent revival of multiferroics [5,63], and although there has been some progress, largely from ab initio

calculations, still in my opinion there is no full solution of this problem[59]. The answer may well lie in the fact that this mutual exclusion is not a “theorem,” but rather a matter of numbers: in most cases a magnetic d^n ion is stable in the center of its O_6 octahedra, but there may still be the cases where it is not. One possible way around this problem may be making” mixed” perovskites with d^0 and d^n ions, refer (Figure 2.10). Unfortunately, the coupling of magnetic and ferroelectric subsystems in mixed perovskites is rather weak.

IV. “Geometric” ferroelectricity

Lastly, we consider a case realized in, for example, $YMnO_3$ [64]. Ferroelectricity in $YMnO_3$ has nothing to do with the magnetic Mn^{3+} , but is caused by the tilting of the practically rigid MnO_5 block. This tilting occurs just to provide closer packing, and as a result the oxygen ions move closer to the rather small Y ions (figure 2-10).

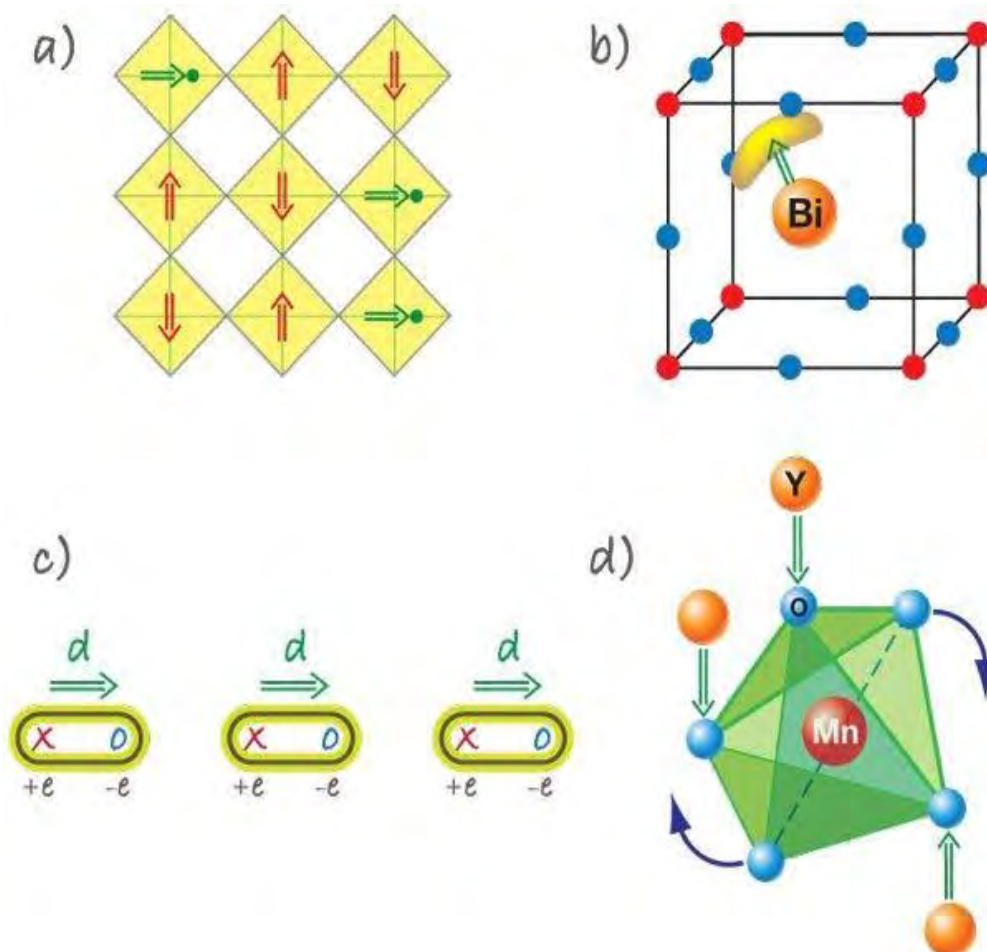


Figure 2-10: Different microscopic mechanisms found in type-I multiferroics. Adapted from [64]

2.3.1.2. Type-II multiferroics: Magnetic multiferroics

The biggest excitement nowadays is caused by the discovery of a novel class of multiferroics in which ferroelectricity exists only in a magnetically ordered state and is caused by a particular type of magnetism. For example, in TbMnO_3 magnetic ordering appears at $T_{N1} = 41$ K, and at a lower temperature, $T_{N2} = 28$ K, the magnetic structure changes. It is only in the low temperature phase that a nonzero electric polarization appears. Similar behavior occurs in TbMn_2O_5 . The first paper to study TbMnO_3 showed that a magnetic field can strongly influence the electric polarization: e.g., in TbMnO_3 the polarization rotates (or “flops”) by 90 degrees when a critical magnetic field is applied along a certain direction [65]. In TbMn_2O_5 [66] the influence of an external field is even stronger: the polarization changes sign with field, and a field alternating between +1.5 and -1.5 Tesla leads to corresponding oscillations in the polarization. Since the discovery of these materials, a number of other type-II multiferroics with strong magnetoelectric coupling have been discovered and studied. From the point of view of the mechanism of multiferroic behavior, one can divide type-II multiferroics into two groups: those in which ferroelectricity is caused by a particular type of magnetic spiral and those in which ferroelectricity appears even for collinear magnetic structures.

a) Spiral magnets

Spiral magnets are those where atomic spin rotate across the lattice in a defined plane, this breaks the symmetry and allows ferroelectricity. However, ferroelectricity only takes place in spiral magnets when the so-called cycloidal spin arrangement set, that is spins rotate in the plane of the propagation of the spiral. In this case, ferroelectricity arises in the plane of the cycloid and perpendicular to the propagation vector of the cycloid due to the so-called inverse Dzyaloshinsky-Moriya interaction ($P = A \sum r_{ij} \times (S_i \times S_j)$, being r_{ij} the vector connecting the S_i and S_j spins). Here, sizable spin-orbit interaction is needed (A), if A is large the magnetoelectric coupling is strong. The cycloid is sensible to the application of a magnetic field, which can produce rotation of cycloid plane by 90 (so-called flopping), inducing a change in the direction of o the ferroelectric polarization. TbMnO_3 is the archetype of this class of 3 multiferroic materials [67].

b) Collinear magnets

In these materials one-dimensional chains of up-up- down-down spins are formed due to the exchange striction. The distortion induced by up-up (down-down) or up-down (down-up) bonds is different, which provokes the formation of ordered electric dipoles. An example is $\text{Ca}_3\text{CoMnO}_6$ [68], or E-type rare earth manganites [69], f.i. HoMnO_3 [70].

2.3.2. Why is it difficult to find materials that are both ferroelectric and magnetic?

Most ferroelectrics are transition metal oxides, in which transition ions have empty d shells. These positively charged ions like to form 'molecules' with one (or several) of the neighbouring negative oxygen ions. This collective shift of cations and anions inside a periodic crystal induces bulk electric polarization. The mechanism of the covalent bonding (electronic pairing) in such molecules is the virtual hopping of electrons from the filled oxygen shell to the empty d shell of a transition metal ion. Magnetism, on the contrary, requires transition metal ions with partially filled d shells, as the spins of electrons occupying completely filled shells add to zero and do not participate in magnetic ordering. The exchange interaction between uncompensated spins of different ions, giving rise to long range magnetic ordering, also results from the virtual hopping of electrons between the ions. In this respect the two mechanisms are not so dissimilar, but the difference in filling of the d shells required for ferroelectricity and magnetism makes these two ordered states mutually exclusive.

Still, some compounds, such as BiMnO_3 or BiFeO_3 with magnetic Mn^{3+} and Fe^{3+} ions, are ferroelectric. Here, however, it is the Bi ion with two electrons on the 6s orbital (lone pair) that moves away from the centrosymmetric position in its oxygen surrounding. Because the ferroelectric and magnetic orders in these materials are associated with different ions, the coupling between them is weak. For example, BiMnO_3 shows a ferroelectric transition at $T_{\text{FE}} \approx 800$ K and a ferromagnetic transition at $T_{\text{FM}} \approx 110$ K, below which the two orders coexist. BiMnO_3 is a unique material, in which both magnetization and electric polarization are reasonably large. This, however, does not make it a useful multiferroic. Its dielectric constant ϵ shows only a minute anomaly at T_{FM} and is fairly insensitive to magnetic fields: even very close to T_{FM} , the change in ϵ produced by a 9-T field does not exceed 0.6%.

2.3.2.1. Requirements for magnetoelectric multiferroicity

By definition, for a material to be a magnetoelectric multiferroic, it must be simultaneously ferromagnetic and ferroelectric. Therefore, its allowed physical, structural, and electronic properties are restricted to those that occur both in ferromagnetic and in ferroelectric materials. In this section, we analyze a range of properties and discuss how these properties limit our choice of potential materials. We discuss those that are the limiting factors in preventing the simultaneous existence of ferromagnetism and ferroelectricity.

i. Symmetry

A primary requirement for the existence of ferroelectricity is a structural distortion from the prototypical high-symmetry phase that removes the center of symmetry and allows an electric polarization. There are 31 point groups that allow a spontaneous electric polarization, P, and 31 that allow a spontaneous magnetic polarization, M [71]. Thirteen-point groups (1, 2, 2C, m, mC, 3, 3mC, 4, 4mCmC, mCm2C, mCmC2C, 6, and 6mCmC) are found in both sets, allowing both properties to exist in the same phase. Although this represents a considerable reduction from the total number of possible crystal structures (the total number of Shubnikov point groups is 122), it is not an insignificant number, and many candidate materials that are not in fact ferromagnetic and ferroelectric exist in one of the allowed symmetries. Therefore, it is unlikely that symmetry considerations are responsible for the scarcity of ferromagnetic ferroelectric materials.

ii. Electrical Properties

By definition, a ferroelectric material must be an insulator (otherwise, an applied electric field would be inducing an electric current to flow, rather than causing an electrical polarization.) Ferromagnets, although not required to have specific electrical properties, are often metals. For example, the driving force for ferromagnetism in the elemental ferromagnets Fe, Co, and Ni and their alloys is the high density of states at the Fermi level, which also, of course, results in metallicity. Therefore, one could assume that the lack of the simultaneous occurrence of magnetic and ferroelectric ordering is simply the result of a dearth of magnetic insulators. However, if we extend our search to include ferrimagnets or weak ferromagnets (which have canted antiferromagnetic ordering, resulting in a weak magnetic moment in the direction of the canting), this argument no longer holds, because most ferrimagnets or weak ferromagnets are, in fact, insulators. In addition, there are also very few antiferromagnetic ferroelectrics, even though antiferromagnets are usually insulating materials. Therefore, it appears that we cannot blame the lack of magnetically ordered ferroelectrics simply on a shortage of magnetically ordered insulators.

iii. Chemistry

“d⁰-ness”: The common perovskite oxide ferroelectric materials have a formal charge corresponding to the d⁰ electron configuration on the B cation. Clearly, if there are no d electrons creating localized magnetic moments, then there can be no magnetic ordering of any type, either ferro-, ferri-, or antiferromagnetic. It appears however that, in most cases, as soon as the d shell on the small cation is partially occupied, the tendency for it to make a distortion that

removes the center of symmetry is eliminated. This could be the result of a number of effects, including size, the tendency to undergo a different, more dominant distortion, electronic properties, magnetic properties, or some combination of the above. We now consider the likely influence of each of these factors.

1) Size of the Small Cation: Are transition metal ions with occupied d shells simply too large to move away from the large space at the center of the oxygen octahedron? In this section, we compare the ionic radii of typical d_0 cations in perovskite ferroelectrics with those of typical d_n cations in nonferroelectric perovskite oxides to see if this argument is correct. The Shannon ionic radii [72] of some common d_0 small cations found in ferroelectric perovskite oxides are: Ti^{4+} , 74.5 pm; Nb^{5+} , 78 pm; and Zr^{4+} , 86 pm. Some representative d_n cations that are found as the small cations in nonferroelectric perovskite oxides include Mn^{3+} (d^4), Ti^{3+} (d^1), and V^{4+} (d^1) with radii of 78.5, 81, and 72 pm, respectively. Therefore, typical B-site cations with d electron occupation do not have systematically larger radii than typical d_0 B-site cations. We conclude that the size of the B cation is not the deciding factor in the existence or otherwise of ferroelectricity.

2) Structural Distortions: Ferroelectric materials must undergo a phase transition to a low temperature phase that does not have a center of symmetry. This is most often achieved in conventional perovskite ferroelectrics by an off-center displacement of the small (B) cation from the center of the oxygen octahedron. However, for cations with certain d orbital occupancies, the tendency to undergo a Jahn-Teller distortion is strong and will likely be the dominant structural effect. The Jahn-Teller distorted structure might have a lower driving force for off-center displacement than the otherwise undistorted structure.

Examples of this effect are seen in lanthanum manganite, $LaMnO_3$, in which the Mn^{3+} ion has a d^4 configuration, and yttrium titanate, $YTiO_3$, in which the Ti^{3+} ion is d^1 . Both materials have a d-type Jahn-Teller distortion, in which the elongated axes of the oxygen octahedra are oriented parallel to each other along the crystallographic c axis

[73] Orbital ordering is observed to occur simultaneously with the Jahn-Teller ordering [73]. LaMnO_3 is insulating and an A-type antiferromagnet, in which planes of ferromagnetically aligned Mn^{3+} ions are aligned antiparallel to each other. YTiO_3 is a strongly correlated ferromagnetic Mott-Hubbard insulator. Neither material is ferroelectric.

Note the relevance of the formal charge on the B cation here. In BaTiO_3 , the actual occupation of the 3d electrons is closer to d^1 than to d^0 because of donation of charge density from the oxygen ligands [74]. A d^1 cation should undergo a Jahn-Teller distortion. No Jahn-Teller distortion is observed in BaTiO_3 however, which is consistent with the d^0 formal charge.

3) Magnetism Versus d-Orbital Occupancy: It is clear that the existence of d electrons on the B-site cation reduces the tendency of perovskite structure oxides to display ferroelectricity. However, it is not clear whether it is merely the presence of d electron density or the influence of the magnetic spin polarization that is the dominant factor in creating this effect. Using first principles density functional theory calculations, it is possible to answer this question by artificially removing the spin polarization in materials that are experimentally found to be magnetic and determining whether they then become ferroelectric. Comparisons for some representative systems and show that removal of the magnetic polarization does not significantly affect the calculated phonon frequencies, suggesting that d-orbital occupancy, rather than d-electron magnetism, is dominant in overriding the tendency to undergo ferroelectric distortion.

2.3.2.2. Conclusion

We do not know for sure why there are so few magnetic ferroelectrics. We do, however, have some clues: multiferroism involves a number of subtle competing factors, with d-electron occupancy on the transition metal being a critical variable.

2.4. BiFeO₃ multiferroics

Bismuth ferrite (BFO) is one of the most interesting members of multiferroic family which shows both ferroelectric and ferromagnetic properties in a single phase at room temperature. It is one of the few multiferroics that has Curie and Neel temperatures far above room temperature. It shows magnetoelectric coupling at room temperature and such coupling is strongly enhanced by proper dopings.

2.4.1. History of BiFeO₃

The basic idea that crystals could be simultaneously ferromagnetic and ferroelectric probably originated with Pierre Curie in the 19th century [75]. After switching was discovered in ferroelectric Rochelle Salt by Valasek in 1920 [76] there was a rash of supposed discoveries of magnetoelectric properties by Perrier [77, 78], but unfortunately in materials such as Ni in which they are now understood to be impossible. A history of this period of solid-state physics is given in O' Dell's text [79].

True magnetoelectricity –defined as a linear term in the free energy was first understood theoretically by Dzyaloshinskii [80] with special predictions being made for Cr₂O₃ and discovered experimentally in that material by Astrov [81]. However, this material is paraelectric and antiferromagnetic, making microelectronics applications impractical.

The more interesting case of ferromagnetic ferroelectrics waited for some years until the work of Schmid on boracites [82]. The boracites are also impractical materials for device applications: they have low symmetry with large unit cells and grow in needle shapes; more importantly, they exhibit magnetoelectricity only at extremely low temperatures. Meanwhile Smolenskii's group in Leningrad pioneered [83] the study of bismuth ferrite, BiFeO₃, but they found that they could not grow single crystals and that ceramic specimens were too highly conducting (probably caused by oxygen vacancies and mixed Fe valences) to be used in applications [84]. They tried to address the conductivity problem by doping other ions into both the A and B sites of the lattice.

Reviews of the general study of magnetoelectricity appeared by Schmid in 1994 [85] and more recently by Fiebig [86] and by Eerenstein et al. [87]. The current interest in bismuth ferrite was stimulated primarily by a 2003 paper from Ramesh's group [88], which showed that it had unexpectedly large remnant polarization. At any rate, the 2003 Science paper has proved enormously stimulating, and has inspired both new fundamental physics and exciting device applications. Increasing efforts have now been devoted to the research focusing on the preparation and characterization of BiFeO₃ in forms of film, bulk and nanostructure.

2.4.2. Science of BiFeO₃

In parallel with the specific investigation of bismuth ferrite and related compounds has been a more general approach to the idea of multiferroics. Nicola Hill (now Spaldin) has asked [5] why there are so few materials that are magnetic and ferroelectric; implicitly limiting her discussion to transition-metal oxides, especially perovskites, she observed that the ferroelectrics (e.g., titanates) have B-site ions with d^8 electrons,[89] whereas the magnets require d^j electrons with j different from zero.

However, oxide perovskites do not all have the same mechanism of ferroelectricity: the center Ti ion plays the key role in BaTiO₃ but the lone-pair Pb ion is dominant in PbTiO₃. [89] Indeed, this seems to be the case in BiFeO₃, where the polarization is mostly caused by the lone pair (s^2 orbital) of Bi³⁺, so that the polarization comes mostly from the A site while the magnetization comes from the B site (Fe³⁺); this same idea has led Spaldin and co-workers to propose a host of other perovskites with possible A-site ferroelectricity and B-site magnetism, such as Bi(Cr,Fe)O₃ and BiMnO₃.

2.4.2.1. Structure of BiFeO₃

The room-temperature phase of BiFeO₃ is classed as rhombohedral (point group R3c).[59] The perovskite-type unit cell has a lattice parameter, a_{rh} , of 3.965 Å and a rhombohedral angle, α_{rh} , of 89.3–89° at room temperature [90,91] with ferroelectric polarization along [111]_{pseudocubic} [92].

A very important structural parameter is the rotation angle of the oxygen octahedra. This angle would be 0° for a cubic perovskite with perfectly matched ionic sizes. A measure of how well the ions fit into a perovskite unit cell is the ratio $(r_{Bi} + r_O)/l$, where r is the ionic radius of the respective ion and l is the length of the octahedral edge. This is completely analogous to the commonly used Goldschmidt tolerance factor, [91] which is defined as $t = (r_{Bi} + r_O)/(r_{Fe} + r_O)$. For BiFeO₃ we obtain $t=0.88$ using the ionic radii of Shannon, [93] with Bi³⁺ in eightfold coordination (the value for 12-fold coordination is not reported) and Fe³⁺ in sixfold coordination and high spin. When this ratio is smaller than one, the oxygen octahedra must buckle in order to fit into a cell that is too small. For BiFeO₃, ω is ca. 11–14° around the polar [111] axis [91, 93]. The displacement of the A-site bismuth cation (shown in figure 2-11) along the [111] axis brings about a non-centrosymmetric polarization resulting in the ferroelectric property.

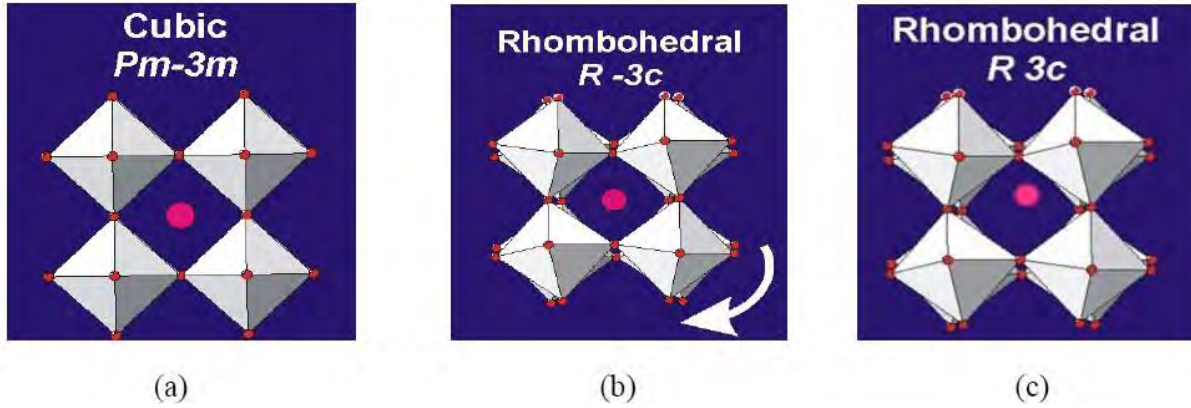
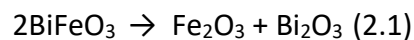


Figure 2-11: Schematic illustration of a structural transition process (a) ideal cubic structure $Pm-3m$ without tilting ($a_0a_0a_0$); (b) $R-3c$ structure tilted along three axes with the same angle ($a-a-a$); (c) Displacement of Bi ion towards $[111]$ direction based on $R-3c$. adapted from [91,93]

The lattice parameter and crystal structure of BiFeO_3 are dependent on the temperature. It was well documented that, except for the long Bi-Fe bond distance, the lattice parameter a , c , the volume of unit cell, the short bond distance of Bi-Fe as well as the bond angles gradually increase with increase in temperature. As a consequence of these variations, magnetism and polarization are reported to be gradually reduced, and structural phase transitions are also induced from the rhombohedrally distorted $R3c$ perovskite structure to an orthorhombic $Pnma$ structure and eventually to a cubic structure.

2.4.2.2. Phase diagram of BiFeO_3

The phase diagram of Fe_2O_3 and Bi_2O_3 is presented below in figure 2-12, unequal amount of Fe_2O_3 and Bi_2O_3 is seen to bring about impurity phases $\text{Bi}_{25}\text{FeO}_{39}$ (bismuth-rich) and Bi_2FeO_9 (bismuth-deficient). BiFeO_3 is usually prepared from equal parts of Bi_2O_3 and Fe_2O_3 , and under high temperatures it can decompose back into these starting materials, as shown in Equation 2.1.



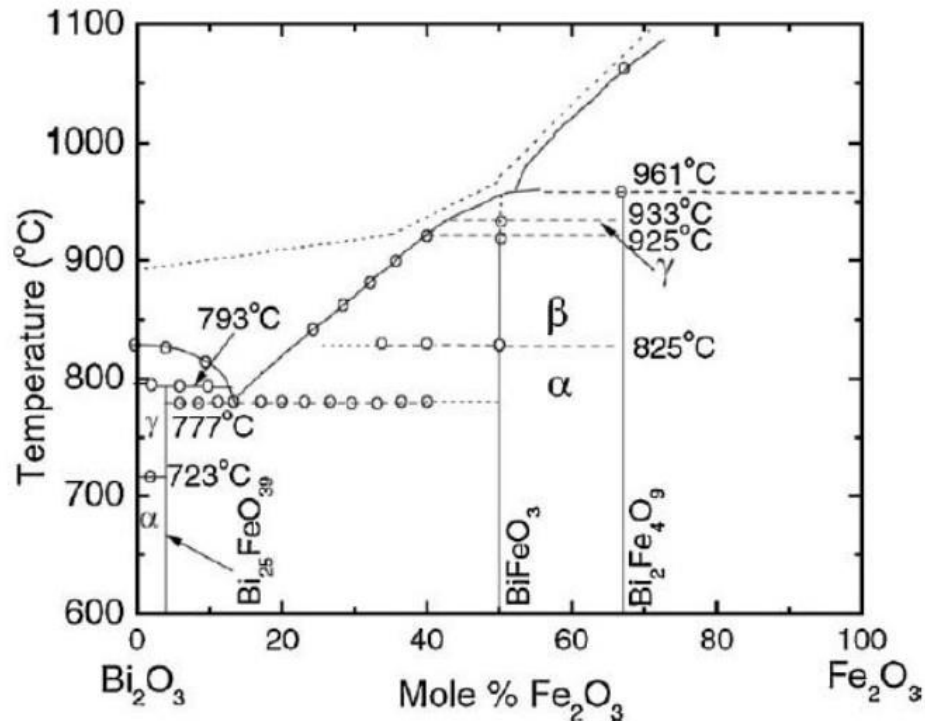


Figure 2-12: Phase Diagram of Fe₂O₃ and Bi₂O₃. (adapted from [94]).

At approximately 825°C there is a first-order transition to a high-temperature β phase that is accompanied by a sudden volume contraction [94,95]. The transition is also accompanied by a peak in the dielectric constant [95,96]; this has been taken as an indication of a ferroelectric–paraelectric transition, although dielectric peaks can also occur in ferroelectric–ferroelectric transitions, such as the orthorhombic–rhombohedral transition in the archetypal perovskite ferroelectric BaTiO₃ (which is also first order). Nevertheless, although there is disagreement about the exact symmetry of the β phase above 825°C, most reports agree that it is centrosymmetric [98–102], so it is probably a safe bet that the α – β transition at $T_C = 825^\circ\text{C}$ is indeed the ferroelectric–paraelectric transition.

Palai et al. [94] propose that the symmetry of the β phase is orthorhombic, although their data does not allow establishing the exact space group with certainty. Some authors have argued that the β phase may be tetragonal or pseudotetragonal [94, 97, 98], but that is impossible, since the domain structure rules out a tetragonal symmetry and the perovskite a, b, c lattice constants are each quite different [94,99]. It was also proposed that this phase may instead be monoclinic; [98,99] the measured monoclinic angle was nevertheless initially quoted as 90° within experimental error, [98] so that the β phase was in effect “metrically orthorhombic” (i.e., the angles may be 90° , but internal ion positions in each unit cell do not satisfy orthorhombic

constraints). More recently, however, Haumont et al. have quoted a monoclinic angle of 90.01° [99].

2.4.3. Electrical properties of BiFeO_3

The ferroelectric state arises from a large displacement of the Bi ions relative to the FeO_6 octahedra in BiFeO_3 as shown in figure 2-13. The ferroelectric polarization lies along the pseudocubic $\langle 111 \rangle$ leading to the formation of eight possible polarization variants, corresponding to four structural variants [104].

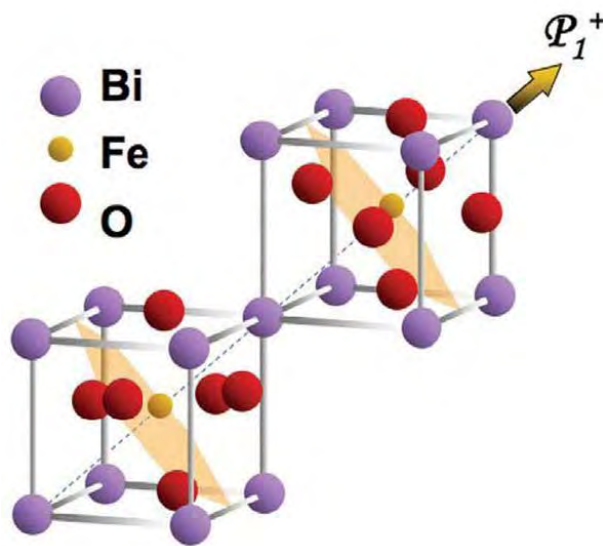


Figure 2-13: Schematic of crystal structure of BFO and ferroelectric polarization (arrow) along $[111]$ direction. (adapted from [104]).

Electrical characterization on bulk BiFeO_3 has been very difficult due to the low resistivity of samples. The controversy about whether it is ferroelectric or antiferroelectric was finally settled based on the hysteresis loop measured by Teague et al. [103]. They performed the experiment in liquid nitrogen, which lowered the charge carrier density and mobility, and in turn lowered the leakage current. The measured spontaneous polarization was $3.5 \mu\text{C}/\text{cm}^2$ along the $\langle 100 \rangle$ direction, which represents $6.1 \mu\text{C}/\text{cm}^2$ in the $\langle 111 \rangle$ direction. This value is much smaller than what would be expected for a ferroelectric material with such high Curie temperature and large distortion. The leakage problem, likely due to defects and non-stoichiometry, has been hampering more comprehensive studies about the bulk BiFeO_3 and has limited applications of this material. To overcome this problem, recent work has focused on reducing leakage current using proper dopants.

2.4.3.1. Piezoelectric Properties of BiFeO₃

Piezoresponse force microscopy measurements have been used to attest ferroelectric properties of the compounds. Trace the changes in the crystal structure parameters for the rhombohedral and orthorhombic phases, as well as to estimate the phase ratio across the transition from the rhombohedral to the orthorhombic structure. In addition, the rhombohedral phase is characterized by a lack of the inversion center and is piezoelectrically active, while the orthorhombic phase exhibits the antipolar displacement of the *A* and *B* ions in the perovskite lattice, thus nullifying the piezoelectric response. It is known that the polar displacement of bismuth ions along (001) direction of the rhombohedral cell gives the largest contribution to the piezoelectric response [155], whereas the calculated ion coordinates allow this displacement to be evaluated. Bismuth ferrite has several important properties, such as high remnant polarization (100 $\mu\text{C}/\text{cm}^2$ in a single crystal) and piezoelectricity, which makes it worth thorough investigation [156].

In addition, limited data exist on the piezoelectric properties and the relationship between strain and electric field, probably due to the problem of conductivity. The piezoelectric d_{33} coefficient and the electromechanical coupling coefficients k_t , k_p of BiFeO₃, sintered at 760 °C, as a function of poling field are shown in Figure 2-14 a and b. The d_{33} increases with poling field up to 40 pC/N at 100 kV/cm Figure 2-14 a.

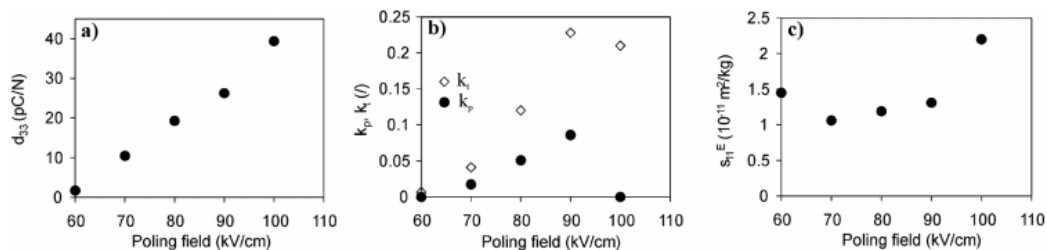


Figure 2-14: a) Piezoelectric d_{33} constant, b) electromechanical coupling coefficients k_p , k_t , and c) elastic compliance S_{11}^E of 760 °C-sintered BiFeO₃ as a function of poling field. (adapted from [158])

A similar trend is observed for k_p and k_t up to 90 kV/cm Figure 2-14 b. However, by increasing the poling field to 100 kV/cm, k_t decreases from 0.23 to 0.21 and k_p drops to almost zero. The drop in k_p coincides with the sudden increase in the elastic compliance S_{11}^E Figure 2-14 c. Inspection of the pellets using optical microscopy after these poling steps revealed cracking, which appeared after reaching a threshold field of 100 kV/cm. The onset of the cracking was also reflected in the splitting of the conductance at the radial mode resonance frequency. The cracks were typically observed along the radial direction of the disk-shaped samples, which could explain the more

pronounced decrease in k_p than in k_t and the softening of the material in the radial direction the increase in apparent S_{11}^E . These results open up further questions about the origin of cracking, an effect that prevents us from eventually obtaining better piezoelectric properties. [158]

- **Piezoelectric Materials**

Piezoelectrics are the class of dielectric materials which can be polarized, in addition to an electric field, also by application of a mechanical stress (figure 2-15). This unusual property exhibited by a few dielectric materials is called piezoelectricity, or, literally, pressure electricity. Piezoelectric materials can be divided into polar (which possess a net dipole moment) and non-polar piezoelectric materials (whose dipolar moments summed in different directions give a null total moment).

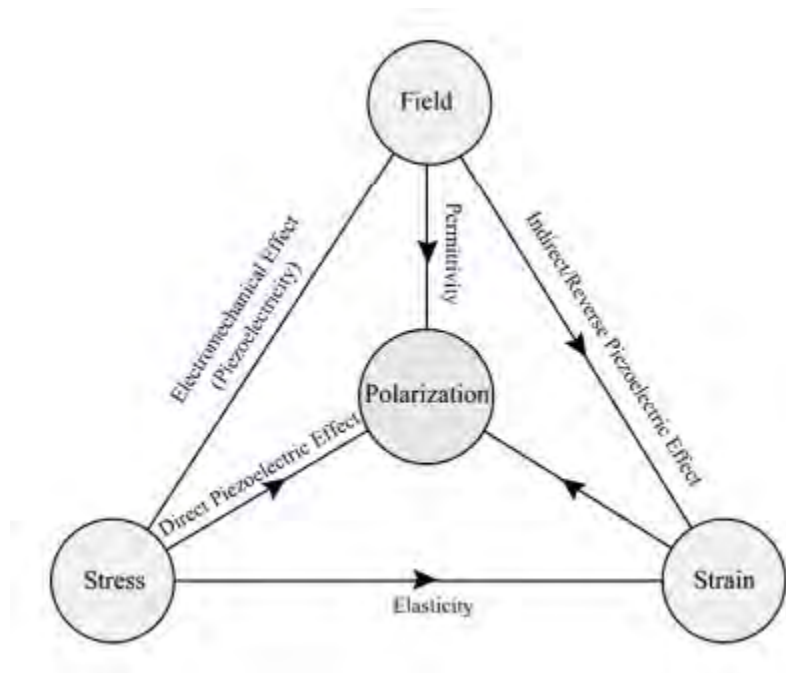


Figure 2-15: Piezoelectricity—An intermingling of electric and elastic phenomena. (Figure adapted from [192])

2.4.3.2. Pyroelectric Properties of BiFeO_3

The pyroelectric effect in bismuth ferrite single crystals is studied in the temperature range from 4.2 to 200 K (limited from above only by the high conductivity of the sample). A nonmonotonous character of the temperature dependence of the pyroelectric coefficient is revealed in the range 120–160 K: at $T = 140$ K, the pyroelectric coefficient reaches the maximum value equal to $1.2 \times$

10–4 C/(m² K). The crystallophysical analysis of the BiFeO₃ structure based on the structural data confirms that the octupole moment of the structure makes the main contribution to the spontaneous polarization. This circumstance leads to a small (in comparison with isostructural compounds) spontaneous polarization of bismuth ferrite and anomalous behavior of the pyroelectric coefficient caused by the contribution of local vibrations of strongly distorted TiO₆ octahedra. [157] The purpose of this study is to investigate the pyroelectric properties of bismuth ferrite single crystals in the range from 4.2 to 220 K, perform a crystallophysical analysis of its structural specific features, and establish the role of individual structure fragments in the formation of the polar state in BiFeO₃, which determine the anomalous behavior of the pyroelectric coefficient.

2.4.3.3. Dielectric constant of BiFeO₃

The radio frequency dielectric constant of BiFeO₃ at room temperature is $\epsilon_r = 30$. [105-108] It peaks at the rhombohedral–orthorhombic transition (825–840°C), possibly – though not necessarily – due to a ferroelectric–paraelectric transition. This dielectric constant is small compared with those of typical perovskite ferroelectrics such as BaTiO₃, (Ba, Sr)TiO₃ and Pb(Zr,Ti)O₃ (PZT). The mean refractive index, n , of BiFeO₃ is [109] ca. 2.62, so the optical frequency dielectric constant can be estimated as $\epsilon_r = n^2 = 6.86$. This is only an average value, however; dielectric constant at optical frequencies is very anisotropic.

Although 30 can be regarded as the intrinsic dielectric constant of this compound at radiofrequencies, the impedance measurements in parallel-plate capacitors often yield higher values: between 50 and 300 depending on sample morphology, orientation, and frequency range. This is because at the frequencies typically accessible by impedance analyzers (100 Hz to 1 MHz), domain-wall motion and space-charge contributions can be important and add to the measured permittivity. While the intrinsic value $\epsilon_r = 30$ may seem small for a ferroelectric, this value is not unreasonable. For one thing, the ferroelectric Curie temperature of BiFeO₃ is very high, meaning that at room temperature the ferroelectric polarization is already saturated and, thus, small electric fields will barely affect it (the dielectric constant is essentially a measure of polarizability).

Finally, and this is just a hypothesis, it may be that perovskite ferroelectrics in which the polarization comes from the A site (e.g., PbTiO₃ and BiFeO₃) have intrinsically lower dielectric constants than those where polarization comes from the B site (e.g., BaTiO₃). Experimentally this certainly seems to be the case, but at present we know of no satisfactory explanation for this fact, if indeed it is more than just a coincidence.

2.4.4. Magnetic properties of BiFeO₃

The local short-range magnetic ordering of BFO is G-type antiferromagnet: each Fe³⁺ spin is surrounded by six antiparallel spins on the nearest Fe neighbours (figure 2-16). The antiferromagnetic spin ordering is not homogeneous but is manifested as an incommensurate cycloid structure with a wavelength of ~64 nm along <110>, as can be seen in figure 2-17 [110]. The spin rotation plane can also be determined because the magnetic scattering amplitude depends on the component of magnetic moments perpendicular to the scattering vector [112]. The magnetic Néel temperature is about 643 K and the cycloid could be distorted at low temperatures [111].

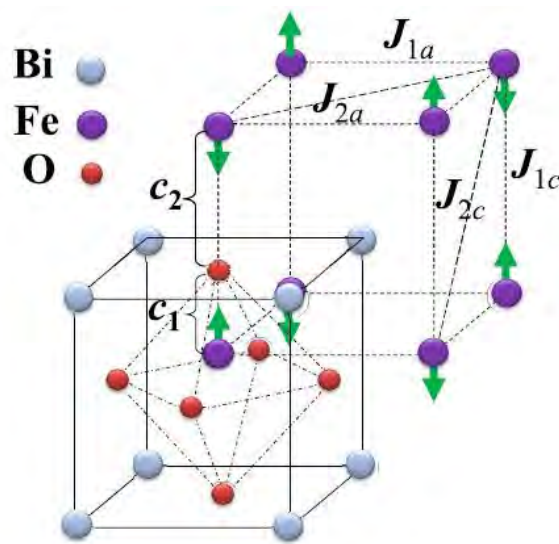


Figure 2-16: (Colour on-line) Schematic of tetragonal-like BiFeO₃ (BFO) with G-type antiferromagnetic ordering. (adapted from [110]).

Sc, Mn, Nb, Zr, Co and Ti ions substitute of Fe ions would increase the magnetization by changing the Fe valence state due to charge compensation and varying the Fe-O-Fe bond angle to increase the spin [114-118].

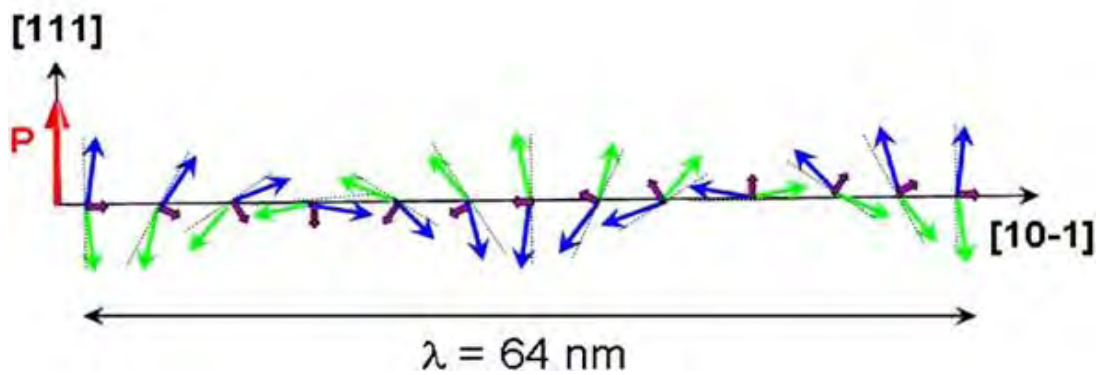


Figure 2-17: Schematics of the 64 nm antiferromagnetic circular cycloid. The canted antiferromagnetic spins (blue and green arrows) give rise to a net magnetic moment (purple arrows) that is specially averaged out to zero due to the cycloidal rotation. The spins are contained within the plane defined by the polarization vector [113].

For Bi-site substitution, Yb, La, Gd, Nd, Pb, Ca, Sr ions may also impact the magnetization of the BFO stem from the spatial homogenization of spin arrangement. The disturbed spin cycloid structure when La ions positions in Bi-site, the formation of partial Fe^{2+} due to the Bi ions volatilization or oxygen vacancies, varied canting angle of Fe-O-Fe bond due the distortion of FeO_6 octahedron caused by introducing La ions. The increased tensile strain changes the balance between the antiferromagnetic and ferromagnetic interactions [119-122]. As for the impact for dopants on the magnetic phase transition, there are very few report studies.

2.4.5. Optical Properties of BFO

2.4.5.1. Linear optical properties

The use of ferroelectric materials to convert light into electrical, mechanical, or chemical energy has generated broad interest in recent years for fundamental understanding reasons as well as application goals as they may be promising in photovoltaic, phototransduction, or photocatalytic devices.[159] Ferroelectrics exhibit an intrinsic spontaneous polarization that is at the heart of the aforementioned photoinduced phenomena. Among useful ferroelectrics for photoinduced applications, the so-called multiferroic BiFeO_3 (BFO) is the most promising candidate because of its relatively small band gap ($E_g \approx 2.6 - 2.8$ eV) in comparison to other classical ferroelectric oxides like BaTiO_3 , PbZrTiO_3 , or LiNbO_3 ($E_g > 3$ eV), allowing one to benefit from a wider part of the sunlight spectrum and its larger polarization value ($P \approx 100 \mu\text{C}/\text{cm}^2$), [160] ensuring a more efficient separation of the photogenerated charge carriers. There is increasing interest for photocatalytic and photolysis processes under visible light irradiation using this material. BFO

could potentially become an alternative to the widely investigated photocatalytic material TiO_2 which suffers from its large band gap, allowing one to use only $\sim 4\%$ of the solar spectrum. [161]

While the particle size is reduced and thus the surface reaction is increased, the photocatalytic activity of BFO was found to decrease in the investigated particle size range. Such unexpected behavior is explained by changes occurring in the optical response of BFO due to the existence of trapped defects and local distortions mainly altered at the skin layer. Decreasing the particle size affects the skin layer response, while the global properties (polarization, strain, band gap) are only weakly affected. The skin layer, being an inherent property of many other compounds, should be then taken into account for further investigation and use in future photocatalysis applications of other functional oxides with the ABO_3 perovskite structure like BiFeO_3 . [162]

2.4.5.2. Non-linear optical properties

BFO belongs to space group $R3c$ and the SHG tensor can be described with four nonzero independent components: d_{22} , d_{15} , d_{31} , and d_{33} . [163] Very few studies have focused on the BFO optical second harmonic properties but, recently, the relative values of the d_{ij} tensor coefficients were determined at 1064 nm from single crystal measurements. [164] In another study, [166] a careful determination of the absolute d_{ij} coefficients was performed at 1550 nm in the case of both rhombohedral and strain-induced tetragonal thin films. Experimental results were found to be consistent with ab initio calculations. [165,167] Interestingly, the magnitude of the coefficients of BFO appears higher than the values known for commonly used nonlinear optical materials, making BFO a very good candidate for frequency conversion applications. In addition, a significant result of this study is that a large increase of the NLO response was observed for tetragonal films in agreement with other reported enhanced properties in such films. [168]

The crystal symmetry of epitaxial BFO(111) films has been shown to be point group $3m$ using optical second harmonic generation (SHG) and diffraction techniques. [169] Optical SHG involves the conversion of light electric field E^ω at a frequency ω into an optical signal at a frequency 2ω by a nonlinear medium through the creation of a nonlinear polarization $P_i^{2\omega} \propto d_{ijk} E_j E_k$, where d_{ijk} represent the nonlinear optical coefficients.

2.4.5.3. Infrared properties

There are sundry studies on infrared properties of BFO. According Kamba et al. IR reflectivity spectra of BiFeO_3 plotted at selected temperatures between 20 and 950 K are shown in figure 2-18. [171] Thirteen reflection bands are well resolved at 20 K, which exactly agrees with the predicted number of IR active modes in the rhombohedral phase see Equation 2.2. Most of the

phonons gradually weaken on heating because the strengths of the newly activated modes in the rhombohedral phase are proportional to the square of the order parameter. [170] Simultaneously damping's of all modes increase on heating. Both these effects cause apparently only four IR reflection bands to be resolved at 950 K (see figure 2-18) although actually still 13 modes are needed for the reflectivity fit up to the highest temperature. One can expect that the strength of most modes will further gradually decrease on heating above 950 K and stepwise vanish at T_c 1120 K due to the first order phase transition into the cubic phase, where only three polar modes are permitted by symmetry.

$$\Gamma_{R3c} = 4A_1(z, x^2+y^2, z^2) + 5A_2(-) + 9E(x, y, x^2-y^2, xy, yz, zx) \dots \dots \dots (2.2)$$

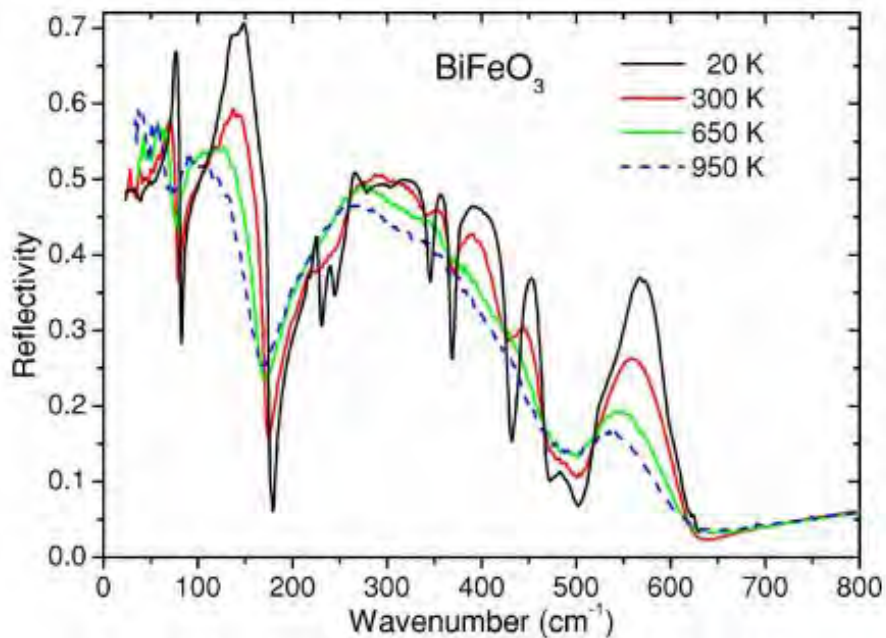


Figure 2-18: Color online Temperature dependence of the IR reflectivity spectra of BiFeO₃ ceramics. They note that the reflectivity value above 200 cm⁻¹ may be slightly reduced due to a small porosity of the ceramics and subsequent diffuse scattering of the IR beam. This can apparently enhance the phonon damping in the fit of our spectra, but the phonon frequencies are not substantially influenced. (Figure adapted from [171])

Another investigation of V. Goian on THz transmission and infrared (IR) reflectivity studies of Bi_{0.85}Nd_{0.15}FeO₃ lying close to AFE/FE boundary (figure 2-19).[173] The obtained complex ϵ^* spectra between 150 GHz and 20 THz are most likely not influenced by conductivity. The spectra allow to distinguish phonon contribution to ϵ^* , which exhibits a drop at T_c on cooling due to hardening of phonon frequencies on lowering temperature. Simultaneously, a strong dielectric relaxation was revealed below 1 THz in paraelectric phase. Its relaxation frequency and dielectric strength decreases on cooling and finally the relaxation disappears below 450 K. The origin of the relaxation and its relation to the strong piezo-response is discussed.

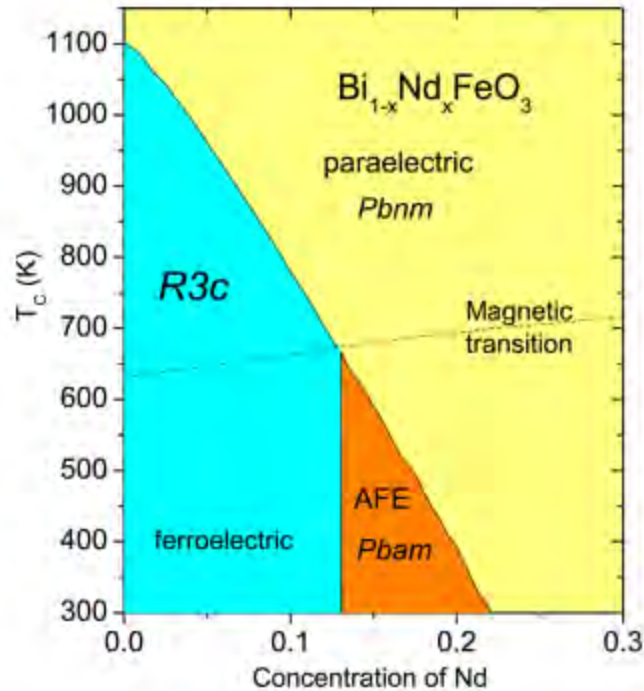


Figure 2-19: (Color online) Schematic structural and magnetic phase diagram of $\text{Bi}_{0.85}\text{Nd}_{0.15}\text{FeO}_3$ (plotted according to data in Ref. 172). Ferroelectric R3c phase has $Z=2$, paraelectric Pbnm phase $Z=4$, and antiferroelectric Pbam phase $Z=8$. Electron diffraction revealed even $Z=16$ and Pbnm structure in AFE phase. Néel temperature of G-type antiferromagnetic phase increases with Nd concentration (dashed line). (Figure adapted from [173])

The shape of low-temperature IR reflectivity spectra of BNFO reminds their spectra of pure BFO ceramics published several years ago,[173] although the crystal structures of both samples are different. One can see that only 13 polar modes are expected in the FE R3c structure of pure BFO, while 45 or even 109 IR active modes are allowed for AFE Pbam or possible Pbnm phase with $Z=8$ or $Z=16$ (possible structures are discussed in the Introduction). They have observed only 15 polar phonons in their low-temperature IR spectra (figure 2-20). The probable reason is that the newly activated phonons are weak and have frequencies close to the modes of the FE R3c structure, so that the modes become overlapped and cannot be resolved from the IR spectra. The possible splitting of the modes has influence on effectively much higher phonon damping observed in BNFO IR reflectivity spectra than in pure BFO. [173] The high-temperature IR reflectivity of BNFO differs from that of BFO mainly at low frequencies below 150 cm^{-1} due to the presence of THz dielectric relaxation. This causes disappearance of the reflectivity minimum near 90 cm^{-1} in BNFO above 700 K, while in BFO, the minimum is present up to the highest investigated temperature of 950 K. [173] Static permittivity of BFO slightly and linearly increases on heating due to small phonon softening with rising temperature, which is typical for improper-ferroelectric phase transition in BFO. [173]

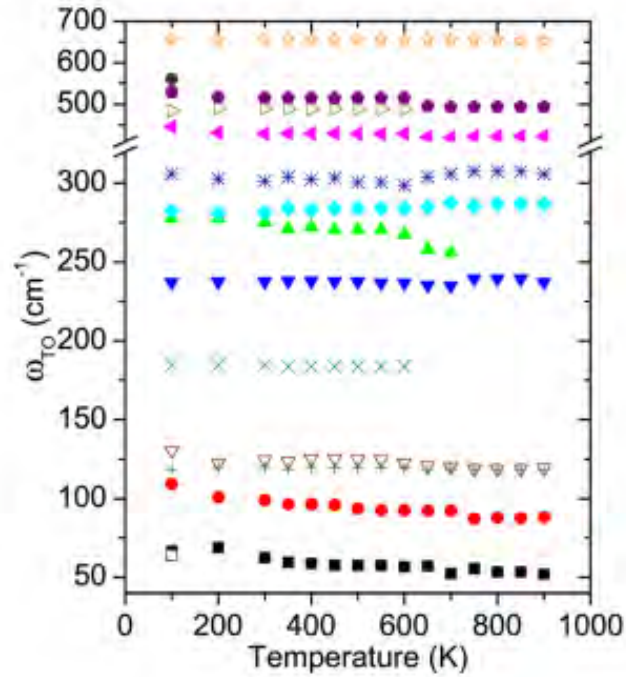


Figure 2-20: (Color online) Temperature dependence of transverse phonon frequencies obtained from the fits of THz and IR spectra. Appearance of several new phonons due to lowering of crystal symmetry below 600 K is seen. (Figure adapted from [173])

In BNFO, the phonon permittivity exhibits jump up at T_c and plateau above it. Nevertheless, contribution of dielectric relaxation grows on heating above T_c and, therefore, the static permittivity from the fit of THz and IR spectra also continuously increases.

2.4.6. Applications of BiFeO₃

Due to combining two or more primary ferroic orders out of ferroelectricity, ferromagnetism and ferroelasticity, multiferroic materials have potential applications in functional materials and fundamental physics, such as high-dense nonvolatile memory devices, spintronics, telecommunication and sensors.

2.4.6.1. Ferroelectric and Piezoelectric Devices

Being a room-temperature multiferroic, BiFeO₃ is an obvious candidate for applications. Interestingly, however, the first application that may reach the market might not use the multiferroic properties of BiFeO₃ at all. The remnant polarization of BiFeO₃ is very large, 100

μCcm^{-2} along the polar [111] direction. To put this into context, this is the biggest switchable polarization of any perovskite ferroelectric, and is roughly twice as big as the polarization of the most widely used material in ferroelectric memories, PZT. Moreover, unlike PZT, BiFeO_3 is a lead-free material, a bonus regarding health and safety. It is therefore not surprising that manufacturers of ferroelectric memories such as Fujitsu are considering BiFeO_3 as the potential active material in their next generation of ferroelectric memory devices.[123] For such an application to ever come into fruition, however, important obstacles must be removed, such as:

- i) the higher conductivity (and thus also dielectric losses) of BiFeO_3 relative to PZT,
- ii) its tendency to fatigue [124], and
- iii) the fact that it appears to thermally decompose at voltages quite close to the coercive voltage [125].

A second potential application unrelated to magnetoelectric properties is piezoelectricity. The piezoelectric coefficient of pure BiFeO_3 is actually quite small. However, its rhombohedral ground state means that mixing it with a tetragonal ferroelectric such as PbTiO_3 leads to a morphotropic phase boundary (MPB) at a composition of 30% mol PbTiO_3 [126].

This is important because MPBs are commonly thought to be the key behind the large piezoelectric coefficients of PZT and relaxors, [127] so the MPB of BiFeO_3 –PT might lead to equally large piezoelectric constants. A newer MPB with enhanced piezoelectric coefficients has been reported [128] for a solid solution of rhombohedral BiFeO_3 with orthorhombic SmFeO_3 ; it is likely that other solid solutions between BiFeO_3 and any of the other orthoferrites should also display similar MPBs. In this context, it is surprising that the widely studied solid solution between BiFeO_3 and LaFeO_3 does not appear to have yet been piezoelectrically characterized; perhaps this is due to its high conductivity.

2.4.6.2. Spintronics

The real drivers behind most of the applied research on BiFeO_3 are magnetoelectric and spintronic applications [129]. Chief among these would be memories that can be written using a voltage and read using a magnetic field. Using a voltage for writing has three advantages:

- i) this can be implemented in a solid-state circuit without mobile parts,
- ii) it has a low-energy requirement, and

- iii) the voltage requirements automatically scale down with thickness.

Reading the memory magnetically, on the other hand, has the advantage that it is a nondestructive readout process, unlike direct ferroelectric reading, which requires switching the polarization in order to read it. For such memories to actually work, the magnetic state therefore must be a) electrically switchable and b) magnetically readable.

The first condition is met by BiFeO_3 , because the easy plane of its antiferromagnetic domains is correlated with the polar direction, and rotating the ferroelectric polarization results in a rotation of the sub lattice magnetization [130-132], i.e., the magnetic state of the sample can be changed by a voltage. On the other hand, the second condition is not directly met, because antiferromagnetic (or, at best, weakly canted antiferromagnetic) domains cannot be easily read. An elegant solution to the problem of reading antiferromagnetic states consists in using the mechanism known as exchange bias. Crudely, exchange bias is the magnetic interaction between the spins at the uppermost layer of an antiferromagnet and a thin ferromagnetic layer attached to it. The exchange bias modifies the hysteresis loops of the ferromagnetic layer, either offsetting or widening them [133]. What is relevant here is that voltage-induced changes to the underlying antiferromagnetic domains will result in changes to the ferromagnetic hysteresis of the upper layer, which can then be read by conventional mechanisms. The implementation of this concept for Cr_2O_3 (which is magnetoelectric but not ferroelectric) was first done by Borisov et al. [134]. and the first investigation with an actual multiferroic (YMnO_3) was done by Laukhin et al.[135] The race to implement this idea using BiFeO_3 (which has the advantage over YMnO_3 that it works at room temperature) has been on for a while, and has been punctuated by several important milestones, such as the observation of exchange bias in thin ferromagnetic layers grown on BiFeO_3 [136,137], the correlation between exchange bias and ferroelectric domains [138], the observation that the antiferromagnetic domains can be switched by a voltage [132], and, most recently, the final proof of- concept that the exchange-biased ferromagnetic layer can indeed be switched by a voltage [139].

A second line of work uses BiFeO_3 as a barrier layer in spintronics. Sandwiching BiFeO_3 between two ferromagnetic metals results in tunneling magnetoresistance [129,138]. For this, the only requirement is that the BiFeO_3 layer be reasonably insulating down to tunneling thicknesses. However, an extra ingredient provided by BiFeO_3 is the fact that it also remains a robust and switchable ferroelectric down to a thickness of 2 nm [140], and thus it could in principle be used as an electrically switchable tunnel junction, whereby the ferroelectric state controls the magnetic state of the thin ferromagnetic electrodes, thus modifying the tunneling magnetoresistance. A similar concept using a ferromagnetic multiferroic (La-BMO) was indeed

demonstrated by Gajek et al. [141], who showed that the tunneling resistivity could be controlled both by electric and magnetic fields, giving rise to a four-state memory device. The voltage dependent barrier characteristics of BiFeO_3 have not yet been established.

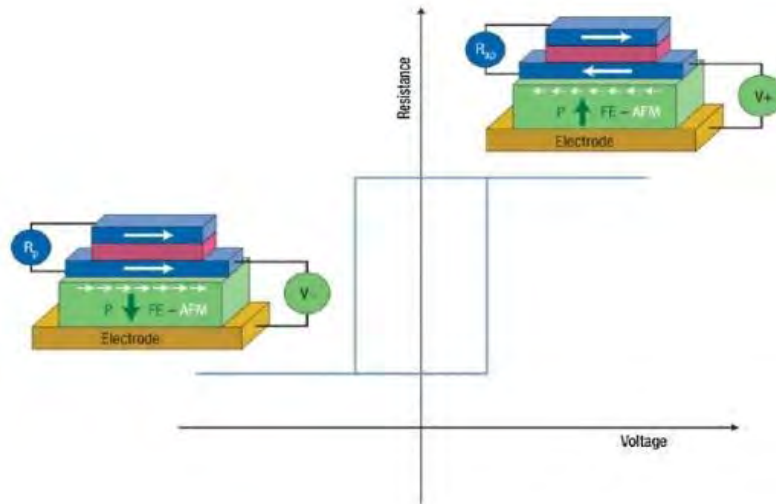


Figure 2-21: MERAM based on exchange-bias coupling between a multiferroic that is ferroelectric and antiferromagnetic (FE-AFM, green layer), and a thin ferromagnetic electrode (blue). A tunneling barrier layer between the two top ferromagnetic layers provides the two resistive states. Interestingly, BiFeO_3 could act not only as the magnetoelectric active layer, but also as the tunneling barrier. Adapted from [142]

The above developments show that, at least in principle, it is now possible to develop an MERAM (Magnetoelectric Random Access Memory) based on BiFeO_3 . A schematic of such a device has been proposed by Bibes and Barthelemy [142], and is reproduced in figure 2-21.

Chapter 3: Experimental and Process Descriptions

This chapter will be outlined the process descriptions and experimental details used during the synthesis and characterization of bismuth ferrite ceramics. A detailed account of all the synthesis and characterization techniques used will be given.

3.1. Introduction

For advanced research, it is very important to use high purity raw materials. At the same time, it is vital to ensure that during sample preparation no impurity gets incorporated into the ceramic powders. Moreover, accurate weight calculation and measurement are also important to guarantee single phase formation. After sample preparation, sample characterization and property measurement were carried out and finally a relationship between structure and property is established. During all experiments starting from sample preparation to property measurement, all parameters should be maintained for getting good consistent results.

3.2. Processing of bismuth ferrite-based ceramics

In case of ceramic bodies, properties of the final parts largely depend on the processing route. In the present days bismuth ferrite powders are being processed through many routes. Of them, starting from solid state reaction to wet chemical methods (sol-gel, co-precipitation, hydrothermal, microwave-hydrothermal, sonochemical and auto-combustion methods) [30] are prominent to obtain ultra-pure powders. Each production route must take the stoichiometry of the final powder into account which relies on the process used and the quality of the raw materials as well as on the applications. But till now the conventional route is the most popular method from the industrial point of view. The conventional solid-state synthesis route, also known as the ceramic method, refers to a procedure of heating two or more non-volatile solid-state materials that can react with one another forming a new compound.

Typically, the high temperature treatment (500°C-2000°C) is required during the process, which provides the energy condition that enables the ions to leave their original sites and diffuse to different sites. The solid-state reaction is quite slow but the reaction can speed up considerably if the temperature is increased. However, due to the decomposition or melting of materials, extremely high temperature is not favored. In principal, the optimal temperature is defined by a rule of thumb that two-thirds of the melting temperature of the compound always gives best reaction time.

3.2.1. Ball Milling

Before ball milling the raw materials like Bi_2O_3 and Fe_2O_3 powders are weighed according to the stoichiometry. The weighed powders are thoroughly mixed in a ball mill or in an attrition mill. Milling is carried out to fulfil twofold purposes. One is to reduce the particle size and another is to mix the raw materials homogeneously. Both finer particle and homogeneity of raw powders eases the diffusion controlled solid state reactions.

The schematic representation of a ball mill is illustrated in figure 3-1. In the present days, powders are only mixed properly in a laboratory type pot mill. Size reduction of the powders are not now the primary objective of ball milling as the nano sized powders are now available for laboratory type research, rather the objective of ball milling is to homogenize the mixture. The balls should be of the same material as powders so that wear of balls does not contaminate the powder mix. For example, in the past days hardened steel balls were used in a porcelain pot. But iron has a very detrimental effect on the dielectric properties of barium titanate based materials. In the present days high density polyethylene (HDPE) pots are used as the container and Y_2O_3 stabilized ZrO_2 balls are used to mill the powders.

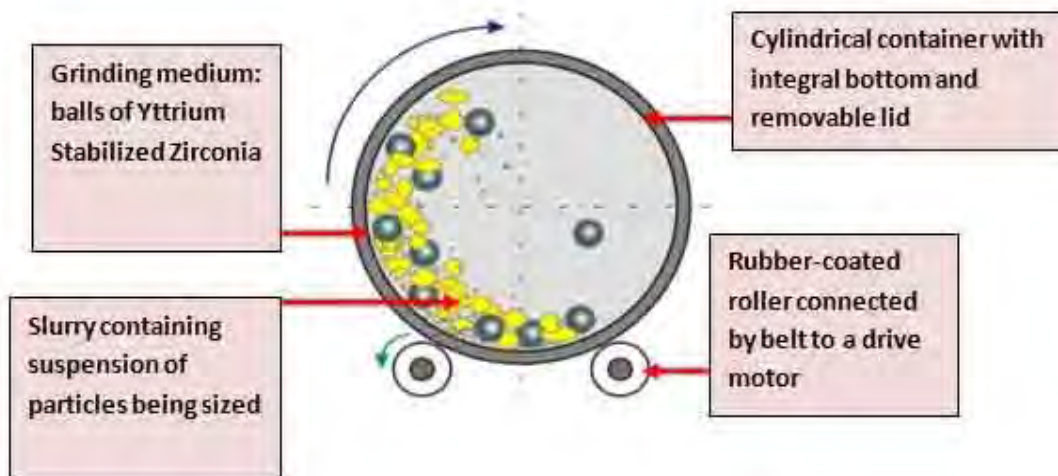


Figure 3-1: Schematic representation of ball milling. [google image]

In the wet milling process, milling medium is another important consideration for two reasons. It must not react with the balls, the container or the powder. Secondly, it must avoid decrease of colloidal stability. After milling the suspension is dried to evaporate the milling medium.

3.2.2. Drying

Drying denotes the separation of volatile liquids from solid materials by vaporizing the liquid and removing the vapor. The liquid that is to be removed is usually water, but it could also be a solvent such as alcohol or acetone, or a mixture of such solvents. The vaporization of liquids requires the supply of heat. Accordingly, drying can be considered a thermal separation process.

The product that is to be dried is denoted as the moist solid, or simply as the solid. The substance that carries the necessary heat is called the drying agent. This substance could be air, an inert gas, or superheated steam. Heat could also be supplied by radiation, by hot surfaces, or by microwaves. In this research I used hot plate for drying. The solution of BFO in IPA (Isopropyl Alcohol) is needed drying to get solid powder from the solvent. The drying is done at 80-90°C for 1 hour.

The mass flux of the vapor leaving the surface of the solid per unit time is called the drying rate, and is denoted by the symbol \dot{m} (in $\text{kg m}^{-2} \text{s}^{-1}$). The drying rate is usually determined by measuring the change of moisture content with time dX/dt . It follows that

$$\dot{m} = - \frac{M_s}{A} \frac{dX}{dt}$$

M_s is the mass of the dry solid, and A is the portion of its surface area that is in contact with the drying agent. The drying rate \dot{m} depends on the conditions of drying and on the moisture content X . The drying conditions are specified by factors such as the air pressure, temperature, and humidity, the radiator temperature, the temperature of a heating surface, or the strength of the microwaves. The relationship of the drying rate \dot{m} and the moisture content X under constant drying conditions – this is $\dot{m}(X)$ – is called the drying rate curve.

3.2.3. Sintering

The densification of a particulate ceramic compact is technically referred to as sintering. Sintering is essentially the removal of the pores between the starting particles (accompanied by shrinkage of the component), combined with growth together and strong bonding between adjacent particles.

The following criteria must be met before sintering can occur:

1. A mechanism for material transport must be present.
2. A source of energy to activate and sustain this material transport must be present.

The primary mechanisms for transport are diffusion and viscous flow. Heat is the primary source of energy, in conjunction with energy gradients due to particle-particle contact and surface tension.

All properties of ceramic depend on the sintered body which is the direct result of the sintering parameter such as sintering temperature, hold time, atmosphere, thermal profile, etc. There are many sintering methods used but this discussion would be limited to Spark Plasma Sintering.

Heat causes the powder particles to develop intergranular bonds by surface diffusion and other physical driving force. The typical green density of ceramic body at the start is about 60% of theoretical density. Strength starts to develop gradually as more and more particles bond.

At about ~ 80% to 85% density the pores are still open and the ceramic has a typical “chalky” appearance. The dielectric constant is usually low and the T_c is not pronounced strongly. The pores of a ceramic are generally closed above ~90% of theoretical density. Additional heat work causes greater densification as trapped gasses diffuse out along grain boundaries. At densities below 90% of theoretical density the presence of open pores would cause the dielectric loss and undoubtedly inferior dielectric properties.

Setting of sintering temperature is not that straight forward. Low temperature sintering results in ceramic of poor density. On the other hand, too high temperature and long hold time may cause open structure with low density. Also, at high temperatures grain growth is accelerated resulting in low dielectric properties. The sintering temperature and time should be optimum for proper densification to occur without abnormal grain growth. This is usually done by trial and error method depending on various process parameters.

3.2.3.1. Mechanism of sintering

There are three types of sintering with different densification mechanisms:

1. Solid phase sintering: All components remain solid throughout the sintering. The densification is carried out by a change in shape of the grains. Mass transport occurs by volume and grain boundary diffusion.

2. Liquid phase sintering: Formation of a viscous liquid (usually a eutectic with a low melting point) that fills the pore spaces of the initial green body (e.g. porcelain). Densification occurs mainly by dissolution and reprecipitation of the solid which allows a rapid mass transport.

3. Reactive sintering: Two or more constituents react during sintering. The densification is carried out by the formation of a new compound.

From a technical perspective, the densification during sintering can be improved by applying an external force. The most common techniques are the application of a uni-axial pressure (HP = hot pressing) or isostatic pressing (HIP = hot isostatic pressing). Additionally, there is a variety of techniques to influence the microstructural characteristics of the final piece by changing the heating and cooling rates. An example is **spark plasma sintering (SPS)** where very high heating and cooling rates are achieved with the help of a pulsed electric field which leads to a high density in a relatively short period of time (5-10 minutes) while keeping a relatively small grain size. [143]

3.2.3.2. Sintering of Bismuth Ferrite

BiFeO_3 ferrite ceramics were synthesized by spark plasma sintering (SPS) and conventional solid-state synthesis in conjunction with high-energy ball milling.

a. Spark plasma sintering

Spark plasma sintering (SPS) is a novel sintering technique and it consolidates powders into bulk materials by utilizing pulsed current simultaneously with in-situ pressure [144,145]. It is a new technique which takes only a few minutes to complete a sintering process compared to conventional sintering which may take hours or even days for the same. The basic configuration of SPS machine is depicted in Figure 3-2. It consists of a uniaxial pressure device, in which water-cooled graphite punches serve also electrodes, a water-cooled reaction chamber that can be evacuate or back field with a gas, a pulsed DC generator and a z-axis position dilatometer and a temperature regulation system.

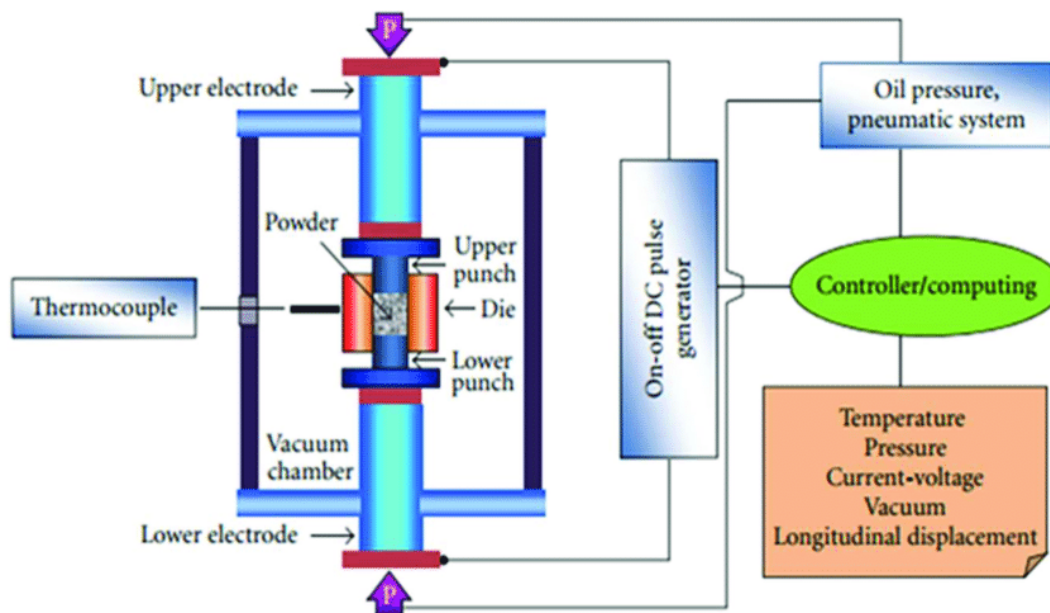


Figure 3-2: Schematic of a spark plasma sintering machine. Adapted from [google image]

This high sintering rate is possible in SPS since high heating rates can be easily attained due to internal heating of the sample as opposed to external heating seen in case of conventional sintering. Also, sintering time is reduced in SPS due to small holding time at sintering temperature, usually 5 to 10 minutes while in conventional sintering it may extend to hours. The heating rates normally attained in conventional furnaces are 5 to 8°C/min which can go maximum upto 10°C/min. So, to attain a temperature of above 1000°C we usually require 2 to 4 hours or more whereas in SPS heating rates exceeding 300°C/min are easily obtained hence a temperature of 1200°C can be obtained in only 4 minutes. Simultaneous application of temperature and pressure leads to high densification and hence a dense compact at sintering temperatures lower by 200 to 250°C than in conventional sintering is easily obtained.

In SPS, since no coarsening and grain growth were allowed to occur, high relative densities were reached in very short time and nano sized powders can be sintered without considerable grain growth which is not possible in conventional sintering process. Hence, nano-structured ceramics or nano-composites can be easily prepared by SPS having more densification and fewer defects. These nano-structured composites exhibit excellent mechanical properties like high strength, high hardness etc.

For conventional sintering usually, a green compact need to be prepared externally using a suitable die and hydraulic machine for applying the necessary pressure. After this the green compact is sintered in a furnace. In SPS the powder is directly fed into the graphite dies and the die is enclosed with suitable punches. This entire assembly is directly put into the SPS chamber and spacers are used if necessary. The chamber is now closed and the atmosphere (vacuum, Argon etc) in which sintering is to be carried out is applied in the chamber. The program is set into the control unit and sintering is carried out. Atmosphere control is much easier in SPS than in conventional furnaces. All types of materials, even those difficult-to-densify can be easily sintered in SPS. Due to advantage of high heating rate and less holding time, SPS can restrict the unwanted sintering reactions in highly reactive systems as opposed to conventional sintering and hence formation of undesirable product phases can be avoided.

The apparent willingness to embrace novel densification mechanisms primarily arises from a belief that lower processing temperatures are required than in conventional processing. Although there is generally an acknowledgement that the temperature seen by the sample is higher than the measured temperature, the extent of this temperature difference and its sensitivity to experimental conditions appear not to be understood. Furthermore, once the temperature seen by the sample is established, a meaningful comparison with conventional processing temperatures can only be made if SPS is compared with other pressure assisted densification techniques (such as hot pressing or hot isostatic pressing) rather than with pressureless sintering.

b. Process of the SPS Machine

Take known quantity of dried and milled powder sample in a cylindrical die, lined with graphite sheet which facilitates easy removal of the sintered compact. Switch on the Chiller – compressor and the machine. Place the die containing the powder sample inside the SPS chamber. Then, set the specific pattern (time-temperature data) needed for the experiment to follow and thereafter, maintain the required atmospheres as Vacuum, Argon etc inside the chamber. Set the power to maximum in Auto mode and the required load to be applied on the die. Also, set the z-axis position to zero. **ON** the timer and finally press **SINTER** to start the sintering process. For measuring the temperature in SPS two types of instruments are used: thermocouple for sintering temperatures below 1000°C and pyrometer for sintering temperatures in excess of 1000°C. High DC Pulse is passed between graphite electrodes and axial pressure is simultaneously applied from the beginning of the sintering cycle. The sample is heated by the Joule-heating and the sparking among the particles of sintered material leads to the faster heat and mass transfer instantaneously. After the sintering, the power is turned off and the sample is allowed to cool.

c. SPS parameter effects

The sintering temperature is of great importance as sintering is a thermally activated process. It has been shown great impact on the densification, sintering rates, grain growth, plastic deformation and solid-state reactions during the sintering ceramics [146,147]. It is known to us that sintering occurs in which the onset temperature for specific materials. Sintering at temperatures beneath this temperature generates it very difficult to create a dense ceramic. Again, it has been shown that length of the holding time above the onset temperature effects the ceramic densification and that grain growth is substantially higher above a specific elevated temperature [146,147].

SPS sintering temperature has a significant effect on the structural properties of bismuth ferrite ceramic. Higher sintering temperature is responsible for formation of impurity phase ($\text{Bi}_2\text{Fe}_4\text{O}_9$). The low temperature one is a thermal activated process, which can be removed by vacuum annealing. The dielectric relaxation at high temperatures is attributed to the short-range motion of oxygen vacancies and cannot be removed by vacuum annealing [153].

During the sintering process the application of pressure has also been shown to have effect on the ceramic. The reduction of pore density throughout the sample has been found with the increased pressure. Thus, it enhances diffusion, this entails that the application of the mechanical pressure during sintering boosts the densification of the ceramic[146,147].

d. Thermal distribution during the SPS process

During the sintering process the temperature distribution is dependent on the number of different parameters:

- ✚ The size and the shape of the die and punches used and their associated thermal and electrical properties.
- ✚ The pressure used during the sintering process along with the heating and cooling rate.
- ✚ The thermal and electrical properties and dimensions of the samples used

The composition of the environment inside the SPS chamber affects the material's diffusivity during sintering. For this reason, the processes that normally occur during a sintering cycle, such as phase constitution, densification, and grain growth, are strongly affected by the sintering atmosphere [148].

Typical materials developed by the SPS technique are refractory metals and intermetallics, oxide and non-oxide ceramics. The particles constituting the powders before consolidation tend to

decrease their surface energy by desorption of chemical species, once introduced inside the SPS chamber. The released gas, water, or organic compounds in the atmosphere modify the thermodynamic driving force to surface reduction and sintering.

3.3. Raw materials

The constituent materials are:

a) Bismuth Oxide (Bi₂O₃) nano powder

Size: 200 nm

Manufacturer: INFRAMAT (USA)

Purity: 99.99%

b) Iron oxide (Fe₂O₃) powder

Size: <50nm

Manufacturer: INFRAMAT (USA)

Purity: 99.99%

Table 3-1: Information of raw materials

Elements/Oxides	Atomic Number	Atomic/Molecular Weight	Density g/cm ³
Bismuth (Bi)	81	208.98	9.78
Iron (Fe)	26	55.85	7.86
Bismuth oxide (Bi₂O₃)	-	465.96	8.9
Iron oxide (Fe₂O₃)	-	159.69	5.24

3.4. Sample Preparation

- 1) Powders will be weighted under fume hood prior to further processing: ball milling, drying and sieving.
- 2) 2-propanol is used as solvents for ball milling. Around 100ml of alcohol is added to 5 g of mixed powders and ball milled for 18h. After ball milling alcohol will be evaporated under fume hood.
- 3) The prepared powders are calcined at 800C for 2h. Then powders are mixed, ball milled again in IPA for 8h. After drying and sieving finally the powders are prepared for sintering and those are used in CEMS Lab for Spark Plasma Sintering (SPS).

3.4.1. Weight Measurement

As stated previously the basic raw materials used are powders of Bi_2O_3 and Fe_2O_3 . These powders were taken according to the target composition of the batch to be prepared. Powders are weighted according to the following:

Bi_2O_3 3.724 & Fe_2O_3 1.227 g (for 5gm precursor)

Bi_2O_3 5.960 & Fe_2O_3 2.040 g (for 8gm precursor)

3.4.2. Milling

The main purpose of ball milling is mixing and homogenization of the samples. Appreciable size reduction does not occur nor is it necessary. The powders of different compositions were taken into different high-density polyethylene (HDPE) pots serving as the milling chamber. Y_2O_3 stabilized ZrO_2 balls, together with Isopropyl Alcohol, were used as the grinding medium. After loading the bottles with powders, balls, and Isopropyl Alcohol the lid was tightly sealed with tape and the bottles were placed in the milling machine. The machine rotates the bottles at an rpm of 50 along a horizontal axis. The grinding action of the balls mixes the powders thoroughly. All the compositions were milled for 18 hours. It must be noted that before adding the powders in the milling bottles, the bottles and the zirconia balls were cleaned, at first by hand, and then in an ultrasonic bath to rid them of any trace of impurity or unwanted substance.



Figure 3-3: Milling pot with zirconia balls and ball mill setup. Adapted from [SPS lab UL]

3.4.3. Extraction and Drying

After milling, the mixture, now in suspension in IPA, is carefully extracted into a glass beaker (which was ultrasonically cleaned). The beaker is covered with a perforated aluminum foil and kept in a drier at around 80-90°C. It is important to keep the mixtures in the drier for a sufficiently long time, so that a completely dry powder mixture is obtained. At this point the powders are in the form of a friable cake.

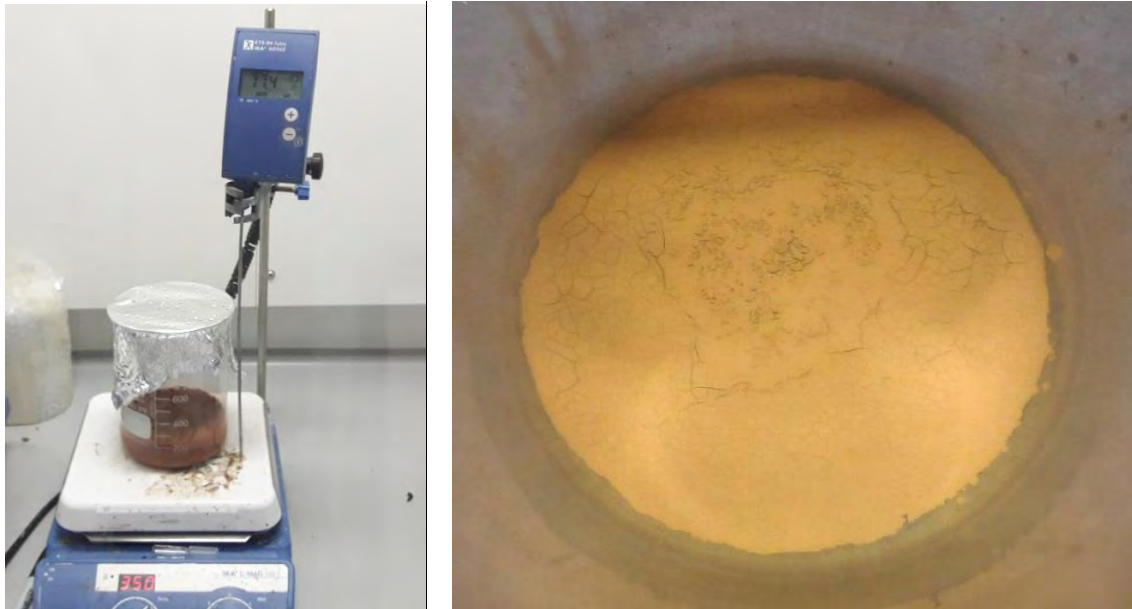


Figure 3-4: Fume hood and Hot plate used for Drying and powders after drying. Adapted from [CS lab UL]

3.4.4. Sieve Analysis

Particle size is one of the most important properties of ceramic. One gram of powdered material can have billions of particles with a surface area of many square meters. A knowledge of not only the average size but how the sizes are distributed, can be very valuable.

A simplistic definition of sieving is the separation of fine material from coarse material by means of a meshed or perforated vessel. Professor Terence Allen characterizes sieving as "The aperture of a sieve may be regarded as a series of gauges which reject or pass particles as they are presented to the aperture." [149] This theory was actually in practice during the early Egyptian era as grains were sized with 'sieves' of woven reeds and grasses. The level of sophistication increased with the rise of the industrial revolution and the need for more sophisticated methods for classifying material by their particle size. As requirements for sized material rose, technology

in producing uniform sieving media increased. Woven wire cloth was introduced as an alternative, providing greater accuracy and durability. At present, this woven cloth is available in a range of sizes from 125 mm (5") openings to 20 micrometer openings. All mesh sizes are covered by both national and international standards.

The need for particle size analysis in the finer size ranges (i.e. 38 micrometers and less) prompted the development of the electrodeposited sieve. These sieves, sometimes called electroformed or micromesh, are currently being produced with openings as fine as 3 micrometers. The mesh openings are extremely uniform in both size and shape and maintain exacting tolerances.

In this work several mesh sizes for sequential sieving using 425, 125, 90, and 53 micrometer respectively were used.



Figure 3-5: Laboratory Test sieve with different mesh size. Adapted from [CS lab UL]

3.4.5. Calcination

The calcining process is used to remove some or all unwanted volatiles from a material (e.g. H₂O, CO₂, SO₂) and/or to convert a material into a more stable, durable or harder state. Varying temperatures are employed to calcine various materials, depending on the decomposition temperature of the volatiles being burned out and the degree of sintering desired in the product.

Calcination temperature of BFO varies with used method of preparation. For solid state synthesis calcination temperature is around 800 °C and for another common route for BFO preparation that is sol-gel. Here calcination temperature is somewhat lower 300-550°C [150,151]. Moreover, for hydrothermal route synthesis temperature is lower than the other route. According to Zhou, Min, et al. synthesis temperature was 180-200°C [152].

In this present work, to form bismuth ferrite precursor powders was calcined at 800 degrees Celsius for 2 hours at a heating rate 5 °C/min. The cooling rate was same as heating rate.



Figure 3-6: Furnace used for calcination and powders after calcination. Adapted from [CS lab UL]

3.4.6. Sintering of Bismuth Ferrite Ceramics

The Bismuth ferrite powders were sintered into ceramics using spark plasma sintering furnace (Dr. Sinter, SPS-515S, SPS Syntex Inc., Kawasaki, Japan). BFO powders was loaded into a graphite die (10mm in diameter) and punches inserted through the top and bottom of the die, as shown below in figure 3-7.

A uniaxial pressure of 50 MPa (3.9kN) was initially to the punches and a sintering vacuum of 6×10^{-3} Pa utilized throughout the process. During the sintering process a constant uniaxial force of 3.9 kN was applied to the powder.

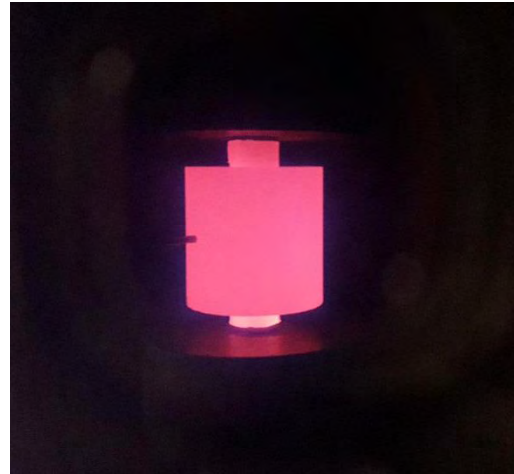
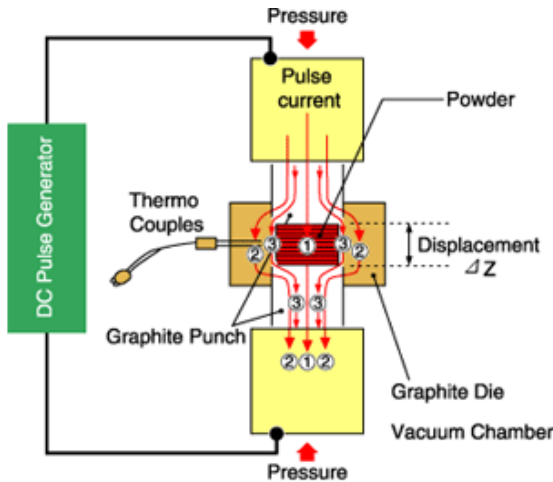


Figure 3-7: Schematic of SPS Machine and Powder sample within graphite die at 750°C during spark plasma sintering.

The sintering programme consisted of a 12:2 pulsed ratio of electrical discharge of up to 5 V and 500 V. The high current applied across the graphite die cause joule heating to heat the sample. The amount of current passing through the sample controls the heating rate, the holding temperature and cooling rate, as figure 3-8.

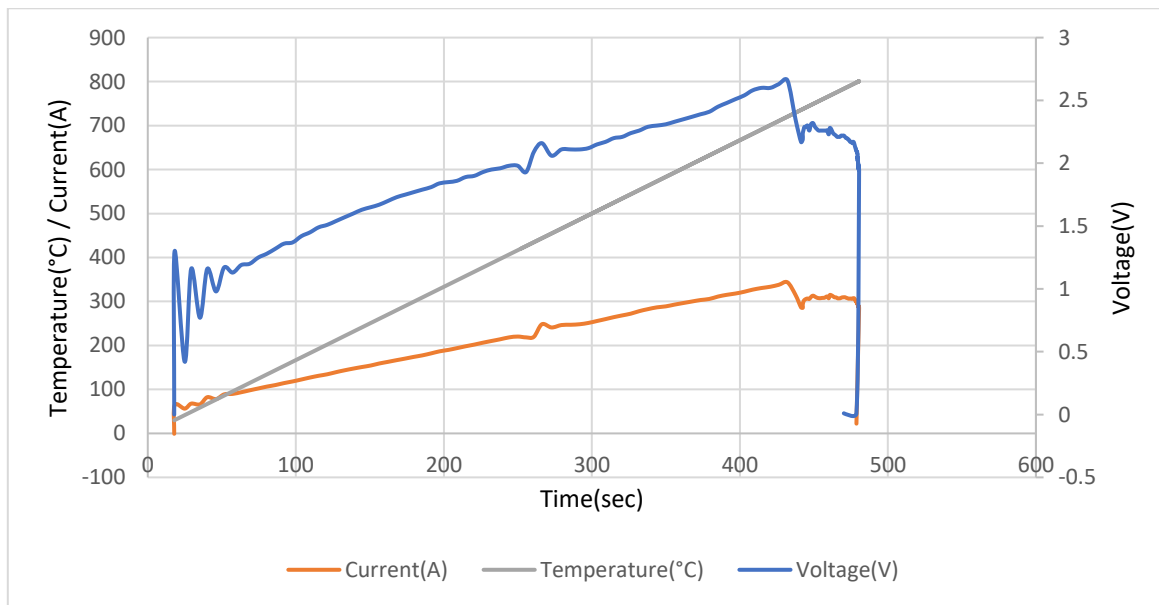


Figure 3-8: Graph showing the effect of voltage and current on the temperature of the sample during spark plasma sintering.

The sintering temperature was varied between 625 to 825 °C with a constant heating rate of 100 °C/min. Once the desired temperature was reached a holding time of 5 min was applied,

after this time the electric current was reduced and the temperature was allowed to gradually decrease to 550 °C. At a temperature of 550 °C the current passing through the sample was turned off and the sample was allowed to cool to room temperature using built in water coolant system. The pressure pressing down on the sample was reduced at 580 to 550 °C during sintered at 625°C. Similarly, pressure reduction starts at 650 to 590 °C, 650 to 560 °C, 700 to 620 °C and 800 to 690 °C during sintering at 700, 750, 800 and 825 °C respectively.

3.4.7. Polishing

Polishing is very important as it is inevitable for obtaining better surface finish. Polish assists to remove unwanted material (like carbon paper) from the surface of the samples. For optical microscopy examination better surface finish is necessary in that case polishing acts as a prerequisite here. In this work I used 3 different grade of paper that are 800, 1000 and 1200 respectively. The machine used for polishing was PM01023 (Figure 3-9). The rpm of the rotating wheel was kept fixed for each sample that was 200. To obtain better surface finish I did polish more time at 1200 grade paper at least 30 min for each sample.



Figure 3-9: Polishing Machine(PM-01023). Adapted from[CS lab UL]

3.5. Poling of Ceramics

Poling or polarizing is to be used after the BFO ceramics have been prepared through spark plasma sintering. It is carried out with the aim of producing net polarization amongst the crystallographic domains within the ceramic and to induce piezoelectricity within the material. When sufficiently strong electric field is applied across the ceramic it can genesis a reorientation of spontaneously polarized units into a more isotropic alignment along the field lines. As very high voltages (up to 5000V) can be used during the polarizing process it was necessary to design and build an insulated container to house the polarizing apparatus will be presented in the following section.

3.5.1. Poling Apparatus

The polarizing unit consists of an external high voltage power supply (PS350 High voltage power supply, Ps 50 to 5000 Volts, 5mA, Stanford research systems), a modified desiccator box with locking mechanism, an internally mounted hot plate and the polarizing apparatus (Figure 3-10).

To assure the safety of the operator and others in the vicinity of the polarizing unit the design and construction of the modified desiccator box was an essential part. The design brief required that no high voltage was pass through the polarizing apparatus while the detector door was open. To complete this brief a safety interlock switch was attached to the side of the desiccator box and control feedback was created to control the current going to the high voltage supply.

When the interlock key on the door is inserted into the door interlock it is held in position with a locking force of 2000 N, the insertion of the interlock key also closes the circuit to allow the high voltage power unit to power up. Without the key being inserted into the interlock no current will flow through the system.

To open the door the high voltage power unit must be fully turned off. This in turn kills power to the interlock switch and switches the locking motor to off position. The door of the desiccator cannot be opened without firstly turning the power off to the high voltage supply.

A keyed emergency stop button is attached to the side of the control unit. This button may be pressed if the need for immediate shut down is required. By pressing the emergency stop button all power is stopped from going into the high voltage supply, which in turn powers down the door interlock switch allowing the door to be opened. To re-start the system, after the emergency stop has been pressed, the key must be turned to the on position. If the key is removed before turning it to the on position the system will remain shut down and no current will flow through it.

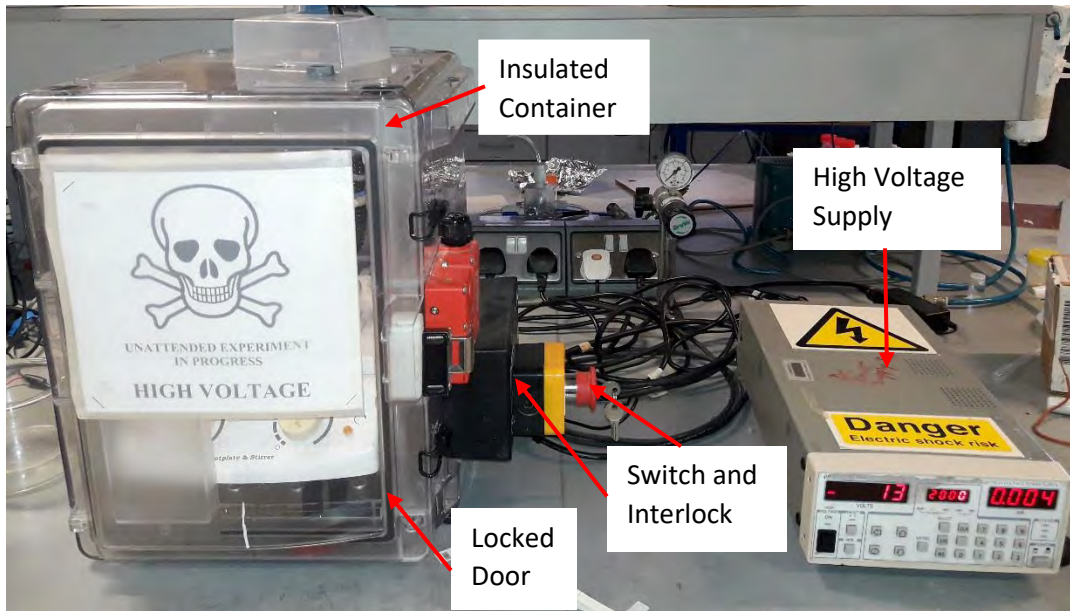


Figure 3-10: Operational set up during polarization of ceramics. Adapted from[CS lab UL]

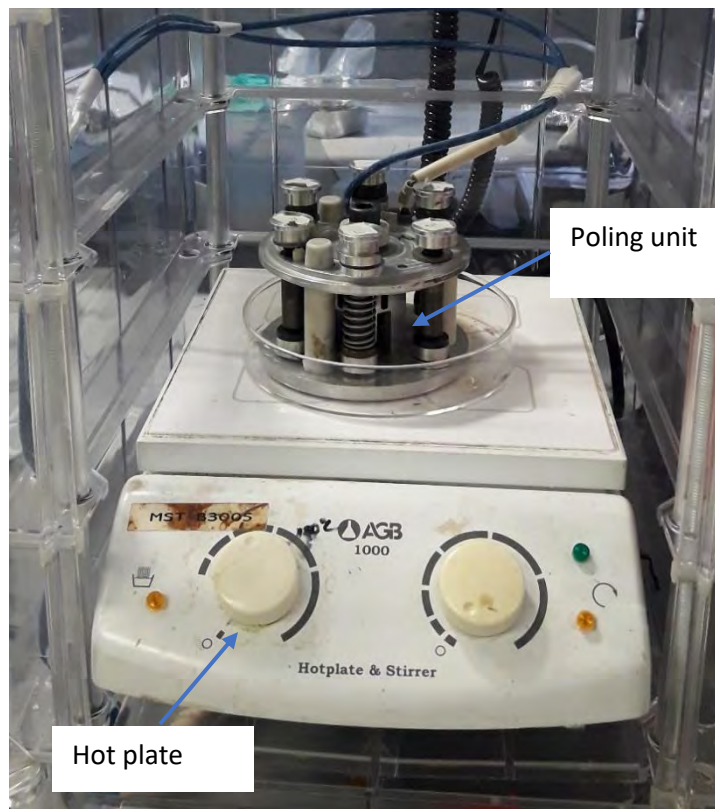


Figure 3-11: Image of the inside of the modified desiccator box containing the polarizing unit and a hot plate. Adapted from[CS lab UL]

The modifications of the desiccator box allow for the safe polarizing of ceramics up to the very high voltages due to the thickness and high insulation properties of the desiccator walls along with the controlled polarizing conditions. The desiccator box was also modified to allow for the safe and easy use of hot plate during polarizing, as shown in Figure 3-11.

3.5.2. Poling procedure

Ceramic samples of bismuth ferrite were prepared for electrical polarization by mechanically polishing each of the 10 mm diameter ceramics to a thickness of 1 mm. To ensure an even distribution of charge and to avoid any electrical discharge, due to un-even surfaces during the polarization, each sample was given a smooth or flat surface. The samples were mechanically polished to achieve this flat surface using a Phoenix 4000 polisher with tungsten carbide paper. The grain size of the tungsten carbide paper was reduced gradually until each samples surface polished down to a 0.6 μm finish, using a silicon suspension and cloth polishing matt. The microstructure of samples was examined under an optical microscope to confirm uniformity throughout the structure.

The BFO ceramic samples were then placed into the polarizing apparatus as shown in figure 3-12. The apparatus consists of a positive and negative aluminum electrode of 15 mm in diameter. A spring was attached to the top, negative electrode ensures constant contact between the electrodes and the sample during the polarizing process. The positive and negative sections of the polarizing apparatus was separated by a ceramic insulator to avoid shorting during the process.

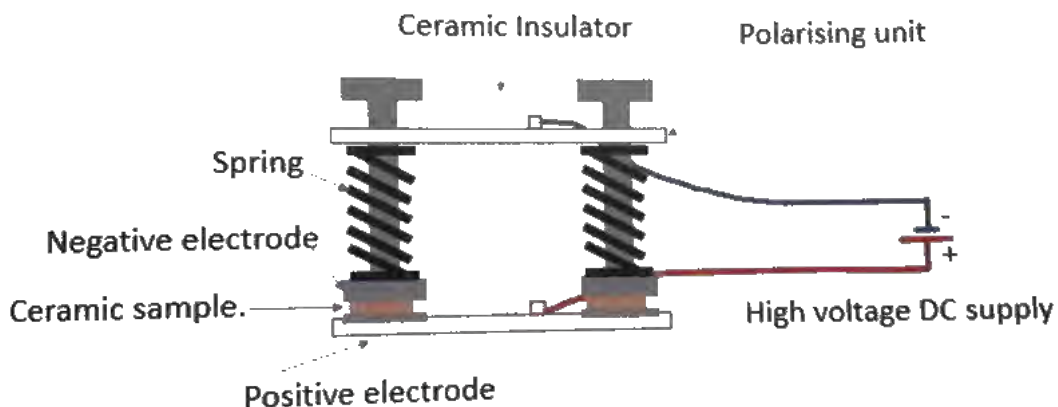


Figure 3-12: Polarizing unit used this research work. (Adapted from [195])

Before polarizing, the entire unit was enclosed in the desiccator box and then connected to the high voltage power supply (PS350, High voltage power supply, 5000 volts, 5mA, Stanford research systems). A temperature of 130 °C was chosen for the polarization process to ensure sufficient motion of the crystallographic domain. This temperature also ensured that the bismuth ferrite was not dehydrated as would occur at elevated temperature.

DC Contact electrical poling was then carried out by heating the sample to the poling temperature at a heating rate 10 °C/min. A DC electric field between 10 kV/cm to 13 kV/cm was then applied to these pellets for 30 minutes each. After 30 minutes the samples were then cooled down to room temperature within the electric field. This cooling process is to ensure the permanent arrangements of the dipoles after poling. D_{33} piezoelectric measurements were then carried out after this poling process.

3.6. Characterization Methods

3.6.1. Phase Study

3.6.1.1. X- Ray Diffraction

All samples of bismuth ferrite were analyzed by X-Ray Diffractometry. X-rays are a type of electromagnetic radiation. The wavelength of x-rays is approximately 1 Å which has the same size equivalent to that of an atom. X-ray diffraction (XRD) is a nondestructive analytical technique mainly used for the phase identification and structural characterization of crystalline materials. X-ray diffraction combined with Rietveld analysis, provides detailed information regarding unit cell dimensions, bond-lengths, bond-angles and the site ordering of crystallites.

X-ray (XRD) analysis is an analytical method used, in which X-rays of a known wavelength are passed through a sample to investigate its crystalline structure. The wave nature of the X-rays used cause them to be diffracted by the lattice structures of the crystal and reflects to give a unique pattern of peaks at different angles and of different intensity depending on the lattice structure. The diffracted beams from atoms in successive planes will cancel out one another through destructive interferences unless they are in phase, and the condition for this is stated by Bragg equation [174]:

$$n\lambda = 2d\sin\theta$$

where λ is the wave length of the x-rays used, d is the distance between different planes of atoms within the crystal lattice and θ is the angle of diffraction.

An x-ray detector, in the XRD machine, moves around the sample stage and measures the intensity and position (angle of diffraction 2θ) of these reflected peaks. This highest peak intensity measured is defined as the 100% peak and intensity of all the other peaks are measured as a ratio of it.

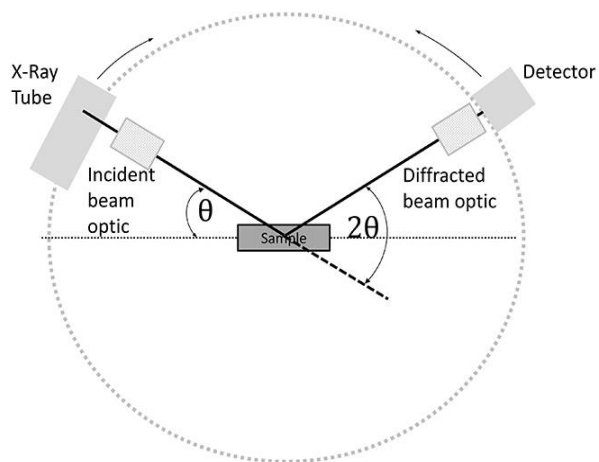


Figure 3-13: Typical features of an XRD Machine. Adapted from[google image]

XRD analysis was carried out on all samples X'Pert Pro MPD X-Ray Diffraction diffractometer (Philips, Almeto, the Netherlands) using graphite mono-chromatized Ni filtered Cu- $K\alpha$ radiation ($\lambda=0.15406 \text{ \AA}$) at 40 kV and 40 mA. A scanning range (2θ) from 20° to 60° with a step size of $0.02^\circ 2\theta/s$ was used throughout the entire process.

XRD analysis was used to access the phases present in the sample, crystallinity and purity of the bismuth ferrite samples as well as its crystallographic properties such as crystal size and lattice parameters.

1) Phase identification

Phase identification of each sample was performed using reference to the library database supplied by the International Centre for Diffraction Data(ICDD) by directly comparing the X-ray diffraction patterns to the Joint Committee for Powder Diffraction Standards(JCPDS) files for the Bismuth ferrite and other common phases present during the synthesis and decomposition of bismuth ferrite. The phase identification was carried out to obtain relative proportions of phases present in the sample. The list of peaks for BFO and the most important peaks of other bismuth and iron rich oxides commonly found within BFO. The phases identified were also checked against that of the database supplied by the ICDD, using the software, X'Pert HighScore Plus, Version 2.2b (PANalytical B.V. Amelo, The Netherlands) and Maud (version 2.8).

2) Purity of Phase

The phase purity of the prepared bismuth ferrite samples in were measured directly from the xiray diffraction patterns obtained using X'Pert HighScore Plus software and Maud. The equation used to calculate the percentage of purity (X_p) of the bismuth ferrite powder is [174]:

$$X_p = \frac{\Sigma Ac - \Sigma Impurity}{\Sigma Ac} \times 100$$

Where ΣAc is the sum of the area under all the bismuth ferrite characteristic peaks and $\Sigma Impurity$ is the sum of the area under all impurity peaks present in the samples between 2θ angles 20° to 80° .

3) Crystallinity

The crystallinity of the bismuth ferrite sample is found by integrating the effects on the XRD of the crystal strain, diffraction domain size and crystal defects. In order to compare the crystallinity of the bismuth ferrite sample the following calculations were made based on the obtained XRD patterns. The percentage of crystallinity (X_c) was determined using [174]:

$$X_c = \frac{\Sigma Ac}{\Sigma Ac + \Sigma Aa} \times 100$$

Where $\Sigma Ac + \Sigma Aa$ is the sum of the area under all the bismuth ferrite crystalline and amorphous peaks respectively and ΣAc yields the sum of the areas under the crystalline peaks present in the scan range between 2θ angles 20° to 80° .

To calibrate the software for crystallinity analysis a constant background parameter needs to be evaluated. This is achieved through calibrating the crystallinity using standard Silicon sample and determining the constant background intensity. This calibration of background intensity is then applied to the tested samples.

4) Texture

The texture of a crystalline sample is the distribution of the crystallographic orientations within a polycrystalline sample. Samples are said bot to have texture which have fully random,

anisotropic, crystallographic orientations. However, samples with an ordered non-random crystallographic orientation are said to have texture. The texture of a sample can vary depending on the percentage crystallographic orientations in a specific direction. A low percentage of orientation in a certain direction is weakly textured inasmuch as a fully isotropic orientation of crystallographic domains is considered as highly textured. The texture of a crystalline material can have a great impact on the materials properties, such as magnetic, optical[161-164] and electrical properties[103,155,157]. The texture of bismuth ferrite ceramics in this experiment is found through orientation Index of the plane N_{hikili} , which is defined as:

$$N_{hikili} = R_{hikili} / R_{hikili}^0$$

This is calculated from X-ray diffraction patterns where R_{hikili} is the intensity ratio of the N plane and R_{hikili}^0 is the intensity ratio taken from a completely randomly orientation powder sample. The intensity ratio of the N plane is described in the following equation.

$$R_{hikili} = I_{hikili} / (I_{h1k1l1} + I_{h2k2l2} + \dots + I_{h_nk_nl_n})$$

Where I_{hikili} is the intensity for the diffraction line $hikili$.

5) Determination of Lattice Parameter

We can define the rhombohedral lattice in two ways: as a trigonal lattice with additional translational vectors, or as a simple lattice with equal primitive vectors making equal angles with one another. The *International Tables* addresses this ambiguity by listing atomic positions for the rhombohedral lattice in a hexagonal setting, where all coordinates are referenced to the conventional cell, and in a rhombohedral setting, where the coordinates are referenced to rhombohedral lattice. To further confuse matters, the unit cell's dimensions might be reported in terms of (**a**, **c**) or in terms of (**a'**, **α**). An article might say that there were N atoms in the rhombohedral cell, or 3N atoms in the conventional cell. One has to pay attention to the context. In the database, the lattice parameters of the system by giving **a** and **c** will be recorded, since that is the usual crystallographic practice. However, atomic positions will be recorded using the rhombohedral primitive vectors, since computer calculations work best with the smallest number of atoms needed to describe the system.

Table 3-2: The space groups associated with the rhombohedral lattice are

146.	R3
148.	R3
155.	R32
160.	R3m
161.	R3c
166.	R3m
167.	R3c

Bismuth ferrite is classed as rhombohedral lattice belonging to the R3c space group.

3.6.1.2. EDS

Energy Dispersive X-Ray Spectroscopy (EDS or EDX) is a chemical microanalysis technique used in conjunction with scanning electron microscopy (SEM). The EDS technique detects x-rays emitted from the sample during bombardment by an electron beam to characterize the elemental composition of the analyzed volume. Features or phases as small as 1 μm or less can be analyzed.

When the sample is bombarded by the SEM's electron beam, electrons are ejected from the atoms comprising the sample's surface. The resulting electron vacancies are filled by electrons from a higher state, and an x-ray is emitted to balance the energy difference between the two electrons' states. The x-ray energy is characteristic of the element from which it was emitted.

The EDS x-ray detector measures the relative abundance of emitted x-rays versus their energy. The detector is typically a lithium-drifted silicon, solid-state device. When an incident x-ray strikes the detector, it creates a charge pulse that is proportional to the energy of the x-ray. The charge pulse is converted to a voltage pulse (which remains proportional to the x-ray energy) by a charge-sensitive preamplifier. The signal is then sent to a multichannel analyzer where the pulses are sorted by voltage. The energy, as determined from the voltage measurement, for each incident x-ray is sent to a computer for display and further data evaluation. The spectrum of x-ray energy versus counts is evaluated to determine the elemental composition of the sampled volume.

3.6.2. Microstructure Study

3.6.2.1. Optical Microscopy

Optical microscopes are categorized on a structure basis according to the intended purpose.

Microscope Basic Functions and Optical System Configuration

An optical microscope consists of the following two major basic functions.

1. Creating a Magnified Image of a Specimen
2. Illuminating a Specimen

The function to create a magnified image of a specimen consists of three basic functions of "obtaining a clear, sharp image", "changing a magnification", and "bringing into focus". An optical system for implementing these functions is referred to as an observation optical system. Meanwhile, the function to illuminate a specimen consists of three basic functions of "supplying light", "collecting light", and "changing light intensity". An optical system for implementing these functions is referred to as an illumination optical system. In other words, the observation optical system projects a sample (specimen) through an optical system and moreover leads a projection image to eyes or a pickup device such as CCD. On the other hand, the illumination optical system effectively collects light emitted from the light source and leads the light to a specimen to illuminate it. The layout of observation and illumination optical systems in an optical microscope is as in the figure below for an upright microscope. Meanwhile, for an inverted microscope the layout relation between those optical systems is upside down at the center of a specimen with respect to an upright microscope.

Principle of Optical Microscope (Compound Microscope)

An optical microscope creates a magnified image of an object specimen with an objective lens and magnifies the image furthermore with an eyepiece to allow the user to observe it by the naked eye. Assuming a specimen as AB in the following figure, primary image (magnified image) A'B' of inverted real image is created with an objective lens (ob). Next, arrange the eyepiece (oc) so that primary image A'B' is located closer to the eyepiece than the anterior focal point, then more enlarged erect virtual image A''B'' is created. Put your naked eye in the eye (pupil) position on the eyepiece barrel to observe the enlarged image. In short, the last image to be observed is an inverted virtual image. As described above, this type of microscope which creates a magnified image by combining an objective lens making an inverted real image and an eyepiece making an erect virtual image is called a compound microscope. The observation optical system in an optical microscope is commonly standardized on this compound microscope. Meanwhile, such type of microscope that directly observes an inverted real image magnified with an objective lens is

called a single microscope. A microscopic observation on a TV monitor, recently popularized increasingly, uses the way of directly capturing this inverted real image with a CCD camera, thereby being comprised of a simple microscope optical system.

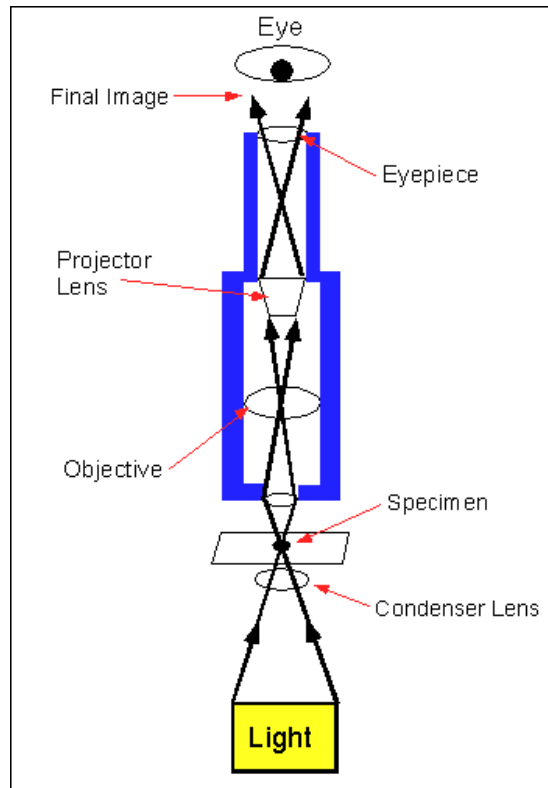


Figure 3-14: Schematic showing principle of Optical Microscope. Adapted from[google image]

To observe sample in the microscope it is needed to undertake etching. For ceramic materials etching is different than metallic materials. Normally thermal etching is performed for ceramic materials. In this research work, thermal etching was carried out 100 °C below the respective SPS sintering temperature.

- **Thermal etching**

The invention relates to a process for the thermal etching of a ceramic under oxidizing conditions with the particular aim of revealing its grain boundaries and studying its granular microstructure. The thermal etching is performed in a furnace or kiln under a controlled atmosphere(air).

The structural study of a material generally involves a careful metallographic preparation of said material for the morphological analysis thereof. In order to study the structure, it is necessary to

render visible the different constituent elements thereof and consequently, precisely reveal the grain boundaries in order to permit the measurement of the size of the grains of the material. In the case of polyphase materials, the size of the grains must be measured on each phase independently.

3.6.2.2. Scanning Electron Microscopy

To observe the grain size and morphology of the samples, Field Emission Scanning Electron Microscope [FESEM: JEOL JSM 7600F] was used (figure 3-15). Prior to insertion in the FESEM, the samples were coated with platinum by ion sputtering method. This is required to make the sample conductive and so circumvent the charging phenomenon. Grain size was estimated by the linear intercept method.



Figure 3-15: Field Emission Scanning Electron (**FESEM**). Adapted from [GCE lab BUET]

3.6.3. FTIR

Fourier transform infrared spectroscopy (FTIR) is a technique which is used to obtain an infrared spectrum of absorption or emission of a solid, liquid or gas. An FTIR spectrometer simultaneously collects high spectral resolution data over a wide spectral range. This confers a significant advantage over a dispersive spectrometer which measures intensity over a narrow range of

wavelengths at a time. The term *Fourier transform infrared spectroscopy* originates from the fact that a Fourier transform (a mathematical process) is required to convert the raw data into the actual spectrum.

The goal of any absorption spectroscopy such as FTIR is to measure how well a sample absorbs light at each wavelength. When a material is irradiated with infrared radiation, absorbed IR radiation usually excites molecules into a higher vibrational state. The wavelength of light absorbed by a particular molecule is a function of the energy difference between the at-rest and excited vibrational states. The wavelengths that are absorbed by the sample are characteristic of its molecular structure. Thus, FTIR Analysis is used to:

- Identify unknown materials
- Identify and/or quantify surface contamination on a material

In figure 3-16, left one (**Perkin Elmer Spectrum 100**) used for solid or pellets materials and right one (**Perkin Elmer Spotlight 200**) is used for powder or liquids materials.



Figure 3-16: FTIR Analyzer. Adapted from [CS lab UL]

As of this project, the FTIR spectrometer used an interferometer to modulate the wavelength from a broadband infrared source. A detector measured the intensity of transmitted or reflected light as a function of its wavelength. The signal obtained from the detector was an interferogram, which was analyzed with a computer using Fourier transforms to obtain a single-beam infrared spectrum. The FTIR spectra are usually presented as plots of intensity versus wavenumber (in cm^{-1}

¹). Wavenumber is the reciprocal of the wavelength. The intensity was plotted as the percentage of light transmittance or absorbance at each wavenumber. As of this work, the intensity was plotted as the percentage of light transmittance at each wavenumber.

3.6.4. Ferroelectric Property measurements

3.6.4.1. Piezoelectric measurements

d_{33} Piezometer, Piezotest, Model PM300 was used in this research work. The setup consists of an oscillation impact hammer with adjustable oscillation frequency, two direct contact electrodes, a charge amplifier, a control unit, a load cell and the sample to be tested. The mini impact hammer has a metal tip with diameter of 10. When the hammer taps the specimen, the load cell measures the input force and the charge amplifier measures the charge generated by the ceramic. Both the measure force and charge are sent to the control output unit, where their peak amplitudes are reduced.



Figure 3-17: Piezo Meter and one of readings of the prepared BFO sample SPS sintered at 825 °C. Adapted from[CS lab UL]

The piezometer was set to d_{33} very low range with a range between 0 to 10 pC/N ($\pm 2\%$, ± 0.01 pC/N) and a loading of 0.1 μ F. the test frequency used throughout the experiment was 111 Hz (± 0.1 Hz) with a static force of approximately 10 N used to grip the sample and the testing is by the oscillatory force pf between 0.05 N to 0.5N.

The d_{33} measurements on the bismuth ferrite ceramic were calculated by the following expression:

$$d_{33} = - \frac{C_s V}{F}$$

where C_s is the capacitance of the sample, F is the applied force and V is the responding Voltage. C_s is defined as:

$$C_s = \int_A \epsilon_{33} dA/d$$

Where A is the area of the sample, d is the thickness and ϵ_{33} is the permittivity.

- **Piezoelectric Effect**

The piezoelectric effect, explained with a simple molecular model shown in figure 3-17, is the generation of an electric charge as a result of a force exerted on the material. Before subjecting the material to an external stress, the centers of the negative and positive charges of each molecule coincide—resulting into an electrically neutral molecule as indicated in figure 3-18 (a). However, in presence of an external mechanical stress the internal reticular can be deformed, thus causing the separation of the positive and negative centers of the molecule and generating little dipoles as indicated in figure 3-18 (b). As a result, the opposite facing poles inside the material cancel each other and fixed charges appear on the surface. This is illustrated in figure 3-18 (c). That is to say, the material is polarized and the effect called direct piezoelectric effect. This polarization generates an electric field that can be used to transform the mechanical energy, used in the material's deformation, into electrical energy.

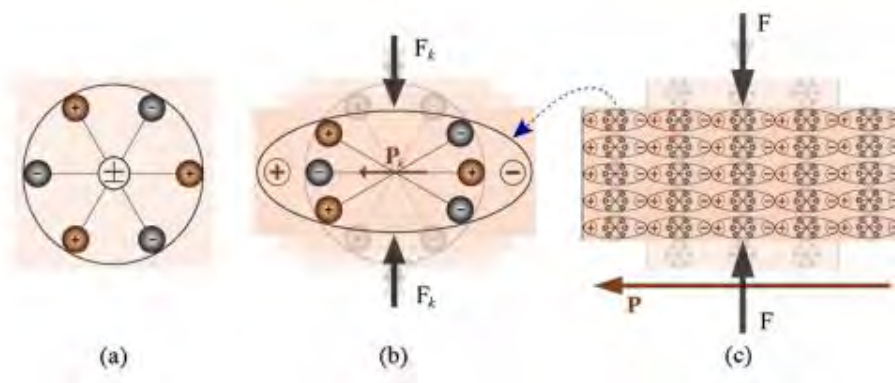


Figure 3-18: Piezoelectric effect explained with a simple molecular model: (a) An unperturbed molecule with no piezoelectric polarization (though prior electric polarization may exist); (b) The molecule subjected to an external force (F_k), resulting in to polarization (P_k) as indicated; (c) The polarizing effect on the surface when piezoelectric material is subjected to an external force. (Figure adapted from [192]).

3.6.4.2. Loop Test

Loop testing is a white box testing technique performed to validate the Polarization vs. Applied Electric Field (P-E) loops and thus to measure the ferroelectric property of the given sample. A P-E loop for a device is a plot of the charge or polarization (P) developed, against the field applied to that device (E) at a given frequency.

The P-E loop measurement was done in our case using precision impedance analyzer [WAYNE KERR 6500B series]. For the acquisition of a P-E loop, the initial wave shape was formed by the function generator, which was then amplified by the high voltage amplifier, which sent the amplified waveform to the sample. The current passing through the sample was then converted to a voltage, which was captured on a digital storage oscilloscope, along with the monitor output from the high voltage amplifier, and waveforms from any displacement measuring devices connected. The captured waveforms were then sent to the computer for subsequent analysis.

Here, the current input goes to the inverting input and the gain of the converter depends on the value of the feedback resistor, such that the current at any instant I is:

$I = V_{out} / R_{st}$; where R_{st} = reference, or 'standard', resistor.

3.6.5. Magnetic property measurement

The magnetization response of the samples with changing magnetic field i.e. the M-H loop was determined using a Vibrating Sample Magnetometer in figure 3-19 [VSM: Model EV-9, Microsense LLC, USA].



Figure 3-19: Vibrating Sample Magnetometer (VSM). Adapted from [google image]

A small piece of the sample (15-35 mg) was broken off and put in the instrument after weighing. Magnetic field as high as 20 kOe was used. The output data of the machine was divided by the weight of the sample (in grams) to obtain the magnetization value in the widely used emu/g units.

3.6.6. Raman Spectroscopy

Raman spectroscopy is one of the vibrational spectroscopic techniques used to provide information on molecular vibrations and crystal structures. This technique uses a laser light source to irradiate a sample, and generates an infinitesimal amount of Raman scattered light, which is detected as a Raman spectrum using a CCD camera. The characteristic fingerprinting pattern in a Raman spectrum makes it possible to identify substances including polymorphs and evaluate local crystallinity, orientation and stress. This spectroscopy detects primarily symmetric molecular vibrations, which results in simpler spectra with minimal overtone or combination bands [175] than, i.e, infrared (IR) spectroscopy Raman shifts are typically reported in wavenumbers, which have units of inverse length, as this is directly related to energy.

When light is scattered by matter, almost all of the scattering is an elastic process (Rayleigh scattering [176,177]) and there is no change in energy. However, a very small percentage of scattering is an inelastic process, thus a scattered light has different energy from incident light. This inelastic scattering of light was predicted theoretically by Adolf Smekal in 1923 [178] and first observed experimentally by Chandrasekhara Venkata Raman in 1928, which is why this inelastic scattering is called Raman scattering (Raman effect).

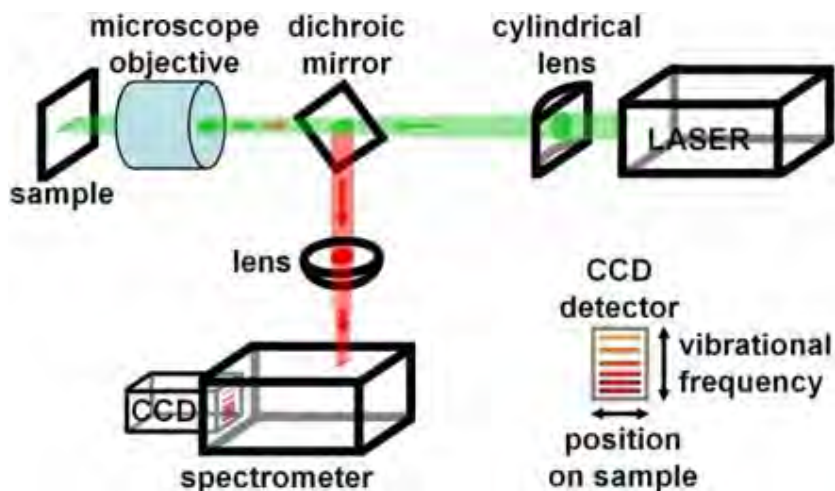


Figure 3-20: Schematic diagram showing the working principle of Raman spectroscopy.

Figure 3-20 shows schematic diagram showing the working principle of Raman spectroscopy. In this work, Raman spectroscopy was used for these following operations which are listed below

- a) **To identify unknown substance** (constituents or elements expect Bi, Fe, O): When foreign material is discovered on the surface of manufactured goods or inside a transparent film, a spectrum can be taken for identification. Raman spectroscopy can analyze buried material, or particles of foreign material smaller than 1 micron which cannot be measured by FTIR. Because Raman spectroscopy is also sensitive in lower frequency regions of the spectrum, identification of inorganic material is also possible.
- b) **To identify polymorphs**: Crystal polymorphism of a material occurs when the chemical formula is the same but the crystal structure of the material is different. This such spectroscopy allows for analysis of crystal polymorphism of BFO, with similar but slight differences in position and intensity ratios of particular peaks between polymorphs, sufficient for identification.
- c) **To track the change in molecular structures**: By recording the Raman spectrum over time, I can follow changes in the molecular structure of the bismuth ferrite sample.
- d) **To track a change in crystallinity**: In BFO sample where the crystallinity changes with heating, changes can be analyzed using the Full Width at Half Maximum (FWHM) of the peak appearing in the Raman spectrum. By performing peak fitting, it is possible to quantify the FWHM and thus carry out quantitative analysis.

Chapter 4: Results and Discussions

In this chapter elaborate results and discussion will be outlined with details explanation for each finding as well as the relevant experimental results and thoroughly explain the relevance of each result.

4.1. Density Measurements

4.1.1. Effect of Sintering Parameters on Density

For desirable optical, electric and magnetic properties, dense samples are a prerequisite. So, the initial goal of this research was to optimize the sintering parameters of the samples. By optimize, it is meant those conditions that produce samples having good percent theoretical density and grain size around $\sim 1\mu\text{m}$.

Figure 4-1 shows final SPS sintered BFO pellets sintered at 625, 700, 750, 800, 825°C respectively.



Figure 4-1: Prepared BFO pellets SPS sintered at 625, 700, 750, 800, 825°C respectively.

Experimentally density of all samples was measured using the formula mass divided by volume. Honestly it won't be possible to get 100% accuracy if the dimensions of the samples are inaccurate. As all BFO samples showed good dimensional accuracy like uniform thickness, Density and %Theoretical Density of all samples are listed in the following table:

Table 4-1: Density and %Theoretical Density of BFO-625, BFO-700, BFO-750, BFO-800 and BFO-825 samples.

Sample Identity	Density (gm/cm ³)	% Theoretical Density
BFO-625	6.00333	72.16
BFO-700	7.47451	89.84
BFO-750	7.83573	94.18
BFO-800	7.66722	92.15
BFO-825	7.11918	85.57

In this analysis BFO-625 showed lower density. Possible reasons behind this lower value was at 625°C holding time 5 minutes wasn't sufficient. At that lower temperature holding time should be 15-20 minutes [185] at 50 MPa applied pressure. BFO-750 showed the higher density so called higher %theoretical density among the all samples. Undoubtedly BFO-750 was the densest product would show optimum properties than rest of the samples. Again, another interesting thing is that density increased from BFO-625 to BFO-750 gradually and decreased upto BFO-825. In BFO-800 slight decrease in density might be happened due to a bit evaporation of $\text{Bi}_2\text{O}_3/\text{Bi}$ at 800°C as at temperatures above 750°C BiFeO_3 becomes unstable and decomposes [186]. At temperature 825°C, 20-25% weight was lost as BFO-825 was melted slightly at this higher temperature.

4.2. Microstructure Analysis

4.2.1. OM Micrograph Analysis

For ceramic sample thermal etching is more convenient precedence for the observation of the microscope. For all samples thermal etching was carried out at the temperature 100°C below the respective SPS temperature. Holding time was 1 hour at that respective temperature. Unfortunately, there was no any grain/grain boundaries were seen at BFO-625, BFO-700, BFO-750 and BFO-825. It was found some grain as well as grain boundaries in BFO-800 sample.

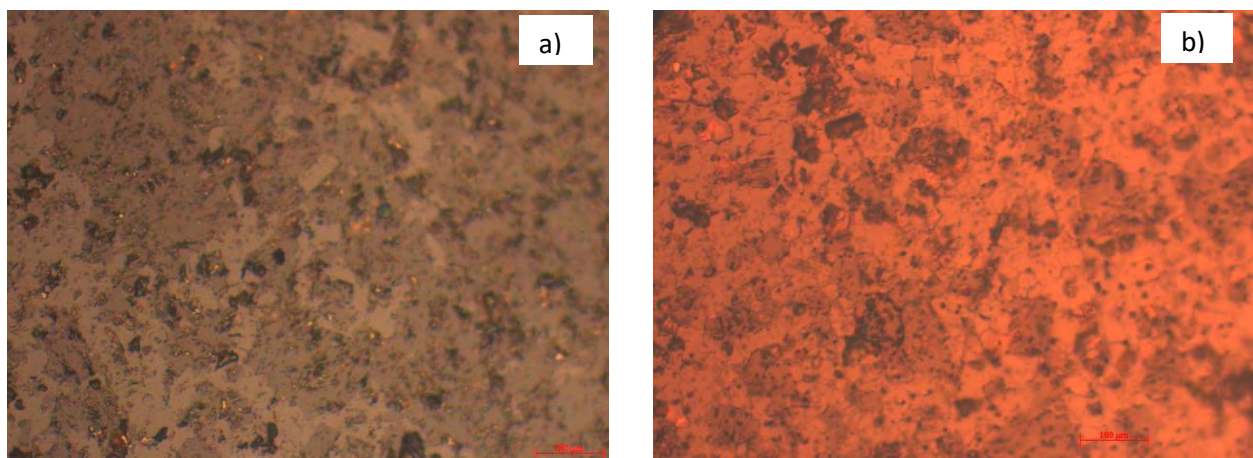


Figure 4-2: Microstructure of BFO-800 sample-a) Before etching, b) After etching

In BFO-800 sample no grains were seen before etching but after etching a remarkable amount of grains along with grain boundaries were observed. Actually, thermal etching at 700 °C made the

grain boundaries thermally activated as grain boundaries are higher energy state and this induces oxidation of surface features at different rates, to reveal various features. So, grain and grain boundaries were seen after the thermal etching.

4.2.2. SEM Analysis

SEM micrographs obtained from the SPS-prepared samples are represented in (Figure 4-3). The SPS-prepared samples exhibit uniform microstructures and their average grain sizes increase gradually with increasing sintering temperature, but they are smaller than ~220 nm up to temperature 750 °C. However, as compared with the SPS-prepared samples, the conventionally prepared sample exhibits less uniform microstructure and larger average grain size, being larger than ~300 nm[37]. In BFO-825 grain size was 0.5030 μm which was the highest in value amongst the all samples. Indeed, this higher temperature was responsible for this increased value.

This should be due to the lower temperature and shorter soaking time employed in the SPS processing as compared with the conventional synthesis [1-5,10,13]

Table 4-2: Comparative study on Grain Size of SPS prepared BFO sample

Sample ID	Grain Size (μm)
BFO-625	0.1157
BFO-700	0.1620
BFO-750	0.2183
BFO-800	0.2787
BFO-825	0.5030

Again, during the heating and soaking of SPS, a pressure of 50 MPa was constantly maintained to the samples, which could easily make the precursor powders deform easily and aggregate closely, so that the SPS-prepared sample is denser.

However, in our previous work[199], it was found that co-doping (Ba and Ta) on BFO has a significant effect on the grain size hence the properties of materials. Ta has a retarding effect on grain growth hence creates finer grain. If SPS of this co-doped BFO will be done it is assumed that grain size might be less than conventional method whose have grain size range 0.11-0.30 μm.

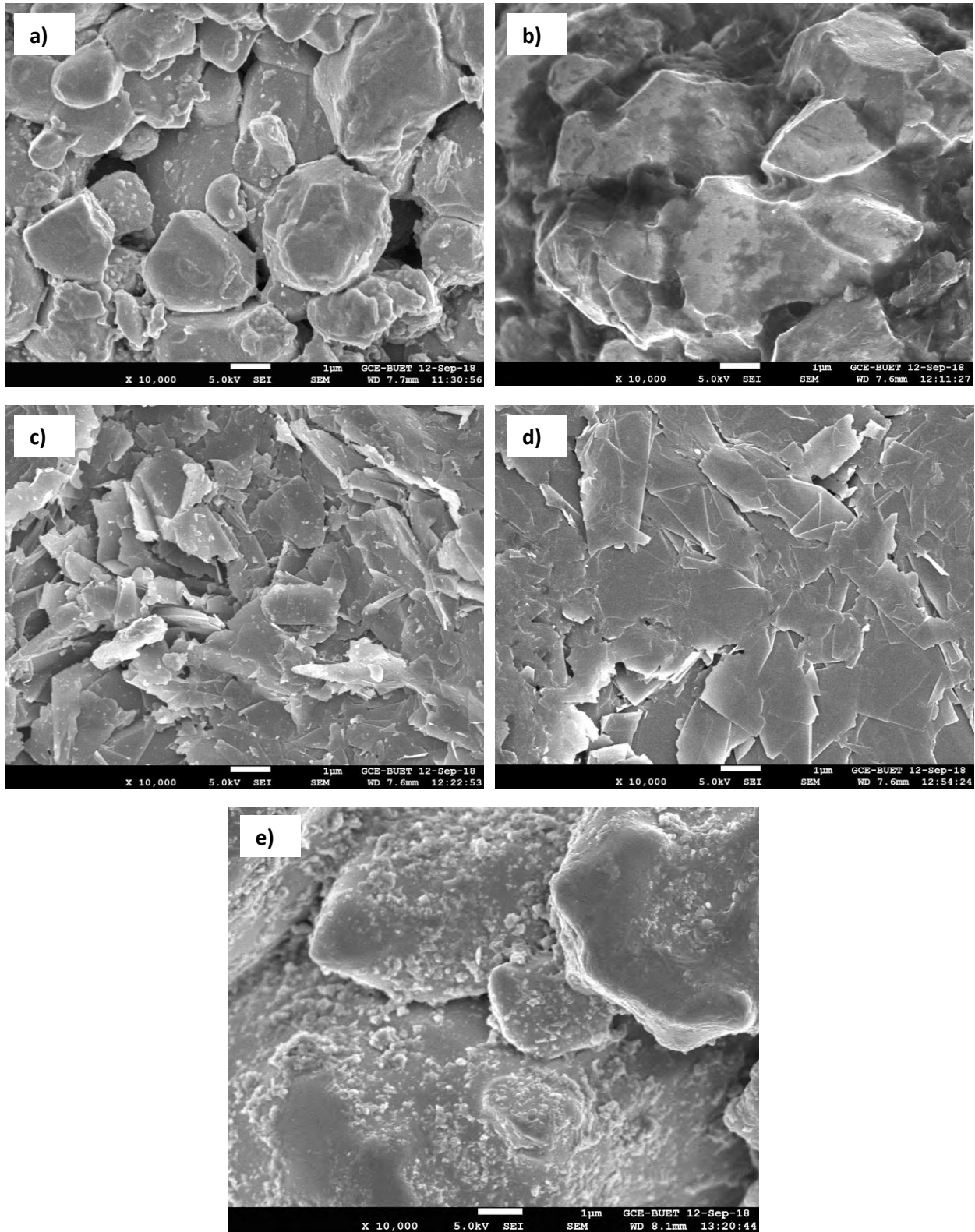


Figure 4-3: SEM micrographs of the pellets sintered by SPS and thermal etched for a) BFO-625, b) BFO-700, c) BFO-750, d) BFO-800, e) BFO-825. The magnification for all the images is 10,000.

From FESEM it was revealed that BFO-625 (figure 4-3 a) showed slightly higher porosity that was responsible for lower density /percent theoretical density. BFO-750 showed the higher density so called higher %theoretical density among the all samples. Undoubtedly BFO-750 (figure 4-3 c) was the densest product would show optimum properties than rest of the samples which has minimum porosity. Again, another interesting thing was that density increased from BFO-625 to BFO-750 gradually and decreased up to BFO-825. In BFO-800 slight decrease in density might be happened due to a bit evaporation of $\text{Bi}_2\text{O}_3/\text{Bi}$ at 800°C as at temperatures above 750°C BiFeO_3 becomes unstable and decomposes [186]. At temperature 825°C , 20-25% weight was lost as BFO-825 is melted slightly at this higher temperature. In BFO-825 (figure 4-3 e) incipient melting is occurred along grain boundaries due to hot spot formation.

Further investigations need to be done in order to identify with certainty the mechanism of microstructural changes.

4.3. EDS Analysis

X-ray energy dispersive spectroscopy (EDS) attached to SEM was used to find elemental composition of prepared sample, which fairly agreed with expected stoichiometry of the compound.

The chemical analysis of SPS sintered samples was carried out by EDS measurements. EDS spectra of BFO-625 samples was shown in figure 4-4 respectively. It was seen that the required peaks were formed in the EDS spectra of BFO-625, BFO-700 and BFO-825 sample in figure 4-4 a), b) and e) respectively. From these findings it was confirmed the formation of bismuth, iron, and oxygen peaks which indeed confirmed the BFO formation in these respective samples.

It was expected that required peaks of bismuth, oxygen and iron would be shown by analysis of the rest of the samples. Surprisingly there was no peaks of Fe was in seen in BFO-750 and BFO-800 samples which engrossed in the figure 4-4 c) and d) respectively. Possible reasons behind this deviousness there maybe segregation occurred in these two samples. It had been really reasonable to think sample segregation prior to other unidentified causes.

The EDX results clearly ensured that the presence of essential elements for the successful synthesis of the BFO-based material. Analysis of the Bi:Fe atomic ratio gave a value of ~ 1 [38].

Thus, from the values of the peak intensities obtained from the EDX spectrum the atomic ratio of Bi:Fe:O is found to be approximately 1:1:3.

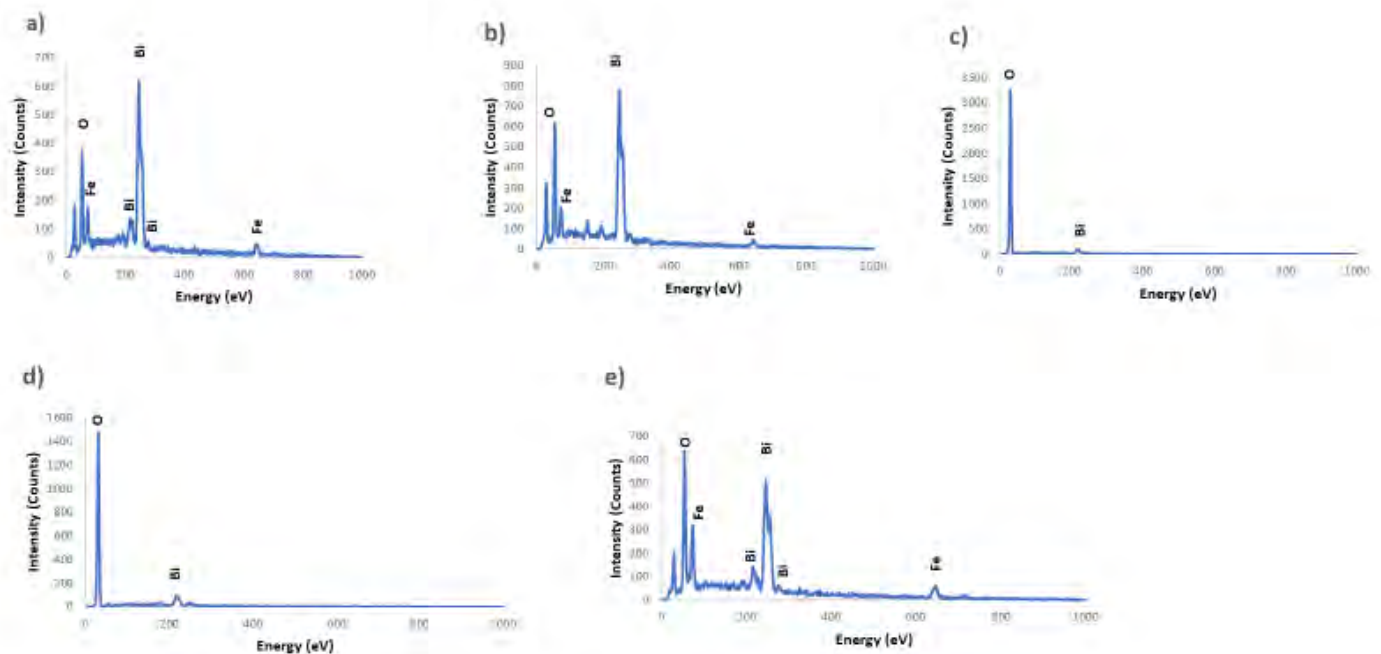


Figure 4-4: EDS mapping of SPS prepared BFO sample showing O, Fe and Bi elements where a) BFO-625, b) BFO-700, c) BFO-750, d) BFO-800, e) BFO-825.

4.4. XRD Analysis

Figure 4-5 shows the XRD patterns at room temperature of BFO samples (BFO-calcined powder, BFO-625, BFO-700, BFO-750, BFO-800 and BFO-825) indicating that BFO structure was indeed formed. The diffraction peaks belong well to the rhombohedrally distorted perovskite structure (PDF 1001090) with same space group $R3c$. The XRD results also reveal no impurity phases present in the powders. The SPS-prepared pellets were polished to remove surface layer followed by XRD analysis. The diffraction pattern of BFO-700, BFO-750 and BFO-825 showed second phase in it.

In order to obtain the detailed crystal structure parameters of BFO ceramics, Rietveld refinements were used to analyze the XRD data of the samples using MAUD (version 2.8). To model a crystal structure with the Rietveld refinement, we must fit a large number of experimental parameters in addition to the crystallographic parameters.

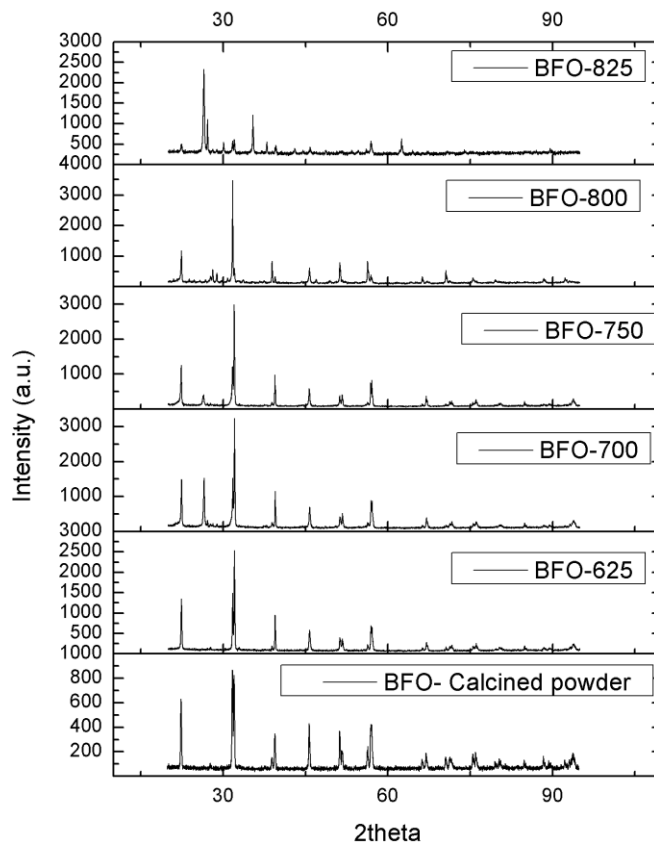


Figure 4-5: XRD patterns of BFO samples (BFO-calcined powder, BFO-625, BFO-700, BFO-750, BFO-800 and BFO-825).

The Rietveld refinement of the XRD patterns for of BFO ceramics was performed using same space group, i.e. R3c and the structural model allowed us to reproduce all the observed peaks in (figure 4-6). The initial Rietveld refinement was carried out by zero point shift, the unit cell and background parameters.

After a good match, the peak positions were achieved, the peak profile parameters including the peak symmetry were refined. Rietveld refinement confirmed the formation of a single phase in BFO-calcined powder and BFO-625. Rietveld data for BFO-700, BFO-750, BFO-800 and BFO-825 samples showed impurities in them. But impurity phase in BFO-750 was in tiny amount than rest of the samples.

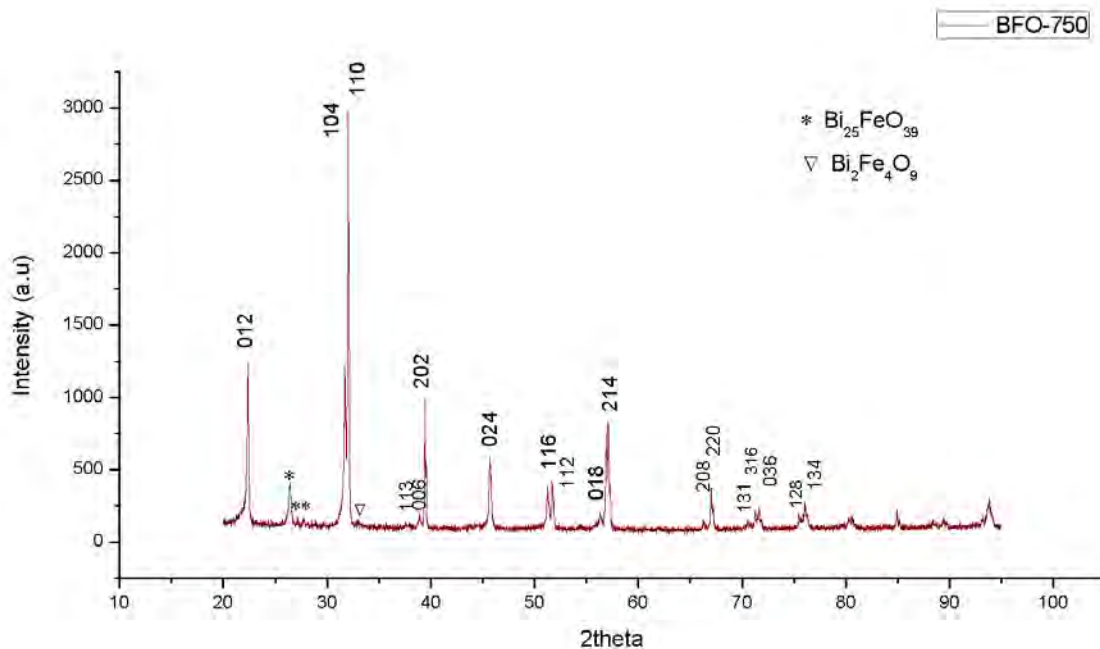


Figure 4-6: XRD Patterns of BFO-750 sample showing respective peaks with a tiny amount of 2ndary phase.

But an unexpected peak was seen in BFO-700 in XRD spectra analysis at 2theta around 25°. Suspected reason on that case there could be segregation occurred on the following sample.

The detailed parameters obtained from Rietveld refinements are listed in table 4-3:

Table 4-3: Structure Parameter of the refined BFO samples

Sample Identity	Lattice Parameters (Å°)	Volume (Å ³)
BFO-Calcined Powder	a=b=5.582294 c=13.877985	374.5264176
BFO-625	a=b=5.5810156 c=13.8772335	374.3346253
BFO-700	a=b=5.5809193 c=13.879375	374.3794716
BFO-750	a=b=5.5795054 c=13.875759	374.0923313
BFO-800	a=b=5.583673 c=13.876163	374.6622850
BFO-825	a=b=5.5808897 c=13.876422	374.2958475

Lattice parameters in BFO- calcined power was nearly close to value given the PDF. With increasing SPS sintering temperature lattice parameters changed due to the slight distortion of rhombohedral structure. BFO-750 possessed the lowest volume than other samples that implies it was supposed to be densest one.

4.4.1. Origin of 2nd phases

According to the phase diagrams (figure 4-7), slight deviations from the stoichiometric composition would result in a mixture of BiFeO_3 and $\text{Bi}_{25}\text{FeO}_{40}$ phases if we move to Bi_2O_3 rich compositions or in a mixture of BiFeO_3 and $\text{Bi}_2\text{Fe}_4\text{O}_9$ if we move to the Fe_2O_3 rich area, but it would be possible to obtain a pure BiFeO_3 with a careful stoichiometric control.

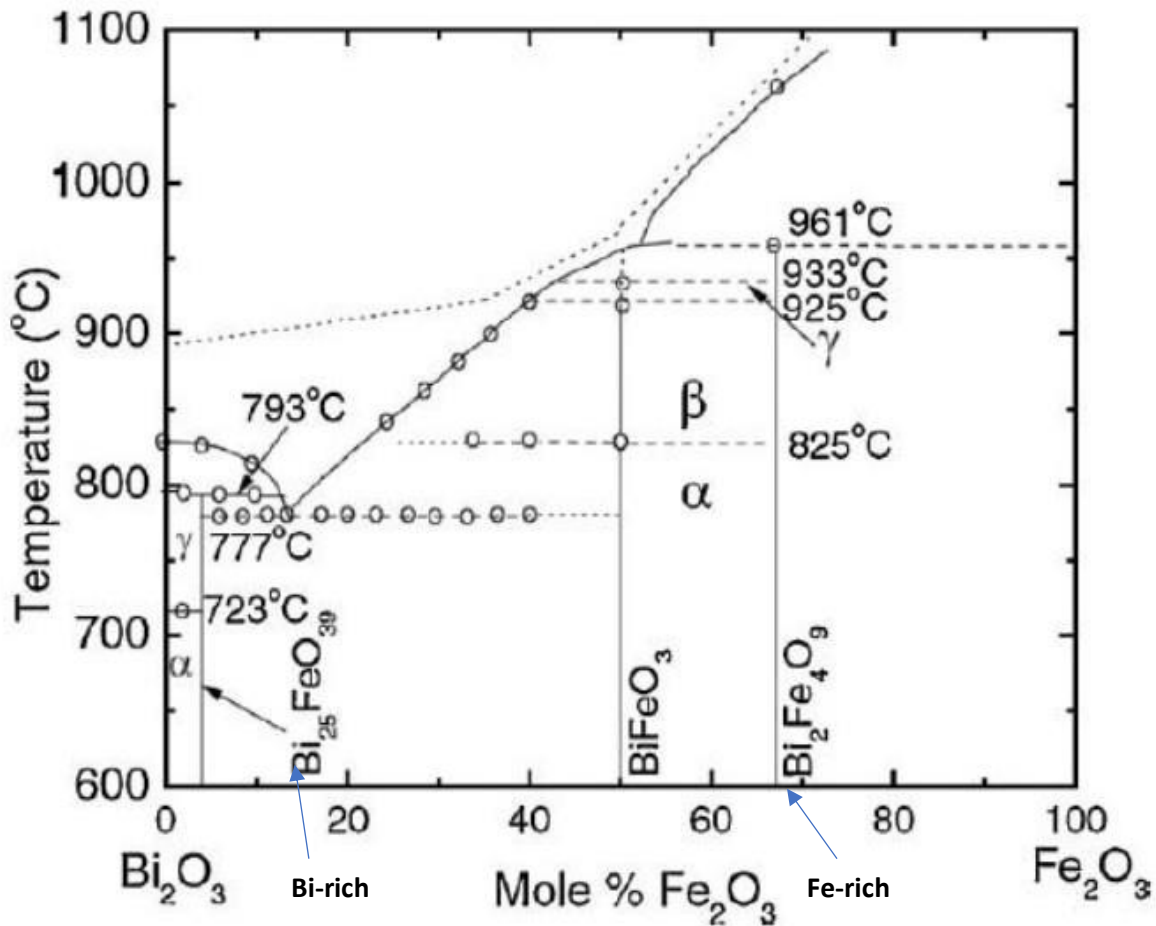


Figure 4-7: Compositional phase diagram of the Bi_2O_3 - Fe_2O_3 system proposed by Palai et al. [94] (adapted from [94]).

Furthermore, the coexistence of the three phases in an equilibrium state has been as well reported [187], although according to the Gibbs phase rule this situation is in fact incompatible for a binary system. Based on this idea Valant et al. [187] suggested that in the presence of tiny amounts of impurities, the $\text{Bi}_2\text{O}_3\text{-Fe}_2\text{O}_3$ system behaves as a pseudo-binary system: slight deviations from the nominal composition will considerably increase the proportion of secondary phases, particularly if impurities are incorporated into the $\text{Bi}_{25}\text{FeO}_{39}$ bismuth-rich phase (the corresponding phase field in the phase diagram would significantly narrow).

In BFO-825 XRD patterns was totally different as 825°C is higher temperature. However, due to a bit evaporation of $\text{Bi}_2\text{O}_3/\text{Bi}$ could be happened at higher temperature. Lebeugle et al. mentioned that at temperatures above 750°C BiFeO_3 becomes unstable and decomposes [186].

Moreover, some other authors assert that bismuth ferrite is actually a metastable phase [188,189], so under certain conditions it will decompose to yield the secondary $\text{Bi}_2\text{Fe}_4\text{O}_9$ and $\text{Bi}_{25}\text{FeO}_{39}$ phases according to the following reaction:



Again, the conditions at which BiFeO_3 decomposes are source of paradox. For example, Morozov et al. [190] stated that BiFeO_3 decompose at temperatures higher than 780°C . On the contrary, Carvalho et al. [188] avowed that BiFeO_3 decomposes at temperatures below 600°C , being possible to obtain a pure phase with a fast cooling that avoids its decomposition.

So, the co-existence of both phases $\text{Bi}_{25}\text{FeO}_{39}$ or $\text{Bi}_{25}\text{FeO}_{40}$ (Sillenite) and $\text{Bi}_2\text{Fe}_4\text{O}_9$ (Bi2) in the BFO structure can be appeared during the study include:

- a) Decomposition at low peritectic decomposition temperature
- b) Evaporation of Bi and /or Bi_2O_3
- c) Insufficient reaction time
- d) Impurities affect solubility of 2ndary phases

Remedy of 2nd phases:

According to Selbach et al. [189] asserted that BiFeO_3 is metastable from 447 up to 767°C . In this range of temperatures, the $\text{Bi}_2\text{Fe}_4\text{O}_9$ and $\text{Bi}_{25}\text{FeO}_{39}$ secondary phases would have a slightly higher stability than BiFeO_3 . Thus, the pure BiFeO_3 phase could be obtained at temperatures slightly higher than 767°C , with a fast heating to avoid the initial formation of $\text{Bi}_2\text{Fe}_4\text{O}_9$ and $\text{Bi}_{25}\text{FeO}_{39}$

phases and a fast cooling to avoid the decomposition of the BiFeO₃ reacted phase. Due to the small Gibbs energy difference between the BiFeO₃ and the decomposition products (Bi₂Fe₄O₉ and Bi₂₅FeO₃₉) minor variations may shift the equilibrium of the BiFeO₃ formation/decomposition reactions given below:



To avoid the formation of unwanted phases SPS can play a vital role. We know one of the most winsome advantages of SPS is high heating rate and less holding time. So, SPS can restrict the unwanted sintering reactions in highly reactive systems as opposed to conventional sintering and hence formation of undesirable product phases can be avoided.

4.5. Magnetic Property Measurement

Magnetic hysteresis loops of the samples are shown in figure 4-8, 4-9, 4-10, 4-11, 4-12, 4-13 for BFO-625, BFO-700, BFO-750, BFO-800, BFO-825 and Compilation of all samples respectively.

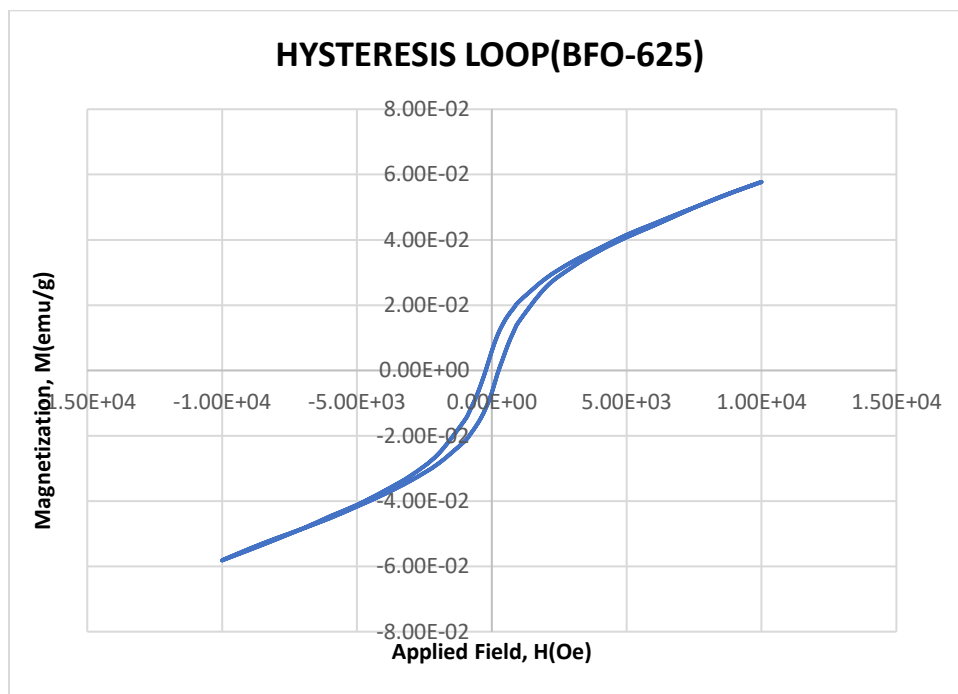


Figure 4-8: Magnetization vs Applied Magnetic Field for SPS Sintered BFO-625.

The SPS-prepared BFO samples showed the small spontaneous magnetization in contrary to antiferromagnetic bulk BFO. The ferromagnetic behavior in BFO arises due to suppression of the known spiral spin structure, presence of oxygen vacancies, valance fluctuation of Fe³⁺ and Fe²⁺ cations [196]. In bulk BFO, the presence of spiral spins arrangement of wavelength 62 nm is

responsible for the suppression of magnetization [197]. This happens because of the external surface spin contribution in comparison to the bulk perovskite ferrite (ABO_3).

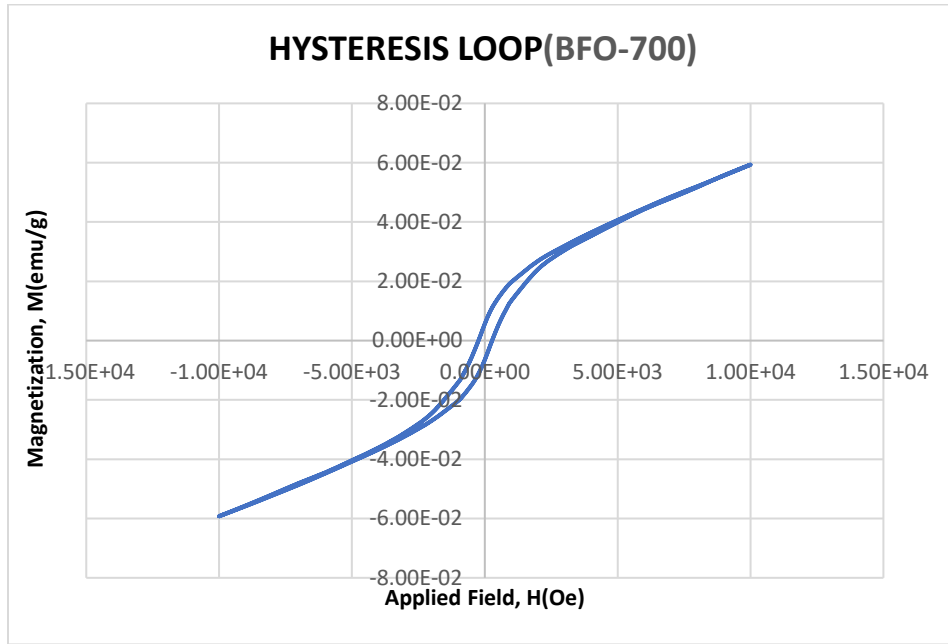


Figure 4-9: Magnetization vs Applied Magnetic Field for SPS Sintered BFO-700.

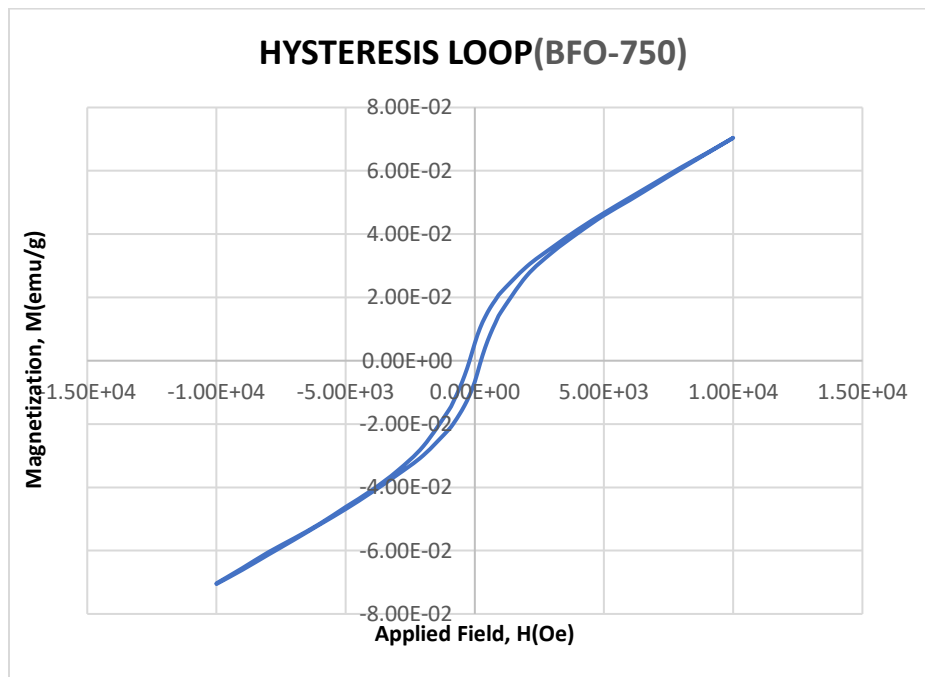


Figure 4-10: Magnetization vs Applied Magnetic Field for SPS Sintered BFO-750.

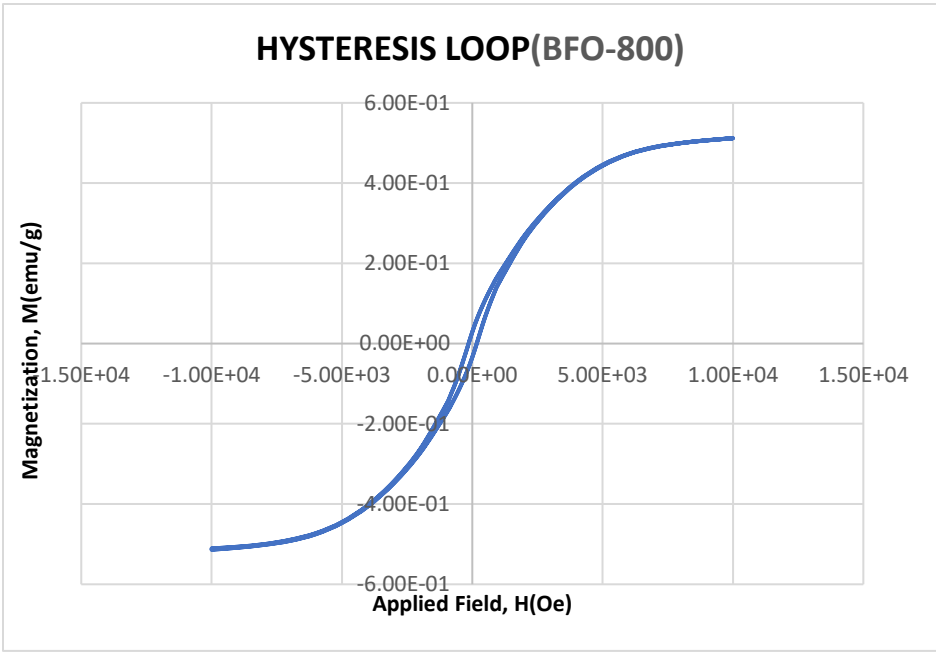


Figure 4-11: Magnetization vs Applied Magnetic Field for SPS Sintered BFO-800.

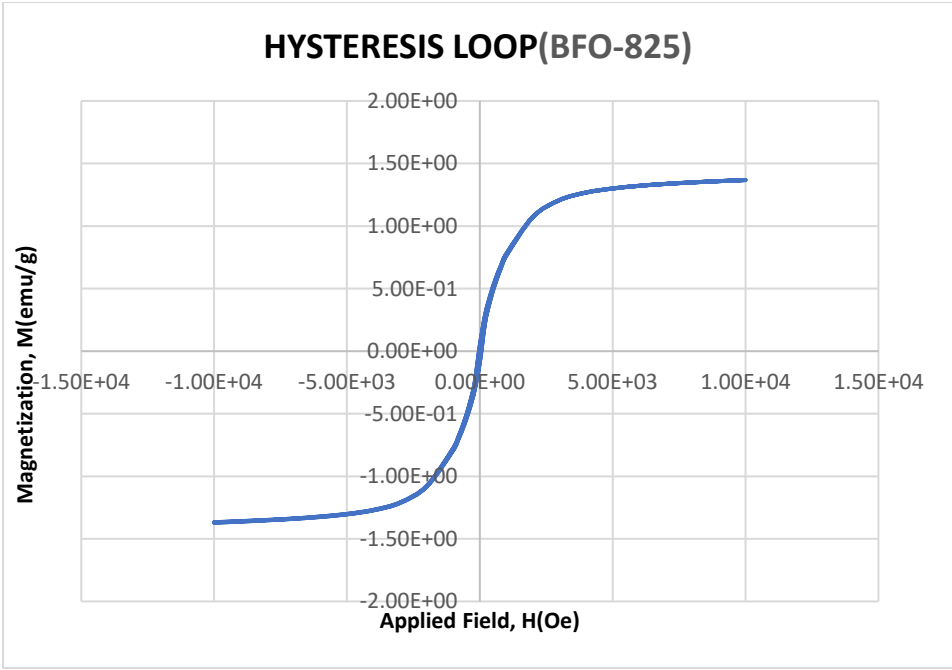


Figure 4-12: Magnetization vs Applied Magnetic Field for SPS Sintered BFO-825.

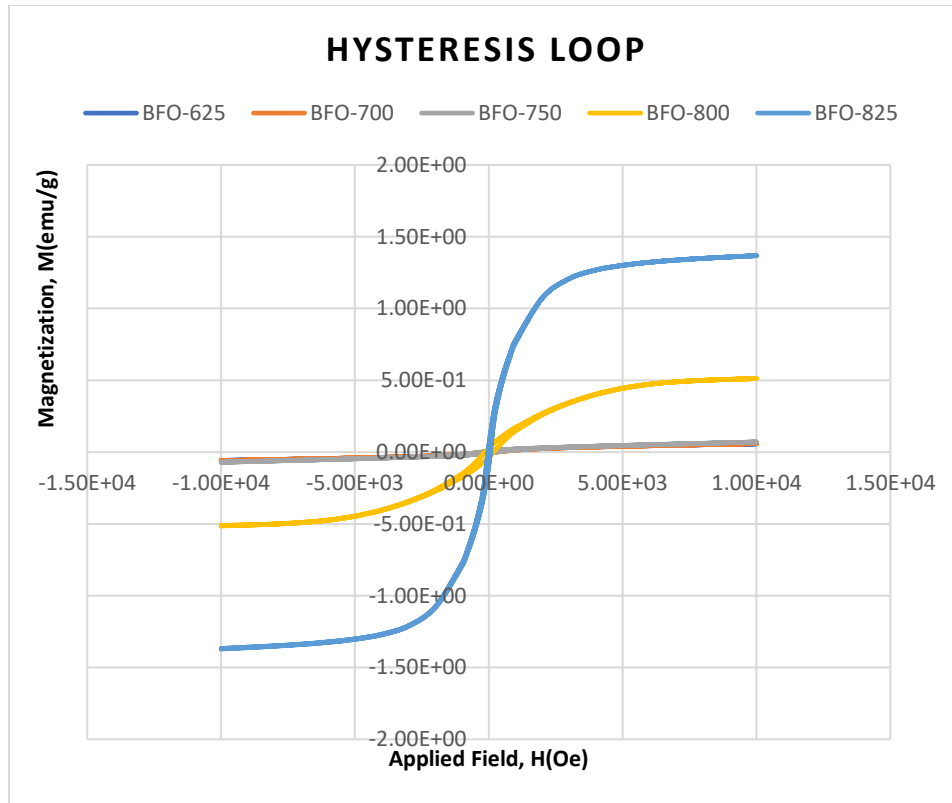


Figure 4-13: Magnetization vs Applied Magnetic Field for BFO-625, BFO-700, BFO-750, BFO-800, BFO-825.

Table 4-4: M-H curve parameters

Sample ID	Average remnant magnetization M_r (emu/g)	Average coercive field H_c (Oe)	Maximum magnetization M_H (emu/g)
BFO-625	0.00639	240.777	0.0579
BFO-700	0.00607	257.608	0.0593
BFO-750	0.00610	220.595	0.0705
BFO-800	0.03161	154.847	0.5125
BFO-825	0.06880	43.678	1.369

A decrease in average coercive field, H_c (Oe) from BFO-700 to BFO-825 is due to sintering temperature effect. From BFO-625 to BFO-825, maximum magnetization, M_H (emu/g) and

remanent magnetization, $M_r(\text{emu/g})$ increase because of the suppressed magnetic spin structure. However, maximum magnetization, $M_H(\text{emu/g})$ and remanent magnetization, $M_r(\text{emu/g})$ in BFO-825 are somewhat higher than the other. It is mentioned that 2nd phase ($\text{Bi}_2\text{Fe}_4\text{O}_9$ and $\text{Bi}_{25}\text{FeO}_{39}$) formed in those samples are iron rich [189]. The highest value of maximum magnetization, $M_H(\text{emu/g})$ in BFO-825 is due to the highest percent 2nd phase formation than other samples. As per table 4-4 it is clearly seen that in BFO-800 $M_H(\text{emu/g})$ was increased about 7 orders in value than BFO-750. These abrupt changes were also seen in average remanent magnetization, $M_r(\text{emu/g})$ as well as in average coercive field, $H_c(\text{Oe})$.

The unique spatial modulation structure of BFO makes it only exhibit very weak or does not exhibit macroscopic magnetism [198]. However, when the grain size is below ~ 62 nm which is the spin cycle of spatial modulation structure, the macroscopic magnetism of BFO will enhance. Since the grains of the SPS-prepared sample are finer than those of the conventionally synthesized one, the macroscopic magnetism of the former could be somewhat stronger.

The promising magnetic properties achieved in the present investigation could be associated with the high-density and fine and uniform microstructure created by SPS along with high-energy ball milling.

4.6. Optical Properties Measurements

4.6.1. FT-IR Analysis

Infrared frequencies correspond to vibrational modes in specific chemical bonds. The stronger the bond, the higher the frequency (shorter the wavelength, higher the energy) the atoms vibrate at. IR absorption occurs when the incoming light frequency matches the vibrational frequency of the bond. This gives chemists a powerful tool, enabling us to identify specific functional groups in molecules in the sample.

Light can be detected either through transmission - the amount of light that passes through the sample - or by reflection - the amount of light that bounces off the sample. Each detection mode has its benefits.

High transmittance at a frequency means there are few bonds to absorb that "color" light in the sample, low transmittance means there is a high population of bonds which have vibrational energies corresponding to the incident light.

Figure 4-14 shows the FT-IR spectra obtained from BFO-Calcined powder and SPS sintered at different temperatures. In all samples characteristic absorption peaks were observed. In BFO-625 and BFO-825 absorption peaks formed at $\sim 634 \text{ cm}^{-1}$, $\sim 848 \text{ cm}^{-1}$ and $\sim 1080 \text{ cm}^{-1}$. Absorption peak

at $\sim 634\text{ cm}^{-1}$ is characteristic to Fe-O stretching. On the other hand, absorption peaks at $\sim 848\text{ cm}^{-1}$ and $\sim 1080\text{ cm}^{-1}$ are characteristic to bending vibrations of octahedral FeO_6 groups in the perovskite compounds [154].

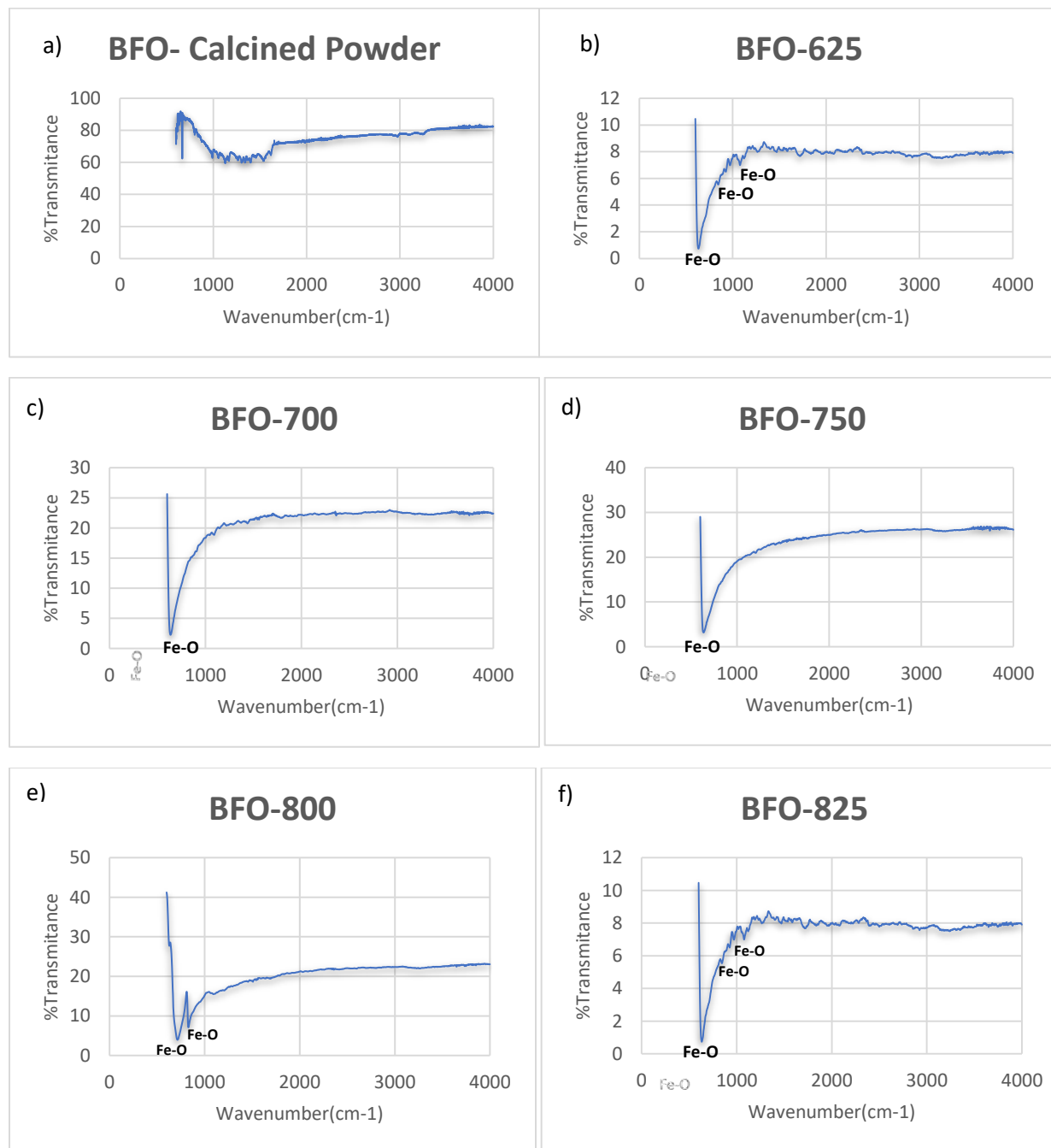


Figure 4-14: Fourier transform infrared (FT-IR) spectrum of Bismuth Ferrite a) BFO-Calcined powder, b) BFO-625, c) BFO-700, d) BFO-750, e) BFO-800, f) BFO-825.

In BFO-700 and BFO-750 absorption peaks appeared at $\sim 640\text{ cm}^{-1}$ and $\sim 634\text{ cm}^{-1}$ respectively which are characteristic to Fe-O stretching. However, in BFO-800 two absorption peaks appeared at $\sim 718\text{ cm}^{-1}$ and $\sim 830\text{ cm}^{-1}$ which characteristic to Fe-O stretching and bending vibrations of octahedral FeO_6 groups in the perovskite compounds. The Fe-O stretching peak of BFO-700 ($\sim 640\text{ cm}^{-1}$) and BFO-800 ($\sim 718\text{ cm}^{-1}$) showed a shift in comparison to BFO-625 ($\sim 634\text{ cm}^{-1}$), BFO-750 ($\sim 634\text{ cm}^{-1}$) and BFO-825 ($\sim 634\text{ cm}^{-1}$).

Two new bending vibration peaks formed in BFO-625 and BFO-825 at $\sim 1080\text{ cm}^{-1}$ with respect to other samples. The Fe-O bending vibration peak of BFO-625 and BFO-825 ($\sim 848\text{ cm}^{-1}$) showed a shift in comparison to the BFO-800 (and $\sim 830\text{ cm}^{-1}$). The shift of the bending vibrations of Fe-O bond towards higher frequency may be due to the disturbance occurring in the bonds and eventually results in the creation of oxygen deficiencies in the sample [154,191]. This result can be corroborated with the defects associated with size mediated weak ferromagnetic behavior.

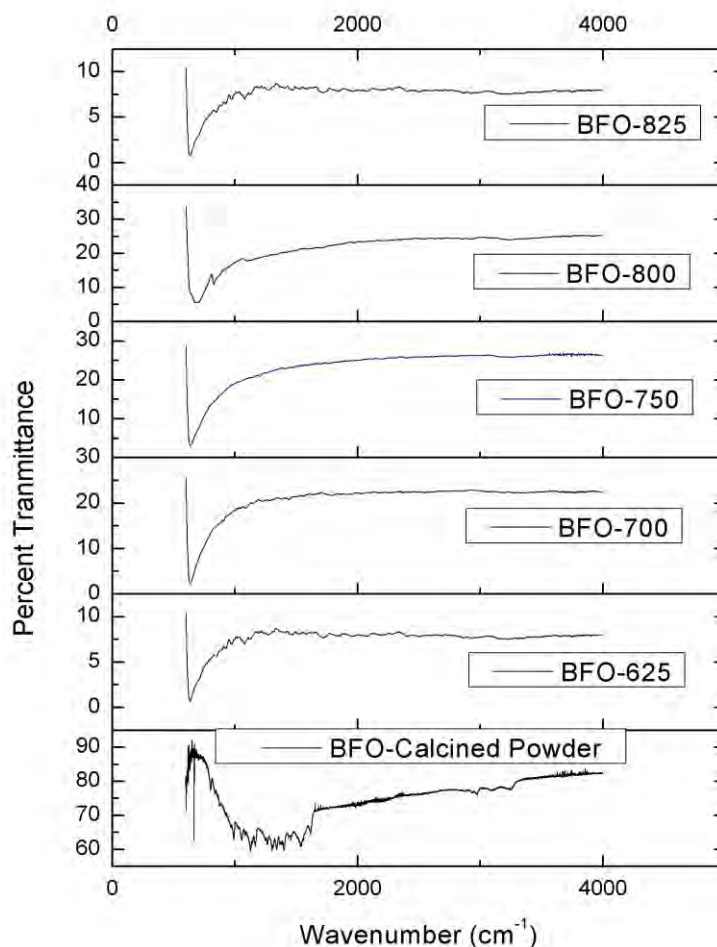


Figure 4-15: Combined Fourier transform infrared (FT-IR) spectrum of Bismuth Ferrite (BFO-Calcined powder, BFO-625, BFO-700, BFO-750, BFO-800, BFO-825).

Figure 4-15 shows the combined Fourier transform infrared (FT-IR) spectrum of all BFO samples. In BFO-625 it is seen that %Transmittance showed consistency over a range of wavenumber 1144-4000 cm^{-1} but value is lower about 8. Interestingly, %Transmittance increased gradually by raising SPS temperature up to 750 and then it reduced its value in descending order. %Transmittance for BFO-825 was regained its value exactly same as the value obtained in BFO-625 in a same range of wavenumber.

In BFO-700 %Transmittance showed consistency about 18.9-22.45 from wavenumber 1084-4000 cm^{-1} . The highest %Transmittance was achieved in BFO-750 that was about 20-26.5 from wavenumber 1100-4000 cm^{-1} . In BFO-800 %Transmittance decreased slightly in a similar way slightly increased in BFO-750 from BFO-700. So, obtained %Transmittance in BFO-800 was about 20-23 from wavenumber 2000-4000 cm^{-1} . Initial range of wavenumber was somewhat higher in BFO-800 sample than the rest of the samples.

Comparatively higher % Transmittance shows its consistency over a long-range wavenumber was obtained in BFO-750 sample. Transmittance 26.5% means that only 26.5% of the incoming light is detected on the other side of the sample. It can be due to either high absorption or scattering of the sample. Both phenomena affect the transmitted beam. In addition, thicker the sample, less light is coming through, according to Beer's law:

$$I = I_0 \cdot \exp(-\beta \cdot d)$$

Where, β is the transmissivity;

D is the path length;

I_0 is original light intensity

I is transmitted light intensity

High transmittance at a frequency means there are few bonds to absorb that "color" light in the BFO-750 sample. As it absorbs color light it can be used as an optical fiber. This infrared response can be the thriving brand-new invention like infrared filter in the study optical properties.

4.6.2. Raman Analysis

Actually, there is two modes (A_1, E) studied in Bismuth Ferrite ceramics. These labels refer to the representation of the molecular point group. The vibrational ground state always transforms as A_1 and the excited state with one vibrational quantum transforms as some representation of the molecular symmetry group, e.g. E_1 .

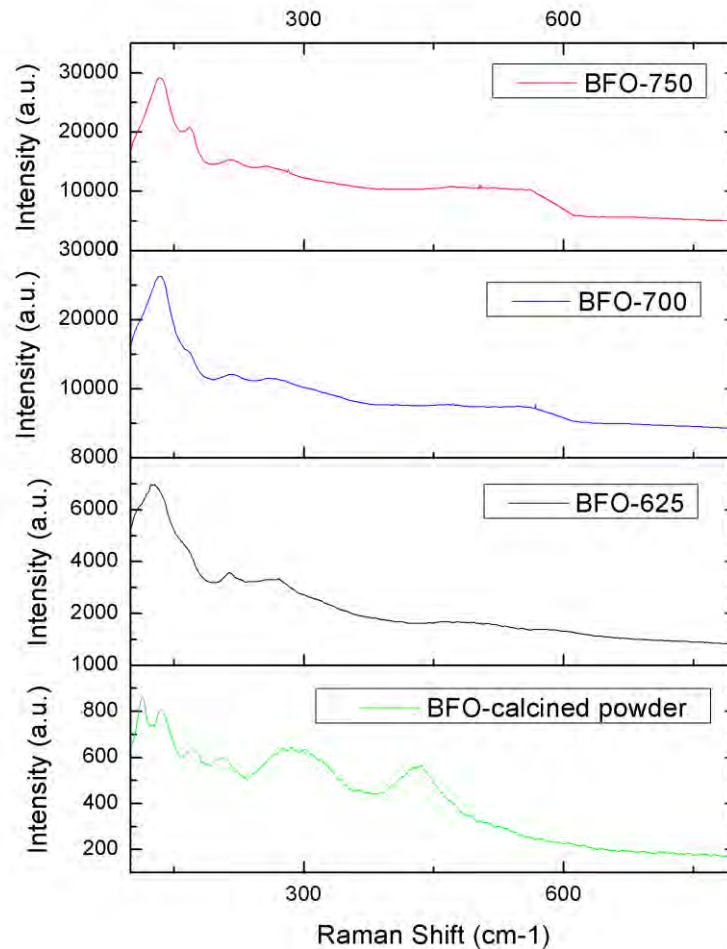


Figure 4-16: Raman Spectra of BFO-Calcined powder and SPS sintered samples (BFO-625, BFO-700, BFO-750).

Then the excitation of one quantum of this vibration corresponds to an energy difference $\Delta E = E_{E_1} - E_{A_1} = h\nu$; $\Delta E = E_{E_1} - E_{A_1} = h\nu$ where, ν is the wavenumber of the Raman transition. BFO-calcined powder quality and Pellet quality was also tested by Raman spectroscopy for each composition, Figure 4-16.

The characteristic lines of rhombohedral R3c BiFeO₃ are clearly observed. According to group theory analysis by several authors [179-184], the R3c structured BFO permits 13 Raman active phonons that can be summarized by the irreducible representation:

$$\Gamma = 4A_1 + 9E \quad [179-184].$$

- Strong scattering intensities A₁-1(140 cm⁻¹), A₁-2(172 cm⁻¹), A₁-3(220 cm⁻¹)
- Weak scattering intensities A₁-4(427 cm⁻¹)
- Medium scattering intensities E-1(75 cm⁻¹), E-2(265 cm⁻¹), E-3(275 cm⁻¹), E-4(345 cm⁻¹), E-5(370 cm⁻¹), E-6(470 cm⁻¹), E-7(525 cm⁻¹), E-8(540 cm⁻¹) or E-9(603 cm⁻¹)

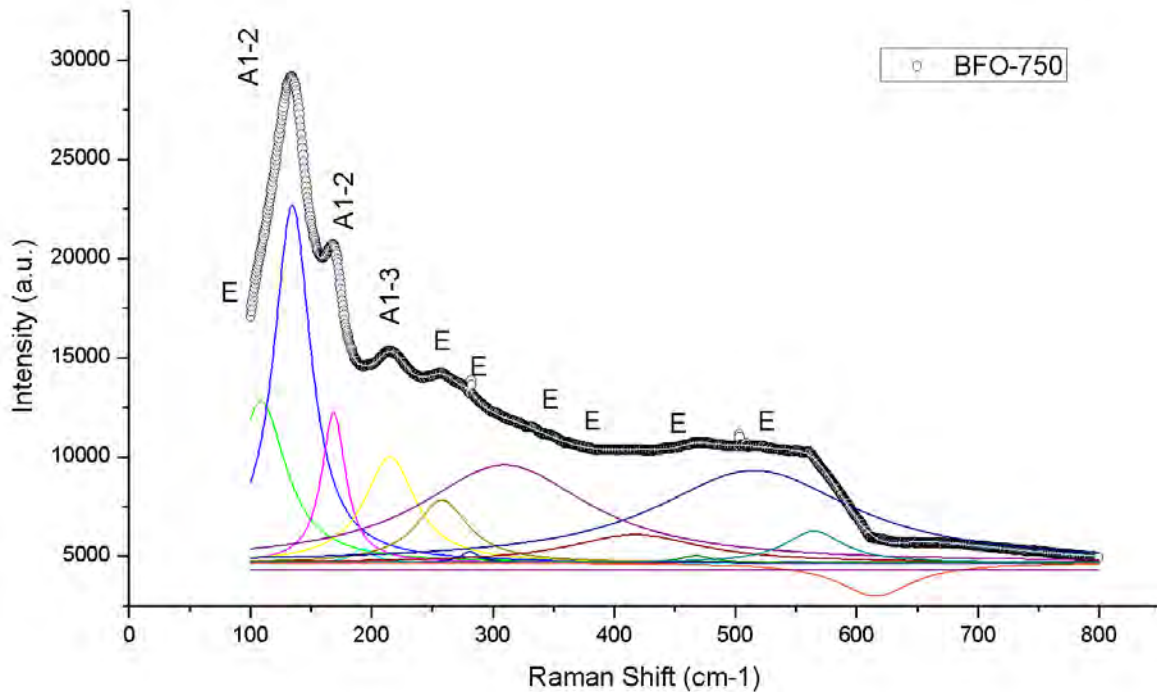


Figure 4-17: Room Temperature Raman Spectra of BFO-750. Multi-peaks fitting shows Raman modes at different Raman shift.

The Raman spectra measured at room temperature was showed in the figure 4-17. As assigned in the spectrum, three A₁ modes (135.37, 171.8, 217.7 cm⁻¹) and seven E modes (75, 261.85, 278, 346.3, 374.1, 477.2, and 524.5 cm⁻¹) can be clearly detected in BFO-750 sample. Similar modes can also be detected in all samples. There is no obvious peak shifting between the spectra. Bands at low Raman shift, associated with the Bi-O bonds.

4.7. Electrical Properties Measurements

4.7.1. Piezoelectric Measurements

Bismuth ferrite is a piezoelectric material. It is very natural to have piezoelectricity in BFO. In Bismuth Ferrite, the rhombohedral phase is characterized by a lack of the inversion center and is piezoelectrically active. It has been already mentioned that the polar displacement of bismuth ions along (001) direction of the rhombohedral cell gives the largest contribution to the piezoelectric response [155], whereas the calculated ion coordinates allow this displacement to be evaluated. Previous studies from Shvartsman et al. it is seen that Piezoelectric d_{33} constant of Bismuth Ferrite sample was 50-70 pC/N.[193]

Before subjecting the material to an external stress, the centers of the negative and positive charges of each molecule coincide—resulting into an electrically neutral molecule. However, in presence of an external mechanical stress the internal reticular can be deformed, thus causing the separation of the positive and negative centers of the molecule and generating little dipoles. As a result, the opposite facing poles inside the material cancel each other and fixed charges appear on the surface. That is to say, the material is polarized. This polarization generates an electric field that can be used to transform the mechanical energy, used in the material's deformation, into electrical energy.

Table 4-5: Piezoelectric d_{33} constant (pC/N) of BFO-750 sintered sample

+ve	-ve
2.0	-2.1
2.6	-2.9
2.5	-2.5
1.6	-1.8
2.5	-2.3
2.2	-1.9

Table 4-5 listed the Piezoelectric d_{33} constant (pC/N) of BFO-750 sintered sample. It was seen that d_{33} constant of this sample showed highest positive charge + 2.6 and highest negative charge -

2.9 without poling the sample. Moreover, the average positive charge was about + 2.23 on the positive side of the sample and the average negative charge was about -2.25 on the opposite side/negative side of the sample. Piezoelectric d_{33} constant (pC/N) on the both sides of the sample were nearly equal.

The average d_{33} coefficient for BFO-750 was 2.242 ± 0.65 pCN⁻¹. The largest d_{33} coefficient measured for BFO-750 was 2.9 ± 0.3 pCN⁻¹.

Two samples were prepared at 800°C with a little change for the measurement of Piezoelectric d_{33} constant (pC/N). Those two samples were named as 800(A) and 800(B). Piezoelectric d_{33} constant (pC/N) of both samples were listed in the table 4-7 and table 4-6 respectively. Stupendous d_{33} constant was obtained in BFO-800(B) without poling which is listed in the table 4-6.

Table 4-6: Piezoelectric d_{33} constant (pC/N) of BFO-800(B)

+ve	-ve
6.8	-6.6
5.3	-5.7
6.4	-5.8
7.1	-6.7
5.6	-6.0
7.2	-6.6

It implies that that d_{33} constant of this sample showed highest positive charge + 7.2 and highest negative charge -6.7 without poling the sample. Moreover, the average positive charge was about + 6.4 on the positive side of the sample and the average negative charge was about -6.23 on the opposite side/negative side of the sample. Piezoelectric d_{33} constant (pC/N) on the both sides of the sample were almost equal.

The average d_{33} coefficient for BFO-800(B) was 6.32 ± 1.1 pCN⁻¹. The largest d_{33} coefficient measured for BFO-800(B) was 7.2 ± 0.5 pCN⁻¹.

On the other hand, it was obtained about 15 orders lower piezoelectric d_{33} constant (pC/N) in BFO-800(A) sample than BFO-800(B). It was seen that d_{33} constant of this sample showed highest positive charge + 0.5 and highest negative charge -0.5 without poling the sample. Moreover, the average positive charge was about + 0.433 on the positive side of the sample and the average negative charge was about -0.45 on the opposite side/negative side of the sample. Piezoelectric d_{33} constant (pC/N) on the both sides of the sample were nearly equal.

Table 4-7: Piezoelectric d_{33} constant (pC/N) of BFO-800(A)

+ve	-ve
0.5	-0.4
0.4	-0.4
0.4	-0.4
0.4	-0.5
0.5	-0.5
0.4	-0.5

The average d_{33} coefficient for BFO-800(A) was $0.442 \pm 0.067 \text{ pCN}^{-1}$. The largest d_{33} coefficient measured for BFO-800(A) was $0.5 \pm 0.1 \text{ pCN}^{-1}$.

It was polled one of BFO samples that was BFO-800(A). Poling temperature, applied voltage and holding time were 130°C , 2000V and 30 minutes respectively. In that case d_{33} constant decreased after poling. As the thickness of the sample 1.378 mm was a bit thicker so it wasn't possible to get exact orientation after poling. That's maybe a possible reason to the reduction of the d_{33} constant after the poling. To get appropriate result after poling *Corona Poling system* will be the best suited for the measurement of the d_{33} constant. Table 4-8 was listed Piezoelectric d_{33} constant (pC/N) of BFO-800(A) sample.

Table 4-8: Piezoelectric d_{33} constant (pC/N) of BFO-800(A) sample after poling.

+ve	-ve
0.2	-0.2
0.3	-0.2
0.2	-0.2
0.2	-0.2
0.2	-0.2
0.3	-0.2

It was seen that d_{33} constant of this sample after poling showed highest positive charge + 0.3 and highest negative charge -0.2. Moreover, the average positive charge was about + 0.233 on the positive side of the sample and the average negative charge was about -0.2 on the opposite side/negative side of the sample. Piezoelectric d_{33} constant (pC/N) on the both sides of the sample were nearly equal.

The average d_{33} coefficient for BFO-800(A) was $0.217 \pm 0.067 \text{ pCN}^{-1}$ after poling. The largest d_{33} coefficient measured for BFO-800(A) was $0.3 \pm 0.1 \text{ pCN}^{-1}$ after poling.

Table 4-9: Piezoelectric d_{33} constant (pC/N) of BFO-825

+ve	-ve
0.3	-0.2
0.2	-0.3
0.2	-0.2
0.2	-0.3
0.3	-0.2
0.3	-0.2

Table 4-9 listed the Piezoelectric d_{33} constant (pC/N) of BFO-825 sintered sample. It was seen that d_{33} constant of this sample showed highest positive charge + 0.3 and highest negative charge -

0.3 without poling the sample. Moreover, the average positive charge was about + 0.25 on the positive side of the sample and the average negative charge was about -0.233 on the opposite side/negative side of the sample. Piezoelectric d_{33} constant (pC/N) on the both sides of the sample were nearly equal.

The average d_{33} coefficient for BFO-825 was 0.242 ± 0.067 pCN⁻¹. The largest d_{33} coefficient measured for BFO-825 was 0.3 ± 0.1 pCN⁻¹.

It was discerned that wayward results between BFO-800(A) and BFO-800(B). It is difficult to predict the exact reasons behinds this. Suspected potential may be due to the following which are listed as following-

- i) Same pressure (50MPa) was applied on these both samples at a different heating range. In BFO-800(A) and BFO-800(B) pressure applied in the temperature range between 244-280°C and 323-340°C respectively. Pressure released in the temperature range between 700-620°C and 700-600°C in the BFO-800(A) and BFO-800(B) samples respectively. As pressure is directly related to the orientation/spin of plane/atom. So, they might have different orientation in the infant state.
- ii) 2ndary phases form in the BFO-800(B) sample was comparatively higher than that of BFO-800(A). As more 2nd phases mean more stressed developed in the crystal structure which is directly responsible for piezo response of a material.

Unfortunately, it wasn't able to find any phenomenal Piezoelectric d_{33} constant (pC/N) in BFO-625 and BFO-700 samples.

4.7.2. Ferro-electric Loop Test

In order to find out the ferroelectric nature of the compounds, polarization vs. electric field (P-E) curves was measured, as shown in figure 4-18, 4-19 and 4-20. P-E loops of the BFO-625, BFO-700, BFO-750, BFO-800 and BFO-825 ceramics were taken at a frequency of 100 Hz and an applied field of 5 kVcm⁻¹ and 10 kVcm⁻¹.

The loops are relatively saturated, indicating that the samples have good ferroelectricity. Usually, it is difficult to obtain a saturated ferroelectric hysteresis loop for BFO because of the leakage current effect caused by impurity phases and other defects. To attain a relatively saturated loop the quality of the prepared material might be good enough. In this work, the high-quality BFO ceramics prepared by SPS along with high-energy ball milling could be responsible for the well-

shaped loops. Normally, it is desirable for the BFO to have large saturation (or maximum) polarization (P_s) and remanent polarization (P_r) but small coercivity (E_c). In the present case, the P_s , P_r and E_c are apparently larger for the samples BFO-625, BFO-700 and BFO-750 at 10 KV than 5 KV. It is seen that the maximum value of P_s , P_r and E_c obtained at BFO-750 sample amongst all samples.



Figure 4-18: P-E curve for BFO-625 and BFO-700 at voltage 5 kV and 10 kV.

As reported by Prasad, [198] the P_r of nanocrystalline BFO ceramics prepared by microwave sintering along with high-energy ball milling was about 0.5 $\mu\text{C}/\text{cm}^2$. Sharma et al. [200] prepared pure BFO ceramics by sol-gel + conventional sintering and obtained that the P_s and P_r were about

8.5 and 2.0 $\mu\text{C}/\text{cm}^2$. Maurya et al. [33] synthesized BFO ceramics by high-energy ball milling + conventional sintering, obtaining that the P_s and P_r were approximately 2.5 and 0.5 $\mu\text{C}/\text{cm}^2$. Clearly, the values in the present work are well comparable with those previous values.

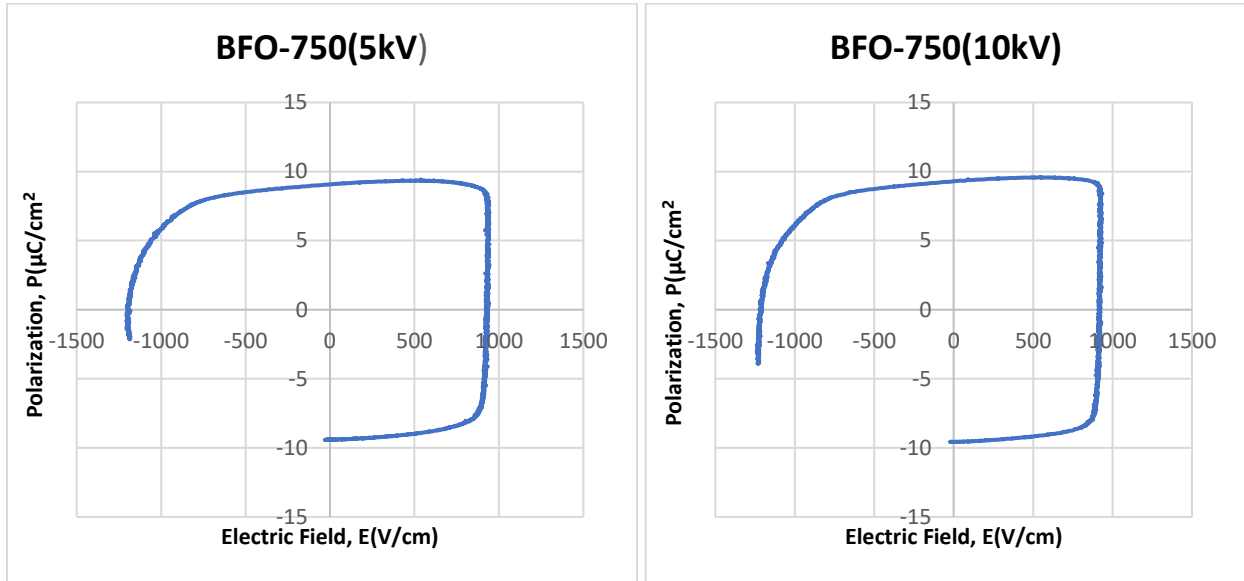


Figure 4-19: P-E curve for BFO-750 at voltage 5 kV and 10 kV.

The conventional furnace sintering (CFS) sample could not withstand application of higher electric fields (>10 kV/cm). Significantly higher values of the breakdown fields in the SPS samples indicate lower leakage currents. The higher coercive field could be attributed to its larger grains, because a switching of ferroelectric domains is more difficult inside a large grain than in small one [201].

A less roundish shape of the hysteresis loop confirms that a leakage current is lower in the SPS sample, which is interesting as it contains slightly higher amount of the secondary phases. Even more importantly, the SPS samples can also contain higher concentration of oxygen vacancies that contributes to low resistance of the sample due to the reduction atmosphere during sintering. Obviously, some other features, such as Fe^{2+} ions concentration should be considered, since electron hopping between Fe^{2+} and Fe^{3+} can increase leakage current, too [202]. In this work obtained results are in good agreement with previous findings published by Dai et al. [202] who reported that sintering in nitrogen provided better ferroelectric properties for the samples than sintering in the air. They achieved the poorest ferroelectric properties in the samples

sintered in oxygen and explained their findings by a decrease in Fe^{2+} fraction, good crystallinity and better microstructure of the samples sintered in nitrogen and air.

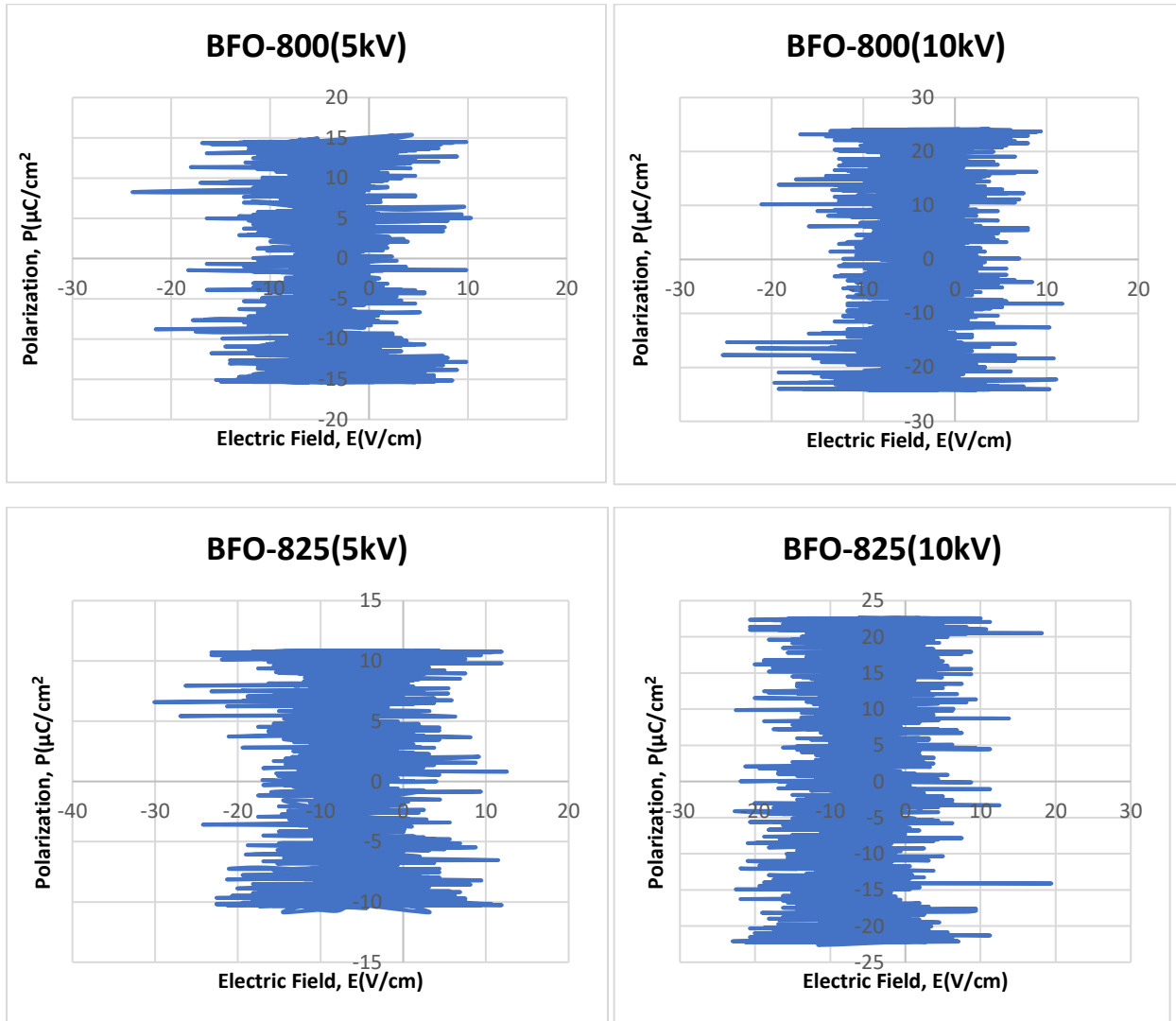


Figure 4-20: P-E curve for BFO-800 and BFO-825 at voltage 5 kV and 10 kV.

In BFO-800 and BFO-825 it is seen that at both 5 kV and 10 kV there is noise in P-E loop. However, it showed the same consequence even with lower frequency as well as lower applied voltage.

Chapter 5: Conclusions and Future Work

A conclusion will be drawn from the experimental results which are novel to this field of study in the conclusion section. Some recommendations will be also enlisted on some future work proposals section.

5.1. Summary of the key Findings

The objective of the thesis is to find out optimum spark plasma sintering condition and this research work is also designed to understand the hierarchy of optical response in BFO crystal.

The main findings of the study are:

- The structure of bismuth ferrite was determined. The structure of BFO was distorted perovskite (rhombohedral) with space group R3c.
- XRD analysis showed that 2nd phases ($\text{Bi}_{25}\text{FeO}_{39}$ and $\text{Bi}_2\text{Fe}_4\text{O}_9$) started to form at 700°C and a tiny amount of phase formed in BFO-750 than BFO-800 and BFO-825.
- Density measurement showed that the densest sample was BFO-750. It was not possible to obtain the exact density of BFO-625 and BFO-825 samples due to the insufficient holding time and somewhat higher spark plasma sintering temperature respectively.
- Optical microscopy assured that there were grains and grain boundaries appeared after thermal etching in BFO-800.
- Scanning Electron Microscopy revealed that the SPS-prepared samples exhibited uniform microstructures and their average grain sizes increased gradually with increasing sintering temperature, but they were smaller than ~220 nm up to temperature 750 °C. BFO-750 was the densest product that would show optimum properties than rest of the samples which has minimum porosity.

- The EDS results clearly ensured the presence of essential elements for the successful synthesis of the SPS BFO-based material.
- As per VSM study magnetic measurement showed that the promising magnetic properties achieved in the present investigation could be associated with the high-density fine and uniform microstructure created by SPS along with high-energy ball milling.
- FT-IR spectroscopy revealed that bismuth ferrite showed good infrared response. The maximum %transmittance obtained over a long-range wavenumber in BFO-750. This material will be best suited for the application of optical fiber (infrared filter) for its laudable infrared response.
- Raman spectroscopy confirmed that there were maximum 13 modes formed in BFO-750. In the spectrum, three A₁ modes (135.37, 171.8, 217.7 cm⁻¹) and seven E modes (75, 261.85, 278, 346.3, 374.1, 477.2, and 524.5 cm⁻¹) were clearly detected in BFO-750 sample. Similar modes can also be detected in all samples.
- The direct piezoelectric effect was measured in BFO-750, BFO-800 and BFO-825 using a quasi-static method based on the Berlincourt method. BFO-800 showed the stunning results without poling.
- From Ferroelectric loop study, it was revealed that the loops are relatively saturated, indicating that the samples have good ferroelectricity except BFO-800 and BFO-825 samples. It was seen that the value of P_s, P_r and E_c obtained at BFO-750 sample amongst all samples were maximum.

5.2. Answers to the Research Questions

Research question 1: *How do spark plasma sintering parameters effect the properties of the bismuth ferrite ceramic?*

Yes. In Spark Plasma Sintering parameters have the paramount effect on the properties of Bismuth Ferrite materials. In this thesis, it has been changed only one parameter by fixing other parameters. In the present work, spark plasma sintering temperature was directly affected structural, optical and electrical properties of Bismuth Ferrite (BiFeO_3).

Research question 2: *What are the optical properties of bismuth ferrite ceramic? Should bismuth ferrite exhibit infrared response?*

Among useful ferroelectrics for photoinduced applications, the so-called multiferroic BiFeO_3 (BFO) is the most promising candidate because of its relatively small band gap ($E_g \approx 2.6 - 2.8$ eV) in comparison to other classical ferroelectric oxides like BaTiO_3 , PbZrTiO_3 , or LiNbO_3 ($E_g > 3$ eV), allowing one to benefit from a wider part of the sunlight spectrum and its larger polarization value ($P \approx 100 \mu\text{C}/\text{cm}^2$), ensuring a more efficient separation of the photogenerated charge carriers. Due to have its small band gap BFO can be promising in photovoltaic, phototransduction, or photocatalytic characteristics.

Yes, BFO showed infrared response. It showed highest 13 Raman active modes and maximum %transmittance was about 27 in pure condition.

Research question 3: *Should bismuth ferrite exhibit piezoelectric effect?*

Bismuth ferrite is a strong piezoelectric material. So, it should show piezoelectric effect. In the recent work piezoelectricity was obtained without poling the sample. The rhombohedral phase is characterized by a lack of the inversion center and is piezoelectrically active. The polar displacement of bismuth ions along (001) direction of the rhombohedral cell gives the largest contribution to the piezoelectric response.

Research question 4: *Should bismuth ferrite demonstrate ferromagnetism, ferroelectricity and pyroelectricity?*

Polar crystals of bismuth ferrite should show ferroelectricity and pyroelectricity. Ferroelectricity can also occur due to the existence of lone pairs of electrons on the outer shell of the A-site atom, which are highly susceptible to polarization. This is the cause of ferroelectricity in BiFeO_3 .

BiFeO₃ has a rhombohedrally distorted perovskite structure having G-type antiferromagnetic ordering and A-site polarization. Each Fe³⁺ spin is surrounded by six nearly antiparallel spin on the nearest oxygen atoms. As Goldschmidt Tolerance Factor is 0.88 buckling (of FeO₆ octahedra) occurs. As a consequence of the oxygen octahedral distortion, directly related with the Fe-O-Fe angle, BiFeO₃ structure presents spin canting which results in a weak magnetic moment. This net magnetic moment exhibits a long-range superstructure consisting on a spin cycloid with a 64-nm wavelength that is incommensurable with the crystallographic structure.

5.3. Testing of the Research Hypotheses

Based on the results presented in this thesis, the research hypothesis can be tested and evaluated as follows:

Hypothesis 1: *Structural changes should have impact on infrared response, piezoelectric and magnetic response.*

This hypothesis has been proven right. In this work, it is seen that lattice parameter changed with the sintering temperature by inducing 2nd phases with higher temperature. These 2nd phases are bismuth and iron rich. Increasing 2nd phases mean increasing development of stress inside the crystal structure. As stresses raises distortion inside rhombohedrally distorted perovskite BiFeO₃ structure also increases. These structural changes are the pioneer of the optical and piezoelectric response of BFO. Again Fe³⁺ has d-orbital which is responsible for optical and polar transition inside the BFO structure.

Hypothesis 2: Sintering temperature is directly related to the % transmittance with a range of wavenumber.

In this work it is investigated that % transmittance increased with increasing sintering temperature and then again decreased. As, sintering temperature is responsible for the densification of BFO. The optimum properties like % transmittance, piezoelectricity and so on will be shown by the higher the denser sample. During sintering pressure applied/released in a range of temperature also plays an imperative role during the densification process.

5.4. Future Work

Future work will be engrossed in optimizing modification/ co-modification either A or B site or both sites to get best electrical, optical and magnetic properties. Thus, the potential for future studies in this area is enormous. On the basis of the present study, the following future work are suggested:

- a) **Modification or co-modification in BFO sample followed by spark plasma sintering-** This modification/co-modification can be done by doping rare earth lanthanide ions (La^{3+} , Nd^{3+} , Gd^{3+} , Ho^{3+} or Sm^{3+}) or divalent ions (Ca^{2+} , Sr^{2+} , Ba^{2+} , Pb^{2+}) at the A site of BFO for substituting part of Bi^{3+} or with ions of Nb^{5+} , Mn^{4+} , Cr^{3+} , Ti^{4+} , Ga^{3+} , Ta^{5+} at the B site for substituting part of Fe^{3+} .
- b) **SPS of Solid Solution-** Fabricating a solid solution of BFO with other ABO_3 perovskite materials, such as BaTiO_3 .
- c) **Synthesis of BFO nano-particle by SPS-** Synthesizing BiFeO_3 nano-particles with grain size below 62 nm to achieve ferromagnetism by destroying spiral spin structure can be applied to SPS sintered BFO sample.
- d) **SPS of BiFeO_3 -PZT to get large piezoelectricity-** This is important because MPBs are commonly thought to be the key behind the large piezoelectric coefficients of PZT and relaxors, so the MPB of BiFeO_3 -PT might lead to equally large piezoelectric constants.

References

- [1] H. Singh and K. L. Yadav, "Dielectric, magnetic and magnetoelectric properties of La and Nb codoped bismuth ferrite," *Journal of Physics: Condensed Matter*, Vol. 23, 2011, pp. 385901:1-6.
- [2] Z. M. Tian, S. L. Yuan, X. L. Wang, X. F. Zheng, S. Y. Yin, C. H. Wang and L. Liu, "Size effect on magnetic and ferroelectric properties in $\text{Bi}_2\text{Fe}_4\text{O}_9$ multiferroic ceramics," *Journal of Applied Physics*, Vol. 106, 2009, pp. 103912: 1-4.
- [3] Y. Lin, Q. Jiang, Y. Wang, C. Nan, L. Chen, and J. Yu, "Enhancement of ferromagnetic properties in BiFeO_3 polycrystalline ceramic by La doping," *Applied Physics Letters*, Vol. 90, 2007, pp. 172507:1-3.
- [4] S. Cheong and M. Mostovoy, "Multiferroics: a magnetic twist for ferroelectricity," *Nature Materials*, Vol.6, 2007, pp. 13-20.
- [5] N. A. Hill, "Why are there so few magnetic ferroelectrics?," *Journal of Physical Chemistry B*, Vol. 104, 2000, pp. 6694–6709.
- [6] Y. F. Cui, Y. G. Zhao, L. B. Luo, J. J. Yang, H. Chang, M. H. Zhu, D. Xie, and T. L. Ren, "Dielectric, magnetic, and magnetoelectric properties of La and Ti codoped BiFeO_3 ," *Applied Physics Letters*, Vol. 97,2010, pp. 222904: 1-3.
- [7] A.K. Ghosh, H. Kevin, B. Chatterjee, G.D. Dwivedi, A. Barman, H.D. Yang and S. Chatterjee, "Effect of Sr-doping on multiferroic properties of $\text{Bi}_{0.8}\text{La}_{0.2}\text{Fe}_{0.9}\text{Mn}_{0.1}\text{O}_3$," *Solid State Communications*, Vol. 152, Issue 6, 2009, pp. 557-560.
- [8] G. Catala, and J.F. Scott, "Physics and applications of bismuth ferrite," *Advanced Materials*, Vol. 21, 2009, pp. 2463-2485.
- [9] I. Sosnowska, T.P. Neumaier, and E. Steichele, "Spiral magnetic ordering in bismuth ferrite," *Journal of Physics C: Solid State Physics*, Vol. 15, 1982, pp. 4835.
- [10] I. Sosnowska, W. Sch" afer, W. Kockelmann, K.H. Andersen and I.O. Troyanchuk, "Crystal structure and spiral magnetic ordering of BiFeO_3 doped with manganese," *Applied Physics A*, Vol. 74, 2002, pp. s1040-s1042.
- [11] C. Ederer and N.A. Spaldin, "Weak ferromagnetism and magnetoelectric coupling in bismuth ferrite," *Physics Review B*, Vol. 71, 2005, pp. 060401.
- [12] J. Wang, J. B. Neaton, H. Zheng, V. Nagarajan, S. B. Ogale, B. Liu, D. Viehland, V. Vaithyanathan, D. G. Schlom, U. V. Waghmare, N. A. Spaldin, K. M. Rabe, M. Wuttig and R. Ramesh, "Epitaxial BiFeO_3 multiferroic thin film heterostructures," *Science*, Vol. 299, 2003, pp. 1719-1722.

- [13] D. Lebeugle, D. Colson, A. Forget, M. Viret, P. Bonville, J. F. Marucco and S. Fusil, "Very large spontaneous electric polarization in BiFeO₃ single crystals at room temperature and its evolution under cycling fields," *Applied Physics Letters*, Vol. 91, 2007, pp. 022907-022907.
- [14] D. Lebeugle, 'Groupement de Recherche sur les Nouveaux Etats Electroniques de la Matiere: GdR NEEM'; Gif sur Yvette, November 2006.
- [15] R. Lobo, R. L. Moreira, D. Lebeugle and D. Colson, "Infrared phonon dynamics of a multiferroic BiFeO₃ single crystal," *Physics Review B*, Vol. 76, 2007, pp. 172105.
- [16] N. Jeon, D. Rout, I. W. Kim, and S.J. L. Kang, "Enhanced Multiferroic Properties of Single-phase BiFeO₃ Bulk Ceramics by Ho doping," *Applied Physics Letter*, Vol. 98, Issue 7, 2011, pp 072901072903.
- [17] D. Lebeugle, Ph.D. Thesis, Saclay Institute of Matter and Radiation, 2007.
- [18] X. Qi, J. Dho, R. Tomov, M. G. Blamire and J. L. MacManus-Driscoll, "Greatly reduced leakage current and conduction mechanism in aliovalent-ion-doped BiFeO₃," *Applied Physics Letters*, Vol. 86, 2005, pp 062903:1-3.
- [19] D. H. Wang, W. C. Goh, M. Ning, and C. K. Ong, "Effect of Ba doping on magnetic, ferroelectric, and magnetoelectric properties in multiferroic BiFeO₃ at room temperature," *Applied Physics Letters*, Vol. 88, 2006, pp 212907: 1-3.
- [20] Y. Lin, Q. Jiang, Y. Wang, C. Nan, L. Chen, and J. Yu, "Enhancement of ferromagnetic properties in BiFeO₃ polycrystalline ceramic by La doping," *Applied Physics Letters*, Vol. 90, 2007, pp 172507:1-3.
- [21] Y. F. Cui, Y. G. Zhao, L. B. Luo, J. J. Yang, H. Chang, M. H. Zhu, D. Xie, and T. L. Ren, "Dielectric, magnetic, and magnetoelectric properties of La and Ti codoped BiFeO₃," *Applied Physics Letters*, Vol. 97, 2010, pp.222904: 1-3.
- [22] C. Lan, Y. Jiang and S. Yang, "Magnetic properties of La and (La, Zr) doped BiFeO₃ ceramics," *Journal of Material Science*, Vol. 46, 2011, pp 734–738.
- [23] Reetu, A. Agarwal¹, S. Sanghi, Ashima and N. Ahlawat, "Structural transformation and improved dielectric and magnetic properties in Ti-substituted Bi_{0.8}La_{0.2}FeO₃ multiferroics," *Journal of Physics D: Applied Physics*, Vol. 45, 2012, pp 165001:1-9.
- [24] A. K. Ghosh, G. D. Chatterjee, B. Rana, A. Barman, S. Chatterjee and H. D. Yang., "Role of codoping on multiferroic properties at room temperature in BiFeO₃ ceramic", *Solid State Communications*, Vol. 166, 2013, pp 22–26.
- [25] J. Li, K. Liu, J. Xu, L. Wang, L. Bian and F. Xu, "Structure-Dependent Electrical, Optical and magnetic properties of Mn-Doped BiFeO₃ thin films prepared by the sol-gel process", *Journal of Materials Science Research*, Vol. 2, 2013, pp 75.

- [26] Z. Cheng, X. Wang, and S. Dou, "Improved ferroelectric properties in multiferroic BiFeO₃ thin films through La and Nb codoping," *Physical Review B*, Vol. 77, 2008, 092101: pp 1-4.
- [27] L. Zhai, Y. G. Shi, S. L. Tang, L. Y. Lv and Y. W. Dou, "Large magnetic coercive field in Bi_{0.9}La_{0.1}Fe_{0.98}Nb_{0.02}O₃ polycrystalline compound," *Journal of Physics D: Applied Physics* Vol. 42, 2009, pp 165004.
- [28] B. F. Yu, M. Y. Li, J. Liu, D. Y. Guo, L. Pei, X. Z. Zhao, "Enhanced electrical properties in multiferroic BiFeO₃ ceramics co-doped by La³⁺ and V⁵⁺," *Journal of Physics D: Applied Physics*, Vol. 41, 2008, pp. 065003.
- [29] M.S. Bernardo, "Synthesis, microstructure and properties of BiFeO₃-based multiferroic materials: A review", *Bol. Soc. Esp. Ceram. Vidr.*, 53 (2014) 1–14.
- [30] J. Silva, A. Reyes, H. Esparza, H. Camacho, L. Fuentes, "BiFeO₃: A Review on synthesis, doping and crystal structure", *Integr. Ferroelectr.*, 126 [1] (2011) pp. 47–59.
- [31] X. He, L. Gao, "Synthesis of pure phase BiFeO₃ powders in molten alkali metal nitrates", *Ceram. Int.*, 35 [3] (2009) pp. 975–978.
- [32] I. Szafraniak, M. Polomska, B. Hilczer, A. Pietraszko, L. Kepinski, "Characterization of BiFeO₃ nanopowder obtained by mechanochemical synthesis", *J. Eur. Ceram. Soc.*, 27 [13-15] (2011) pp. 4399–4402.
- [33] D. Maurya, H. Thota, K.S. Nalwa, A. Garg, "BiFeO₃ ceramics synthesized by mechanical activation assisted versus conventional solid-state reaction process: A comparative study", *J. Alloys Compd.*, 477 [1-2] (2009) pp. 780–784.
- [34] A. Perejón, N. Murafa, P.E. Sánchez-Jimenez, J.M. Criado, J. Subrt, M.J. Diáñez, L.A. PérezMaqueda, "Direct mechanosynthesis of pure BiFeO₃ perovskite nanoparticles: reaction mechanism", *J. Mater. Chem. C*, 1 [22] (2013) pp. 3551–3562.
- [35] Y.P. Wang, L. Zhou, M.F. Zhang, X.Y. Chen, J.M. Liu, Z.G. Liu, "Room-temperature saturated ferroelectric polarization in BiFeO₃ ceramics synthesized by rapid liquid phase sintering", *Appl. Phys. Lett.*, 84 [10] (2004) pp. 1731–1733.
- [36] W. Cai, C. Fu, W. Hu, G. Chen, X. Deng, "Effects of microwave sintering power on microstructure, dielectric, ferroelectric and magnetic properties of bismuth ferrite ceramics", *J. Alloy Compd.*, 554 (2013) pp. 64–71.
- [37] S.H. Song, Q.S. Zhu, L.Q. Weng, V.R. Mudinepalli, "A comparative study of dielectric, ferroelectric and magnetic properties of BiFeO₃ multiferroic ceramics synthesized by conventional and spark plasma sintering techniques", *J. Eur. Ceram. Soc.*, 35 [1] (2015) pp. 131–138.

- [38] A. Perejón, N. Masó, A.R. West, P.E. Sánchez Jiménez, R. Poyato, J.M. Criado, L.A. Pérez Maqueda, "Electrical properties of stoichiometric BiFeO₃ prepared by mechanosynthesis with either conventional or spark plasma sintering", *J. Am. Ceram. Soc.*, 96 [4] (2013) pp. 1220 -1227.
- [39] A. Perejón, P.E. Sánchez-Jiménez, R. Poyato, N. Masó, A.R. West, J.M. Criado, L.A. Pérez-Maqueda, "Preparation of phase pure, dense fine grained ceramics by conventional and spark plasma sintering of La-substituted BiFeO₃ nanoparticles", *J. Eur. Ceram. Soc.*, 35 [8] (2015) pp. 2283–2293.
- [40] L.C. Wang, Z.-H. Wang, S.L. He, X. Li, P.T. Lin, J.R. Sun, B.G. Shen, "Enhanced magnetization and suppressed current leakage in BiFeO₃ ceramics prepared by spark plasma sintering of sol-gel derived nanoparticles", *Physica B*, 407 [8] (2012) pp. 1196–1202.
- [41] L. E. Cross, "Ferroic Materials and Composites: Pass, Press, and Future" (1997).
- [42] F. Duan and J. Guojun, "Introduction to Condensed Matter Physics," World Scientific (Vol. 1), Singapore, 2005.
- [43] J. M. Yeomans, "Statistical Mechanics of Phase Transitions," Oxford University Press, 2002.
- [44] M. E. Lines and A. M. Glass, "Principles and Applications of Ferroelectrics and Related Materials," Oxford University Press, 2004.
- [45] C. Kittel, "Introduction to solid state physics," American Journal of Physics, Vol. 35, 1967, pp. 547-548.
- [46] E. K. H Salje, "Phase Transitions in Ferroelastic and Co-elastic Crystals," Cambridge University Press, 1990.
- [47] V. Muller, A. Fuith, J. Fousek, H. Warhanek and H. Beige, "Spontaneous strain in ferroelastic incommensurate [N(CH₃)₄]₂CuCl₄ crystals," *Solid State Communications*, Vol. 104, 1997, pp. 455-458.
- [48] L. Jian and C. M. Wayman, "Compressive behavior and domain-related shape memory effect in LaNbO₄ ceramics," *Materials Letters*, Vol. 26, 1996, pp 1-7.
- [49] R. E. Newnham, "Molecular mechanisms in smart materials," *MRS Bulletin*, Vol. 22, 1997, pp. 2034.
- [50] Van E. Wood, A. E. Austin, "Magnetolectric interaction phenomena in crystals," edited by A. J. Freeman and H. Schmid, Gordon and Breach Science Publishers, 1975.
- [51] G. A. Smolenskii and I. E. Chupis, "Ferroelectromagnets," *Soviet Physics Uspekhi*, Vol. 25, 1982, pp475.

- [52] D.I. Khomskii, "Multiferroics: different ways to combine magnetism and ferroelectricity," *Journal of Magnetism and Magnetic Materials*, Vol. 306, 2006, pp 1-8.
- [53] M. Fiebig, "Revival of the magnetoelectric effect," *Journal of Physics D: Applied Physics*, Vol 38, 2005, pp. R123.
- [54] W. Eerenstein, N. D. Mathur, and J. F. Scott, "Multiferroic and magnetoelectric materials," *Nature*, Vol. 442, 2006, pp 759.
- [55] J. P. Velev, S. S. Jaswal, and E. Y. Tsymbal, "Multi-ferroic and magnetoelectric materials and interfaces," *Philosophical Transactions of the Royal Society A: Mathematical, Physical and Engineering Sciences*, Vol. 369, 2011, pp 3069.
- [56] W. Prellier, M. Singh, P. Murugavel, "The single-phase multiferroic oxides: from bulk to thin film," *Journal of Physics: Condensed Matter*, Vol. 17, 2005, pp. R803.
- [57] Y. Tokura and N. Kida, "Dynamical magnetoelectric effects in multiferroic oxides," *Philosophical Transactions of the Royal Society A: Mathematical, Physical and Engineering Sciences*, Vol. 369, 2011, pp. 3679-3694.
- [58] G. Lawes and G. Srinivasan, "Introduction to magnetoelectric coupling and multiferroic films," *Journal of Physics D: Applied Physics*, Vol. 44, 2011, pp. 243001.
- [59] M. Fieberg, "Revival of the magnetoelectric effect", *Journal of Physics D: Applied Physics*, Vol. 38, 2005, pp. R123.
- [60] W. Ehrenstein, N. Mazur, J. Scott, "Multiferroic and magnetoelectric materials", *Nature*, Vol. 442, 2006, pp. 759.
- [61] R. Ramesh, N.A. Spaldin, "Multiferroics: progress and prospects in thin films", *Nature Materials*, Vol. 6, 2007, pp. 21-29.
- [62] Special issue, *Journal of Physics: Condensed Matter*, Vol. 20, 2008, pp. 434201-434220.
- [63] D.I.Khomskii, "Magnetism and ferroelectricity: why do they so seldom coexist?," *Bulletin of American Physical Society C*, Vol. 1, 2001, pp. 21002.
- [64] B. B. Van. Aken, T. T. M. Palstra, A. Filippetti, and N. A. Spaldin, "The origin of ferroelectricity in magnetoelectric YMnO_3 ", *Nature Materials*, Vol. 3, 2004, pp 164-170.
- [65] N. Hur, S. Park, P. A. Sharma, J. S. Ahn, S. Guha and S. W. Cheong, "Electric polarization reversal and memory in a multiferroic material induced by magnetic fields", *Nature*, Vol. 429, 2004, pp 392-395.
- [66] H. Kastura, N. Nagaosa and A. V. Balatsky, "Spin current and magnetoelectric effect in noncollinear magnets," *Physics Review Letters*, Vol. 95, 2005, pp. 057205.

- [67] T. Kimura, T. Goto, H. Shintani, K. Ishizaka, T. Arima, and Y. Tokura, "Magnetic control of ferroelectric polarization," *Nature*, Vol. 426, 2003, pp. 55-58.
- [68] Y. J. Choi, H. T. Yi, S. Lee, Q. Huang, V. Kiryukhin and S. W. Cheong, "Ferroelectricity in an Ising Chain Magnet," *Physics Review Letters*, Vol. 100, 2008, pp. 047601.
- [69] I. A. Sergienko, C. Şen, E. Dagotto, "Ferroelectricity in the Magnetic E-Phase of Orthorhombic Perovskites," *Physics Review Letters*, Vol. 97, 2006, pp. 227204.
- [70] N. Lee, Y. J. Choi, M. Ramazanoglu, W. Ratcli, V. Kiryukhin, and S.-W. Cheong, "Mechanism of exchange striction of ferroelectricity in multiferroic orthorhombic HoMnO single crystals," *Physics Review B*, Vol. 84, 2011, pp. 3020101.
- [71] Y. F. Popov, A. M. Kadomtseva, G. P. Vorob'Ev and A. K. Zvezdin, "Discovery of the linear magnetoelectric effect in magnetic ferroelectric BiFeO_3 in a strong magnetic field," *Ferroelectrics*, Vol. 162, 1994, pp. 135-140.
- [72] R.D. Shannon, "Revised Effective Ionic Radii and Systematic Studies of Interatomic Distances in Halides and Chalcogenides," *Acta Crystallographica*, Vol. A32 1976, pp 751-767.
- [73] T. Mizokawa, D.I. Khomskii and G.A. Sawatzky, "Interplay between orbital ordering and lattice distortions in LaMnO_3 , YVO_3 , and YTiO_3 ," *Physics Review B*, Vol. 60, 1999, pp 7309.
- [74] R.E. Cohen, H. Krakauer, *Ferroelectrics*, Vol.136, 1992, pp 95.
- [75] P. Curie, "Sur la symétrie dans les phénomènes *physiques*. Symétrie d'un champ électrique et d'un champ magnétique", *Journal de Physique*, Vol. 3, 1894, pp 393-417.
- [76] J. Valasek, "Piezoelectric and allied phenomena in Rochelle salt", *Physical Review*, Vol. 15, 1920, pp 537-538.
- [77] A. Perrier and A. J. Staring, *Archives des Sciences Physiques et Naturelles (Geneva)*, Vol. 4, 1922, pp 373-382.
- [78] A. Perrier and A. J. Staring, *Archives des Sciences Physiques et Naturelles (Geneva)*, Vol. 5, 1923, pp 333.
- [79] T. H. O'Dell, "The Electrodynamics of Magneto-electric Media", Publisher: North-Holland, Amsterdam, 1970.
- [80] I.E. Dzyaloshinskii, *Zh. Eksp. Teor. Fiz.*, Vol. 37, 1959, pp 88. [*Soviet Physics — JETP*, Vol. 10, 1959, pp 628.]
- [81] D.N. Astrov, *Zh. Eksp. Teor. Fiz.*, Vol. 38, 1960, pp 984. [*Soviet Physics — JETP*, Vol. 11, 1960, pp 708.]

- [82] E. Ascher, H. Rieder, H. Schmid and H. Stossel, "Some Properties of Ferromagnetoelectric Nickel-Iodine Boracite", $\text{Ni}_3\text{B}_7\text{O}_{13}\text{I}$ Journal of Applied Physics, Vol. 37, 1966, pp 1404-1405.
- [83] G. A. Smolensky, V. A. Isupov and A. I. Agronovskaya, Soviet Physics — Solid State, Vol. 1, 1959, pp 149- 150.
- [84] G. A. Smolenskii and I. E. Chupis, Soviet Physics — Solid State, Vol. 4, 1962, 4, pp 807.
- [85] H. Schmid, "Multi-ferroic magnetoelectrics. Ferroelectrics", Vol. 162, 1994, pp 665.
- [86] M. Fiebig, "Revival of the magnetoelectric effect", Journal of Physics D: Applied Physics, Vol. 38, 2005, pp R123.
- [87] W. Eerenstein, N.D. Mathur and J.F. Scott, "Multiferroic and magnetoelectric materials", Nature, Vol. 442, 2006, pp 759.
- [88] J. Wang, J.B. Neaton, H. Zheng, V. Nagarajan, S.B. Ogale, B. Liu, D. Viehland, V. Vaithyanathan, D.G. Schlom, U.V. Waghmare, N.A. Spaldin, K.M. Rabe, M. Wuttig and R. Ramesh, "Epitaxial BiFeO_3 Multiferroic Thin Film Heterostructures", Science, Vol. 299, 2003, pp 1719-1722.
- [89] A. Filippetti and N.A. Hill, "Coexistence of magnetism and ferroelectricity in perovskites," Physics Review B, Vol. 65, 2002, pp 195120.:
- [90] V.S Filip'ev, I.P Smol'yaninov, E.G Fesenko and I.I Belyaev, Soviet Physics — Crystallogr., Vol. 5, 1960, pp 913.
- [91] F. Kubel and H. Schmid, "Structure of a ferroelectric and ferroelastic monodomain crystal of the perovskite BiFeO_3 ," Acta Crystallographica B, Vol. 46, 1990, pp 698.
- [92] A. Palewicz, I. Sosnowska, R. Przeniosła and A.W. Hewat, "BiFeO₃ Crystal Structure at Low Temperatures," Acta Physica Polonica A, Vol. 117, 2010, pp 296.
- [93] R. D. Shannon, "Revised Effective Ionic Radii and Systematic Studies of Interatomic Distances in Halides and Chalcogenides," Acta Crystallographica A, Vol. 32, 1976, pp 751.
- [94] R. Palai, R. S. Katiyar, H. Schmid, P. Tissot, S. J. Clark, J. Robertson, S. A. T. Redfern, G. Catalan and J. F. Scott, " β phase and γ - β metal-insulator transition in multiferroic BiFeO_3 ," Physics Review B, Vol. 77, 2008, pp 014110.
- [95] M. Polomska, W. Kaczmarek and Z. Pajak, "Electric and magnetic properties of $(\text{B}_{1-x}\text{La}_x)\text{FeO}_3$ solid solutions," Physica Status Solidi, Vol. 23, 1974, pp 567-574.
- [96] N. N. Krainik, N. P. Khuchua, A. A. Bierezhnoi, A. G. Tutov, A. J. Cherkashtchenko, Izvestiya Akademii Nauk SSR, Seriya Fizicheskaya, Vol. 29, 1965, pp 1026.

- [97] R. Haumont, J. Kreisel, P. Bouvier and F. Hippert, "Spin-phonon coupling in multiferroics," *Physics Review B*, Vol. 73, 2006, 73, pp 132101.
- [98] I. A. Kornev, S. Lisenkov, R. Haumont, B. Dkhil and L. Bellaiche, "Finite- temperature properties of multiferroic BiFeO₃," *Physics Review Letter*, Vol. 99, 2007, pp 227602.
- [99] R. Haumont, I. A. Kornev, S. Lisenkov, L. Bellaiche, J. Kreisel and B. Dkhil, "Phase stability and structural temperature dependence in powdered multiferroic BiFeO₃," *Physics Review B*, Vol. 78, 2008, pp 134108.
- [100] S.M. Selbach, T. Tybell, M.-A. Einarsrud and T. Grande, "High-temperature semiconducting cubic phase of BiFe_{0.7}Mn_{0.3}O₃," *Advanced Materials*, Vol. 20, 2008, pp 3692.
- [101] D. C. Arnold, K. S. Knight, F. D. Morrison, P. Lightfoot, *Physics Review Letter*, Vol. 102, 2009, pp 027602.
- [102] S. A. T. Redfern, J. N. Walsh, S. M. Clark, G. Catalan, J. F. Scott, arXiv: 0901.3748, 2009 (unpublished).
- [103] J.R. Teague, R. Gerson and W. J. James, *Solid State Communications*, Vol. 8, 1970, pp. 1073.
- [104] F. Zavaliche, R.R. Das, D.M. Kim, C.B. Eom, S.Y. Yang, P. Shafer, and R. Ramesh, *Applied Physics Letter*, Vol. 87, 2005, pp 182912.
- [105] N. N. Krainik, N. P. Khuchua, V. V. Zhdanova, V. A. Evseev, *Soviet Physics — Solid State*, Vol. 8, 1966, pp. 654.
- [106] W. Kaczmarek, Z. Pajak, M. Polomska, *Solid State Communication*, Vol. 17, 1975, pp.807.
- [107] S. Kamba, D. Nuzhnyy, M. Savinov, J. Šebek, J. Petzelt, J. Prokleska, R. Haumont, J. Kreisel, *Physics Review B*, Vol. 75, 2007, pp.024403.
- [108] M. Polomska, W. Kaczmarek, Z. Pajak, *Physica Status Solidi*, Vol. 23, 1974, pp.567.
- [109] J.-P. Rivera, H. Schmid, *Ferroelectrics*, Vol. 204, 1997, pp.23.
- [110] I. Sosnowska, T. Peterlin-Neumaier, E. Steichele, *Journal of Physics C: Solid State Physics*, Vol. 15, 1982, pp. 4835.
- [111] P. Fischer, M. Polomska, I. Sosnowska, M. Szymanski, *Journal of Physics C: Solid State Physics*, Vol. 13, 1980, pp. 1931.
- [112] D. Lebeugle, D. Colson, A. Forget, M. Viret, A.M. Bataille, A. Gukasov, *Physical Review Letters*, Vol. 100, 2008, pp. 227602.

- [113] G. Catalan, G. and J.F. Scott, *Advanced Materials*, Vol. 21, 2009, pp. 2463 .
- [114] W. Jie, R. Haumont, R. Jarrier, P. Berhtet, B. Dkhil, *Applied Physics Letter*, Vol. 96, 2010, pp. 102509.
- [115] X. Qingyu, Z. Haifa, D. Wu, T. Qiu, and M.X. Xu, *Applies Physics Letter*, Vol. 95, 2009, pp. 112510.
- [116] W. Yao, Q. Jiang, H. He, C.W. Nan, *Applied Physics Letter*, Vol. 88, 2006, pp. 142503.
- [117] M. Kumar, K.L. Yadav, *Applied Physics Letter*, Vol. 91, 2007, pp. 112911.
- [118] S.R. Shannigrahi, A. Huang, N. Chandrasekhar, D. Tripathy, A.O. Adeyeye, *Applied Physics Letter*, Vol. 90, 2007, pp. 022901.
- [119] Z. Shan-Tao, Z. Yi Lu, D. Ming-Hui, C. Chao-Ling, L. Yan-Feng, Z. Zhi-Guo, M. Yong-Yuan, P. Nai-Ben, X. Q., *Applied Physics Letter*, Vol. 88, 2006, pp. 162901.
- [120] Z. Yan, K.F.Wang, J.F. Qu, Y. Wang, Z.T. Song, and S.L. Feng, *Applied Physics Letter*, Vol. 91, 2007, pp. 082906.
- [121] S. Karimi, I.M. Reaney, I. Levin, I. Sterianou, *Applied Physics Letter*, Vol. 94, 2009, pp. 112903.
- [122] V.A. Khomchenko, V. V. Shvartsman, P. Borisov, W. Kleemann, D.A. Kiselev, I.K. Bdikin, J.M. Vieira, A.L. Kholkin, *Acta Materialia*, Vol. 57, 2009, pp. 5137 .
- [123] Fujitsu website: <http://www.fujitsu.com/my/news/pr/fmal20060808.html>
- [124] H. W. Jang, S. H. Baek, D. Ortiz, C. M. Folkman, C. B. Eom, Y. H. Chu, P. Shafer, R. Ramesh, V. Vaithyanathan, D. G. Schlom, *Applied Physics Letter*, Vol. 92, pp. 062910.
- [125] X. J. Lou, C. X. Yang, T. A. Tang, Y. Y. Lin, M. Zhang, J. F. Scott, *Applied Physics Letter*, Vol. 90, 2007, pp. 262908.
- [126] D. I. Woodward, I. M. Reaney, R. E. Eitel, C. A. Randall, *Journal of Applied Physics*, Vol. 94, 2003, pp. 3313.
- [127] B. Noheda, D. E. Cox, G. Shirane, J. A. Gonzalo, L. E. Cross, S. E. Park, *Applied Physics Letter*, Vol. 94, 1999, pp. 2059.
- [128] S. Fujino, M. Murakami, V. Anbusathaiah, S.-H. Lim, V. Nagarajan, C. J. Fennie, M. Wuttig, L. Salamanca-Riba, I. Takeuchi, *Applied Physics Letter*, Vol. 92, 2008, pp. 202904.
- [129] H. Bea, M. Gajek, M. Bibes, A. Barthelemy, *Journal of Physics: Condensed Matter*, Vol. 20, 2008, pp. 434231.

- [130] T. Zhao, A. Scholl, F. Zavaliche, K. Lee, M. Barry, A. Doran, M. P. Cruz, Y. H. Chu, C. Ederer, N. A. Spaldin, R. R. Das, D. M. Kim, S. H. Baek, C. B. Eom, R. Ramesh, *Nature Materials*, Vol. 5, 2006, pp. 823.
- [131] S. Lee, W. Ratcliff, S.-W. Cheong, V. Kiryukhin, *Applied Physics Letter*, Vol. 92, 2008, pp. 192906.
- [132] D. Lebeugle, D. Colson, A. Forget, M. Viret, A. M. Bataille, A. Gukasov, *Physics Review Letter*, Vol. 100, 2008, pp. 227602.
- [133] J. Nogues, I. K. Schuller, *Journal of Magnetism and Magnetic Materials*, Vol. 192, 1999, pp. 203.
- [134] P. Borisov, A. Hochstrat, X. Chen, W. Kleemann, C. H. Binck, *Physics Review Letter*, Vol. 94, 2005, pp. 117203.
- [135] V. Laukhin, V. Skumryev, X. Marti ´, D. Hrabovsky, F. Sa ´nchez, M. V. Garc ´ıa-Cuenca, C. Ferrater, M. Varela, U. Lu ´nders, J. F. Bobo, J. Fontcuberta, *Physics Review Letter*, Vol. 97, 2006, pp. 227201.
- [136] J. Dho, X. Qi, H. Kim, J. L. MacManus-Driscoll, M. G. Blamire, "Large electric polarization and exchange bias in multiferroic BiFeO₃", *Advanced Materials*, Vol. 18, 2006, pp. 1445.
- [137] H. Be ´a, M. Bibes, S. Cherifi, F. Nolting, B. Warot-Fonrose, S. Fusil, G. Herranz, C. Deranlot, E. Jacquet, K. Bouzouane, A. Barth ´el ´emy, "Tunnel magnetoresistance and robust room temperature exchange bias with multiferroic BiFeO₃ epitaxial thin films", *Applied Physics Letter*, Vol. 89, 2006, pp. 242114.
- [138] H. Be ´a, M. Bibes, F. Ott, B. Dupe ´, X.-H. Zhu, S. Petit, S. Fusil, C. Deranlot, K. Bouzouane, A. Barth ´el ´emy, "Mechanisms of exchange bias with multiferroic BiFeO₃ epitaxial thin films", *Physics Review Letter*, Vol. 100, 2008, pp. 017204.
- [139] Y.-H. Chu, L. W. Martin, M. B. Holcomb, M. Gajek, S.-J. Han, Q. He, N. Balke, C.-H. Yang, D. Lee, W. Hu, Q. Zhan, P.-L. Yang, A. Fraile-Rodr ´ıguez, A. Scholl, S. X. Wang, R. Ramesh, "Electric field control of local ferromagnetism using a magnetoelectric multiferroic" *Nature Materials*, Vol. 7, 2008, pp. 478-482.
- [140] H. Bea, S. Fusil, K. Bouzouane, M. Bibes, M. Sirena, G. Herranz, E. Jacquet, J.-P. Contour, A. Barth ´el ´emy, "Ferroelectricity down to at least 2 nm in multiferroic BiFeO₃ epitaxial thin films" *Japanese Journal of Applied Physics*, Vol. 45, 2006, pp. L187.
- [141] M. Gajek, M. Bibes, S. Fusil, K. Bouzouane, J. Fontcuberta, A. Barth ´el ´emy, A. Fert, "Tunnel junctions with multiferroic barriers", *Nature Materials*, Vol. 6, 2007, pp. 296.
- [142] M. Bibes, A. Barth ´el ´emy, "Towards a magnetoelectric memory", *Nature Materials*, Vol. 7, 2008, pp. 425-426.

- [143] M. Stuer, Z.Zhao, U. Aschauer, P. Bowen, "Transparent Polycrystalline Alumina using Spark Plasma Sintering: effect of Mg, Y and La doping" *J Eur Ceram Soc.* 30 (2010) pp. 1335-1343.
- [144] V.R. Mudinepalli, S.H. Song, J.Q. Li, et al., A comparative study of structural and electrical properties of $Ba_{0.8}Pb_{0.2}TiO_3$ nanocrystalline ceramics prepared by microwave and spark plasma sintering, *Mater. Chem. Phys.* 142 (2013) pp. 686–691.
- [145] J.Q. Li, L.F. Li, S.H. Song, et al., High thermoelectric performance of the GeTe– Ag_8GeTe_6 composites, *J. Alloy. Compd.* 565 (2013) pp. 144–147.
- [146] Shen, Z., Johnsson, M., Zhao, Z., & Nygren, M. (2002), *J. Am. Cer. Soc.*, 85, pp. 1921-7.
- [147] Liu, J., Shen, Z., Nygren, M., Su, B. & Button, T. W. (2006), *J. Am. Cer. Soc.*, 89, pp. 2689-94.
- [148] Navrotsky A. Energetics of oxide nanoparticles. *International Journal of Quantum Chemistry.*2009;109:2647. DOI: 10.1002/qua.21981.
- [149] Allen, Terence, *Particle Size Measurement*, Chapman and Hall, New York 1981.
- [150] Kayani, Zohra N., Saira Riaz, and Shahzad Naseem. "Preparation of BiFeO₃ films by sol-gel technique and their characterization." *Sci. Int.(Lahore)* 23.4 (2011): pp. 255-258.
- [151] Johari, Anoopshi. "Synthesis and characterization of bismuth ferrite Nnanoparticles." *AKGEC Journal of Technology July-December* 2.2 (2011): pp. 0975-9514.
- [152] Zhou, Min, et al. "Hydrothermal synthesis of bismuth ferrite Fenton-like catalysts and their properties." *Journal of Nanoparticle Research* 18.11 (2016): pp. 346.
- [153] Dai, Zhong-Hua, and Yukikuni Akishige. "BiFeO₃ ceramics synthesized by spark plasma sintering." *Ceramics International* 38 (2012): pp. S403-S406.
- [154] G. V. Subba Rao, C. N. R. Rao, and J. R. Ferraro, "Infrared and Electronic spectra of Rare Earth Perovskites: Ortho-Chromites, -Manganites and –Ferrites," *Appl. Sp ectrosc.*, 24, pp. 436–45 (1970).
- [155] Catalan, Gustau, and James F. Scott. "Physics and applications of bismuth ferrite." *Advanced Materials* 21.24 (2009): pp. 2463-2485.
- [156] Rojac, T., Bencan, A., Malic, B., Tutuncu, G., Jones, J. L., Daniels, J. E., & Damjanovic, D. (2014). BiFeO₃ ceramics: processing, electrical, and electromechanical properties. *Journal of the American Ceramic Society*, 97(7), pp. 1993-2011.
- [157] Shaldin, Y. V., Matyjasik, S., & Bush, A. A. (2007). Pyroelectric properties of bismuth ferrite in the low-temperature range. *Crystallography Reports*, 52(1), pp. 123-128.

- [158] Rojac, T., Kosec, M., Budic, B., Setter, N., & Damjanovic, D. (2010). Strong ferroelectric domain-wall pinning in BiFeO₃ ceramics. *Journal of Applied Physics*, *108*(7), pp. 074107.
- [159] Kreisel, J., Alexe, M., & Thomas, P. A. (2012). A photoferroelectric material is more than the sum of its parts. *Nature materials*, *11*(4), pp. 260.
- [160] Yang, Y., Infante, I. C., Dkhil, B., & Bellaiche, L. (2015). Strain effects on multiferroic BiFeO₃ films. *Comptes Rendus Physique*, *16*(2), pp. 193-203.
- [161] Schneider, J., Matsuoka, M., Takeuchi, M., Zhang, J., Horiuchi, Y., Anpo, M., & Bahnemann, D. W. (2014). Understanding TiO₂ photocatalysis: mechanisms and materials. *Chemical reviews*, *114*(19), pp. 9919-9986.
- [162] Bai, X., Wei, J., Tian, B., Liu, Y., Reiss, T., Guiblin, N., ... & C. Infante, I. (2016). Size effect on optical and photocatalytic properties in BiFeO₃ nanoparticles. *The Journal of Physical Chemistry C*, *120*(7), pp. 3595-3601.
- [163] R. L. Sutherland, Handbook of Nonlinear Optics (Marcel Dekker, 2003).
- [164] H. Yokota, R. Haumont, J.-M. Kiat, H. Matsuura, and Y. Uesu, Appl. Phys. Lett. *95*, 082904 (2009).
- [165] S. Ju, T.-Y. Cai, and G.-Y. Guo, J. Chem. Phys. *130*, 214708 (2009).
- [166] R. C. Haislmaier, N. J. Podraza, S. Denev, A. Melville, D. G. Schlom, and V. Gopalan, Appl. Phys. Lett. *103*, 031906 (2013).
- [167] S. Ju and T.-Y. Cai, Appl. Phys. Lett. *95*, 112506 (2009).
- [168] R. J. Zeches, M. D. Rossell, J. X. Zhang, A. J. Hatt, Q. He, C.-H. Yang, A. Kumar, C. H. Wang, A. Melville, C. Adamo, G. Sheng, Y.-H. Chu, J. F. Ihlefeld, R. Erni, C. Ederer, V. Gopalan, L. Q. Chen, D. G. Schlom, N. A. Spaldin, L. W. Martin, and R. Ramesh, Science *326*, 977 (2009).
- [169] J. F. Ihlefeld, A. Kumar, V. Gopalan, Y. B. Shen, X. Q. Pan, T. Heeg, J. Schubert, X. Ke, P. Schiffer, J. Orenstein, L. W. Martin, Y. H. Chu, R. Ramesh, and D. G. Schlom, Appl. Phys. Lett. *91*, pp. 071922 2007.
- [170] J. Petzelt and V. Dvořák, J. Phys. C *9*, pp. 1571 1976.
- [171] Kamba, S., Nuzhnyy, D., Savinov, M., Šebek, J., Petzelt, J., Prokleška, J., ... & Kreisel, J. (2007). Infrared and terahertz studies of polar phonons and magnetodielectric effect in multiferroic BiFeO₃ ceramics. *Physical Review B*, *75*(2), pp. 024403.
- [172] I. Levin, M. G. Tucker, H. Wu, V. Provenzano, C. L. Dennis, S. Karimi, T. Comyn, T. Stevenson, R. I. Smith, and I. M. Reaney, Chem. Mater. *23*, pp. 2166 (2011).

- [173] Goian, V., Kamba, S., Greicius, S., Nuzhnyy, D., Karimi, S., & Reaney, I. M. (2011). Terahertz and infrared studies of antiferroelectric phase transition in multiferroic $\text{Bi}_{0.85}\text{Nd}_{0.15}\text{FeO}_3$. *Journal of Applied Physics*, 110(7), pp. 074112.
- [174] Shino, T. & Oikawa, D.(2002), *Mat. Sci.*, 11, pp. 81-102
- [175] Colthup, N. *Introduction to Infrared and Raman spectroscopy*. (Elsevier, 2012).
- [176] Rayleigh, J. W.S. B. *On the scattering of light by small particles*. (1871)
- [177] Rayleigh, L. X. On the electromagnetic theory of light. *The London, Edinburgh, and Dublin Philosophical Magazine and Journal of Science* 12, pp. 81-101(1881).
- [178] Smekal, A. Zur quantentheorie der dispersion. *Naturwissenschaften* 11, pp. 873-875(1923).
- [179] M.K. Singh, H.M. Jang, S. Ryu, M.H. Jo, *Appl. Phys. Lett.* 88 (2006) pp. 042907.
- [180] D. Kothari, V.R. Reddy, A. Gupta, V. Sathe, A. Banerjee, S.M. Gupta, A.M. Awasthi, *Appl. Phys. Lett.* 91 (2007) pp. 202505.
- [181] H. Fukumura, S. Matsui, H. Harima, T. Takahashi, T. Itoh, K. Kisoda, M. Tamada, Y. Noguchi, M. Miyayama, *J. Phys.: Condens. Matter* 19 (2007) pp. 365224.
- [182] Y. Wang, C.-W. Nan, *J. Appl. Phys.* 103 (2008) pp. 114104.
- [183] Y. Yang, J.Y. Sun, K. Zhu, Y.L. Liu, J. Chen, X.R. Xing, *Physica B* 404 (2009) pp. 171.
- [184] R. Palai, H. Schmid, J.F. Scott, R.S. Katiyar, *Phys. Rev. B* 81 (2010) pp. 064110.
- [185] Brankovic, Z., Golic, D. L., Radojkovic, A., Cirkovic, J., Pajic, D., Stanojevic, Z. M., ... & Brankovic, G. (2016). Spark plasma sintering of hydrothermally synthesized bismuth ferrite. *Processing and Application of Ceramics*, 10(4), pp. 257-264.
- [186] Lebeugle, D.; Colson, D.; Forget, A.; Viret, M.; Bonville, P.; Marucco, J. F.; Fusil, S., (2007): Room temperature coexistence of large electric polarization and magnetic order in BiFeO_3 single crystals. *Phys. Rev. B*, 76 (2): 024116.
- [187] Valant, M.; Axelsson, A. K.; Alford, N., (2007): Peculiarities of a solid-state synthesis of multiferroic polycrystalline BiFeO_3 . *Chem. Mater.*, 19: pp. 5431-5436
- [188] Carvalho, T. T.; Tavares, P. B., (2008): Synthesis and thermodynamic stability of multiferroic BiFeO_3 . *Mater. Lett.*, 62 (24): pp. 3984-3986.
- [189] Selbach, S. M.; Einarsrud, M. A.; Grande, T., (2009): On the Thermodynamic Stability of BiFeO_3 . *Chem. Mater.*, 21 (1): pp. 169-173.

- [190] Morozov, M. I.; Lomanova, N. A.; Gusarov, V. V., (2003): Specific features of BiFeO₃ formation in a mixture of bismuth(III) and iron(III) oxides. *Russ. J. Gen. Chem.*, 73 (11): pp. 1676-1680.
- [191] A. Fidalgo, L.M. Ilharco, J. Non-Cryst. Solids 283 (2011) 144.
- [192] Ikeda, T. (1996). *Fundamentals of piezoelectricity*. Oxford university press.
- [193] Shvartsman, V. V., Kleemann, W., Haumont, R., & Kreisel, J. (2007). Large bulk polarization and regular domain structure in ceramic BiFeO₃. *Applied physics letters*, 90(17), 172115.
- [194] Wang, T., Song, S. H., Wang, M., Li, J. Q., & Ravi, M. (2016). Effect of annealing atmosphere on the structural and electrical properties of BiFeO₃ multiferroic ceramics prepared by sol-gel and spark plasma sintering techniques. *Ceramics International*, 42(6), pp. 7328-7335.
- [195] E. O'Sullivan, M.Sc. Thesis, University of Limerick, 2015.
- [196] Bismibanu, A., Alagar, M., Jebaselvi, J. M., & Gayathri, C. Preparation and Characterization of Bismuth Ferrite Nanoparticle Using Sol-Gel Method.
- [197] Vanga, P. R., Mangalaraja, R. V., & Ashok, M. (2015). Structural, magnetic and photocatalytic properties of La and alkaline co-doped BiFeO₃ nanoparticles. *Materials Science in Semiconductor Processing*, 40, pp. 796-802.
- [198] Sree Rama Linga Prasad, C., Sreenivasulu, G., Roopas Kiran, S., Balasubramanian, M., & Murty, B. S. (2011). Electrical and magnetic properties of nanocrystalline BiFeO₃ prepared by high energy ball milling and microwave sintering. *Journal of nanoscience and nanotechnology*, 11(5), pp. 4097-4102.
- [199] Islam, M. R., Islam, M. S., Zubair, M. A., Usama, H. M., Azam, M. S., & Sharif, A. (2018). Evidence of superparamagnetism and improved electrical properties in Ba and Ta co-doped BiFeO₃ ceramics. *Journal of Alloys and Compounds*, 735, pp. 2584-2596.
- [200] Sharma, S., Singh, V., Kotnala, R. K., & Dwivedi, R. K. (2014). Comparative studies of pure BiFeO₃ prepared by sol-gel versus conventional solid-state-reaction method. *Journal of Materials Science: Materials in Electronics*, 25(4), pp. 1915-1921.
- [201] Chong, K. B., Guiu, F., & Reece, M. J. (2008). Thermal activation of ferroelectric switching. *Journal of Applied Physics*, 103(1), pp. 014101.
- [202] Dai, H. Y., Chen, Z. P., Li, T., Xue, R. Z., & Chen, J. (2013). Structural and electrical properties of bismuth ferrite ceramics sintered in different atmospheres. *Journal of superconductivity and novel magnetism*, 26(10), pp. 3125-3132.